

55-45
53442
p. 69

CHAPTER 10

N92-15462

Trends in Aerosol Abundances and Distributions

Panel Members

R. P. Turco and M. P. McCormick, Co-Chairs

R. T. Clancy

R. Curran

J. DeLuisi - NJ920944

P. Hamill

G. Kent

J. M. Rosen

O. B. Toon

G. Yue

Chapter 10

Trends in Aerosol Abundances and Distributions

Contents

10.1	INTRODUCTION	599
10.2	AEROSOLS IN THE MIDDLE AND LOWER ATMOSPHERE	599
10.2.1	Aerosol Species	599
10.2.2	Optical Properties of Aerosols	602
10.2.3	Aerosol Radiative Transfer	604
10.2.4	Measured Properties of Aerosols	606
10.2.5	Aerosol Microphysical Parameters	607
10.3	LONG-TERM AEROSOL DATA BASES	609
10.3.1	Mauna Loa Observations	609
10.3.2	University of Wyoming Dustsonde	611
10.3.3	Satellite Systems: SAM, SAGE, SME	615
10.3.3.1	SAM and SAGE	615
10.3.3.2	SME	618
10.3.3.3	SAGE/SME Intercomparisons	622
10.4	AEROSOL PERTURBATIONS: EL CHICHÓN AND OTHER EVENTS	622
10.4.1	El Chichón	623
10.4.1.1	Cloud Characteristics and Behavior, April–December 1982	625
10.4.1.2	Cloud Characteristics and Behavior, 1983–1986	628
10.4.2	Mount St. Helens and Other Volcanic Eruptions	629
10.5	AEROSOL IMPACT ON OZONE OBSERVATIONS	632
10.5.1	Umkehr	632
10.5.1.1	Description of the Aerosol Error	632
10.5.1.2	Calculation of Umkehr/Aerosol Errors	636
10.5.2	Solar Backscatter Ultraviolet (SUBV)	639
10.5.2.1	Description of the Aerosol Error	639
10.5.2.2	Implications of SME Data for SBUV Ozone Trends	640
10.5.3	Aerosol Data Requirements for Ozone Observing Systems	640
10.6	POLAR STRATOSPHERIC CLOUDS AND THE OZONE HOLE	641
10.6.1	Observations and Morphology of PSC's	642
10.6.1.1	The SAM-II Satellite System	642
10.6.1.2	PSC Properties	643
10.6.1.3	PSC's in the Northern Polar Vortex	650
10.6.1.4	Long-Term Trends in PSC Properties	651

10.6.2	Physical Chemistry and Microphysics of PSC's	651
10.6.2.1	Sulfuric Acid Ice Clouds	652
10.6.2.2	Nitric Acid Ice Clouds	655
10.6.2.3	Hydrochloric Acid Ice	659
10.6.2.4	Ice Clouds	660
10.6.3	Radiative Properties of PSC's	660
10.6.3.1	PSC Lidar Backscatter and Polarization Characteristics	660
10.6.3.2	Radiative Heating of PSC's	661
10.7	CONCLUSIONS	662

10.1 INTRODUCTION

In this chapter, the properties of aerosols that reside in the upper atmosphere are described, with special emphasis on the influence these aerosols may have on ozone observation systems, mainly through radiative effects, and on ambient ozone concentrations, mainly through chemical effects. It has long been appreciated that stratospheric particles can interfere with the remote sensing of ozone distribution. Here, the mechanism and magnitude of this interference, and potential spatial and temporal trends in the interference, are evaluated. Separate sections deal with the optical properties of upper atmospheric aerosols, long-term trends in stratospheric aerosols, perturbations of the stratospheric aerosol layer by volcanic eruptions, and estimates of the impacts that such particles have on remotely measured ozone concentrations.

Another section is devoted to a discussion of the polar stratospheric clouds (PSC's). These unique clouds, recently discovered by satellite observation, are now thought to be intimately connected with the Antarctic ozone hole (see Chapter 11). Accordingly, interest in PSC's has grown considerably in recent years. This chapter describes what we know about the morphology, physical chemistry, and microphysics of PSC's.

10.2 AEROSOLS IN THE MIDDLE AND LOWER ATMOSPHERE

The global measurement of ozone from orbiting satellites using the spectral signature of Earth's albedo is complicated by the presence of fine light-scattering (and absorbing) particles in the upper atmosphere. If the spatial distribution, size distribution, composition, and morphology of these particles are known, their optical properties can be determined and employed in the calculation of ozone abundances from the raw satellite radiance data. Most ozone-sensing systems are not designed to measure independently the aerosol properties that are required. Accordingly, in cases where aerosol interference is identified as a problem, corrections to the ozone observations may be estimated by using either a standard aerosol model, or coincident aerosol data from other sensors, or reanalysis of the onboard data (through a modified inversion scheme) to deduce the aerosol fields. Thus, several alternatives may be available to correct for the effects of aerosols in data retrieval procedures.

Two principal concerns regarding aerosol effects are noted:

1. Research teams working with the satellite radiance data and inversion schemes should be aware of the types and variations of particles in the upper atmosphere and their general optical properties.
2. Past measurements of ozone, both satellite and ground based, which may have been inadvertently contaminated by aerosol scattering effects, might be recalibrated (if this is possible) to allow more accurate ozone trend analyses.

10.2.1 Aerosol Species

Table 10.1 summarizes and compares information on the most prominent atmospheric particulates, including water clouds. Specific types of aerosols may not significantly affect a particular system, or may have been taken into account in designing the system. The general optical properties of aerosol particles are discussed in Section 10.2.2.

AEROSOL ABUNDANCES AND DISTRIBUTIONS

Table 10.1 Properties of Atmospheric Aerosols* and Clouds

Type of particulate	Altitude (km)	Horizontal scale (km)	Occurrence frequency	Composition	Mass loading (mg/m ³)	Vertical optical depth (at 550 nm)	Mean particle number radius (μm)	Principal size range (μm)
Stratus, cumulus, nimbus clouds	1–18	10–1,000	0.5	Water, ice	1,000–10,000	~1–100	10–1,000	Variable
Cirrus clouds	7–16	10–1,000	0.3	Ice	10–100	~1	~10–100	Variable
Fog	0–1	10–100	Sporadic	Water	10–100	1–10	~10	10–50
Tropospheric aerosols	0–10	1,000–10,000 (ubiquitous)	1	Sulfate, nitrate, minerals	0.01–0.1	~0.1	0.1–1	~0.3
Ocean haze	0–1	100–1,000	0.3	Sea salt sulfate	0.1–1	0.1–1	0.5	~0.3
Dust storms	0–3	10–1,000	Sporadic	Silicates, clays	<1–>100	1–10	1–10	10–100
Volcanic clouds	5–35	100–10,000	Sporadic	Mineral ash, sulfates	<1–>1,000	0.1–10	0.1–10	1–10
Smoke	0–10	1–100	Sporadic (from fires)	Soot, ash, tars	0.1–1	~0.1–10	0.1–1	~0.3
Stratospheric aerosols	10–30	1,000–10,000 (ubiquitous)	1	Sulfate	0.001–0.01	~0.01	0.1	~0.1
Polar stratospheric clouds	15–25	10–1,000	0.1 (winter only)	HNO ₃ /H ₂ O ice	0.001–0.01	~0.01–1	1–10	~1
Polar mesospheric clouds	80–85	~200 (polar regions above 50°)	0.1 (summer only)	Ice	~0.0001	~0.0001–0.01	~0.05	~0.02
Meteoric dust	50–90	10–1,000	0.5–1	Minerals, carbon	~0.00001	~0.00001	≤0.01	Wide range incl. micro-meteors

*All particles that can be nucleated into cloud (water) droplets at supersaturations of $\geq 10\%$ are referred to as “condensation nuclei,” or cn. Those particles that can be nucleated at low supersaturations of $\leq 1\%$ are referred to as “cloud condensation nuclei,” or ccn.

The aerosols of primary interest include:

Volcanic Eruption Clouds

Large volcanic eruptions deposit ash and sulfurous gases in the stratosphere between 10 and 35 kilometers altitude. While the larger ash debris falls out of the atmosphere within a fairly short time (a few weeks or months) and locally near the explosion site, the sulfuric acid aerosol generated from the gaseous sulfur emissions can remain suspended for several years; the particle density and global distribution evolve over this period. The sulfuric acid particles typically have a radius <1 micrometer (or micron, μm), and thus are very efficient at light scattering. The vertical stratospheric extinction optical depth in major volcanic eruption plumes will vary from very high values at early times to values of ~ 0.1 to 0.5 over global scales at longer times. The occurrence of eruptions large enough to affect the stratosphere is unpredictable, with major events occurring on a time scale of decades, and smaller but significant events occurring perhaps every few years.

The optical properties of aged volcanic aerosols (at least several months old) are relatively uniform over hemispheric scales. Accordingly, the interfering aerosol radiances may be more

readily characterized and corrected in the ozone algorithms. Nevertheless, the distribution of aerosol light scattering exhibits large- and small-scale inhomogeneities that could still be significant. Moreover, the spectral signature of the aerosols depends on their size distribution, which can vary with time, location, and altitude. For a rough first-order optical analysis of solar transmission through background aerosols, it is probably adequate to assume a λ^{-1} dependence for light extinction (see Section 10.2.2).

The aerosol contribution to the radiance may be determined directly from the observations by including a factor in the inversion equation to account for aerosol effects. One or more of the sensor wavelengths may be used to characterize the aerosol properties. Alternatively, independent measurements of the aerosol properties from other satellites, aircraft surveys, or ground-based lidar soundings could be employed to develop a time-dependent model for the particulate radiances to be treated in the data retrieval scheme. At a simpler level, a standard volcanic-aerosol radiance model could be formulated and applied to correct the satellite data, after the absolute radiances in the model had been calibrated at a reference frequency.

Nacreous Clouds and Polar Stratospheric Clouds (PSC's)

These clouds are largely a manifestation of water vapor condensation (likely in combination with nitric acid vapor) in regions of extremely low stratospheric temperatures. The classical nacreous, or "mother of pearl," clouds often occur in the lee waves of orographic features, in the ascending, cooling region of the waves. Nacreous clouds are a relatively rare phenomenon and reside primarily in the lower stratosphere. They apparently consist of supercooled liquid droplets of about 1 micron radius with a very narrow size dispersion (which is responsible for the strong wavelength dependence of light scattering leading to the distinctive coloration of these clouds). PSC's are observed in the polar regions mainly in winter. Most of our knowledge of PSC's is derived from remote observations by the SAM-II satellite instrument. The clouds extend between roughly 10 and 25 kilometers in altitude, and are found at latitudes above about 65°. While the sizes and composition of PSC particles are not yet known precisely, a substantial amount of information is available to define their general physical and morphological properties (see Section 10.6). Measured extinction coefficients at 1 micron wavelength averaged over path lengths of ~ 100 km are typically of the order of $10^{-3}/\text{km}$, although higher and lower values are frequently observed. Hence, vertical cloud extinction optical depths of the order of 10^{-2} are expected, although much higher values could be found in fully developed clouds.

PSC's can have considerable spatial structure, as is revealed by lidar surveys. However, the clouds are largely confined to the polar regions in winter. Ozone data should be carefully analyzed for PSC effects under these observational conditions. The clouds are likely to be most prominent in the perpetual nighttime zone of the polar winter stratosphere when air temperatures are coldest; satellite sensors that use the Sun as a light source are quiescent in this situation (although other bright astronomical objects have been used as alternate light sources under special circumstances).

Noctilucent Clouds

These clouds are most likely water ice clouds formed near the mesopause (~ 80 km) in the summer at high latitudes. Noctilucent clouds have been studied extensively using ground-based observations, with occasional in situ measurements. However, even under optimal conditions, ground sightings of the clouds are quite rare. On the other hand, the SME satellite has cataloged a

AEROSOL ABUNDANCES AND DISTRIBUTIONS

more pronounced circumpolar cloud layer at the summer mesopause extending poleward from about 70°. The layer is only a few kilometers thick and seems to consist of ice crystals (of unknown morphology) of about 0.05 micron radius. The vertical optical thickness of the clouds is only $\sim 10^{-4}$. Reviews of noctilucent cloud properties based on past observations are provided by Fogle and Haurwitz (1966), Avaste et al. (1980), and Thomas (1984).

Because the noctilucent cloud particles are so small, their optical properties may be adequately described by Rayleigh scattering theory (see Section 10.2.2). In this case, the wavelength dependence of the light extinction (or scattering) would be given by λ^{-4} . This strong wavelength variation is in contrast to the much weaker wavelength dependence of scattering in suspensions of larger particles such as volcanic acid aerosols.

Tropospheric Aerosols

The particulates discussed so far reside in the stratosphere and mesosphere. Because they are coincident with the ozone layer, particles in the middle atmosphere can have a direct impact on the radiance fields that must be analyzed to obtain ozone profiles. Fortunately, the aerosols that might cause problems have, in general, small optical depths. By contrast, tropospheric clouds, hazes, and fogs can have large optical depths and substantial effects on Earth radiances (see Table 10.1). Because tropospheric clouds lie below the ozone layer, they introduce difficulties mainly in the following circumstances:

- When underlying the satellite field of view, they enhance the upwelling shortwave radiation and block the direct observation of the tropospheric component of the total ozone column concentration.
- When overlying ground-based instruments, they create a diffuse radiation field that dominates the radiance at the sensor.

Because of their more obvious manifestations, tropospheric clouds have been extensively treated in ozone observing systems, such as the Dobson network (see Chapter 3, which discusses ozone retrieval algorithms).

10.2.2 Optical Properties of Aerosols

The fundamental aerosol optical properties of importance here are the extinction coefficient and scattering phase function. The extinction cross-section of a single spherical particle at a specific wavelength can be written:

$$\sigma_e(\lambda) = \pi r^2 Q_e(r, \lambda, \eta),$$

$$\begin{aligned} \text{where } \sigma_e &= \text{cross section (cm}^2\text{)} \\ r &= \text{particle radius (cm)} \\ \lambda &= \text{wavelength (cm)} \\ \eta &= \text{index of refraction} = \eta_r - i\eta_i. \end{aligned}$$

Q_e is the Mie extinction efficiency, which can be expressed as a function of the Mie parameter x :

$$x = 2\pi r/\lambda,$$

or,

$$Q_e = Q_e(x, \eta).$$

Extinction is the sum of light scattering by a particle plus light absorption in the particle. Thus,

$$Q_e = Q_s + Q_a,$$

$$\sigma_e = \sigma_s + \sigma_a,$$

where Q_s and Q_a are the Mie scattering and absorption efficiencies, respectively, and σ_s and σ_a are the scattering and absorption cross sections, respectively.

The single-scatter albedo is defined as

$$\omega_o = \sigma_s / \sigma_e = Q_s / Q_e.$$

The detailed distribution of the scattered energy is described by the phase function, $P(\theta)$, such that the fraction of the total energy scattered into a small angular width $d\theta$ about the scattering angle θ is

$$\sigma_s(\theta, \lambda) = \sigma_s(\lambda) P(\theta) \sin(\theta) / 2d\theta$$

where P is then normalized as

$$\frac{1}{2} \int_0^\pi P(\theta) \sin(\theta) d\theta = 1.$$

Here, θ is the scattering angle measured from the forward direction of the light ray ($\theta = 0$) toward the backward direction ($\theta = \pi$), and azimuthal symmetry is assumed for the scattered field.

It is also convenient to define the asymmetry factor for particle scattering as

$$g = \frac{1}{2} \int_0^\pi P(\theta) \cos(\theta) \sin(\theta) d\theta.$$

Aerosols tend to scatter light preferentially in the forward direction, with $g \sim 0.7$. Cloud droplets exhibit stronger forward scattering, with $g \sim 0.9$. For molecular (Rayleigh) scattering, $g = 0$; that is, there is equal forward and backward scattering.

Individual aerosol particles have phase functions that exhibit a complex structure of scattering intensity lobes; the number of such lobes is generally equal to the Mie parameter x . However, in a typical collection of atmospheric particles of different sizes, the "lobe" structures in the scattered radiation field are averaged out. Accordingly, it is often possible to employ a simplified composite scattering pattern such as the Henyey-Greenstein phase function (which, however, neglects the backscatter peak):

$$P(\theta) = (1 - g^2) / [1 + g^2 - 2g \cos(\theta)]^{3/2},$$

where g is the average asymmetry factor for the aerosols.

AEROSOL ABUNDANCES AND DISTRIBUTIONS

A collection of spherical particles of a given type can usually be accurately described by a size distribution function $n_p(r)$, where $n_p(r)dr$ is the number of particles per cubic centimeter of air with sizes between r and $r + dr$. The volume extinction (scattering, absorption) coefficient is defined as

$$\beta_{e\lambda}(\bar{y}) = \int_0^\infty \pi r^2 Q_e(r, \lambda, \eta) n_p(r, \bar{y}) dr \quad (\text{cm}^{-1}),$$

where the spatial variation has been included through the vector location \bar{y} , and η is assumed to be independent of particle size and location. The total concentration of particles is given by

$$N_p(\bar{y}) = \int_0^\infty n_p(r, \bar{y}) dr \quad (\text{particles/cm}^3).$$

The extinction (scattering, absorption) *optical depth* along a specific ray through the atmosphere is defined in terms of the extinction coefficient as:

$$\tau_{e\lambda} = \int_{\text{ray } \bar{s}} \beta_{e\lambda}(\bar{y}) ds.$$

where ds is the length increment along the ray \bar{s} .

In lidar observations, the radiation received at the instrument originates in the backscattering of the emitted laser beam. The backscatter cross-section is given by $\sigma_s(\pi, \lambda)$, and can be integrated over the particle size distribution in analogy to the extinction cross-section to yield the backscatter coefficient, $\beta_{b\lambda}(\bar{y})$. Occasionally lidar data are reported as integrated backscatter coefficients, in which $\beta_{b\lambda}(\bar{y})$ is integrated along the lidar path through the aerosol layer, by analogy with the extinction optical depth. The radiance seen by a lidar instrument also contains a Rayleigh scattering component from the air molecules in which the observed aerosols are embedded. The analysis for the aerosol component of the scattered radiance is usually based on a background atmospheric model for the air scattering, or normalization of the return signal in regions where aerosols are not expected to be present.

When an ensemble of different particle and gas species that scatter and absorb radiation is considered, all of the above optical parameters must be summed over the ensemble (for the scattered radiation, contributions from individual scattering centers are treated as incoherent sources).

10.2.3 Aerosol Radiative Transfer

The basic problem in radiative transfer as applied to remote sensing in general, and thus to ozone detection, is to solve the monochromatic transfer equation

$$dI_\lambda/d\tau_\lambda = -I_\lambda + S_\lambda,$$

for the appropriate wavelengths (or wavelength bands), geometries and boundary conditions. In this equation, I_λ is the radiance (energy/area-time-steradian-wavelength), $d\tau_\lambda$ is the differential optical depth (including all optically active species) along the ray path, and S_λ is the source function, which at visible and near-ultraviolet wavelengths can have a direct and single-scatter solar component, a multiple-scatter skylight component, and possible contributions from fluorescence and chemiluminescence.

Solution of the general radiative transfer equations in practical situations usually involves a number of simplifications. For example, light scattering by air molecules and very small particles may be described by the Rayleigh cross-section and phase function, for which

$$Q_s(x, \eta) = \frac{8}{3} x^4 |(\eta^2 - 1)/(\eta^2 + 2)|^2,$$

and

$$P_R(\theta) = \frac{3}{4} [1 + \cos^2(\theta)].$$

For air, the Rayleigh extinction coefficient can be accurately expressed in the form

$$\beta_{e\lambda}(\bar{y}) = c \rho(\bar{y})/\lambda^4,$$

where $\rho(\bar{y})$ is the density of air (g/cm^3) and c is a constant.

The single-scattered radiance reaching a satellite sensor from an atmosphere containing particles may be expressed as follows:

$$I_{s\lambda} = \int_{\substack{\text{obs. path} \\ \bar{s}}} [P_R(\theta)\beta_{gs\lambda}(\bar{y}) + P_p(\theta)\beta_{ps\lambda}(\bar{y})] F_{o\lambda} \exp[-\tau_{eo\lambda}(\bar{y})] \exp[-\tau_{e\lambda}(\bar{y})] ds$$

where $F_{o\lambda}$ = incident solar irradiance
 $\beta_{gs\lambda}$ = volume scattering coefficient for the gases
 $\beta_{ps\lambda}$ = volume scattering coefficient for larger particles
 P_R = Rayleigh scattering phase function
 P_p = average aerosol phase function, which may vary along the ray path
 $\tau_{eo\lambda}$ = total extinction optical depth for solar rays to the point \bar{y} , equal to $\tau_{geo\lambda} + \tau_{peo\lambda}$,
 $\tau_{e\lambda}$ = total extinction optical depth for the observation ray to the point \bar{y} , equal to $\tau_{ge\lambda} + \tau_{pe\lambda}$.

The total extinction and scattering terms have components associated with molecular Rayleigh scatter, ozone absorption, other gaseous absorption depending on wavelength, and particle scattering and absorption. Additional contributions to the radiance should be included for surface and cloud reflection, multiple-scattered light, and fluorescence.

Figure 10.1 illustrates some of the possible geometries for passive remote sensing of the lower atmosphere and ozone layer from space and from the ground.

As an example of the application of the general radiative transfer equation displayed above to a nadir-viewing satelliteborne sensor, the angle θ would be equated to the solar zenith angle, and the optical depths $\tau_{eo\lambda}$ and $\tau_{e\lambda}$ would be related by $\tau_{eo\lambda} = \sec(\theta)\tau_{e\lambda}$. Inasmuch as $P_p(\theta)$ is generally much smaller than $P_R(\theta)$ in the stratosphere for typical geometries because particles are more strongly forward scattering, the aerosol contribution to the total radiance is relatively less important. However, since $\beta_{gs\lambda} \propto \lambda^{-4}$ while $\beta_{ps\lambda} \propto \lambda^{-1}$, aerosol scattering is relatively more important at longer wavelengths. Aerosol scattering is also greatly enhanced after volcanic eruptions, in the presence of stratospheric clouds, or in the troposphere where very large particulate optical depths can occur.

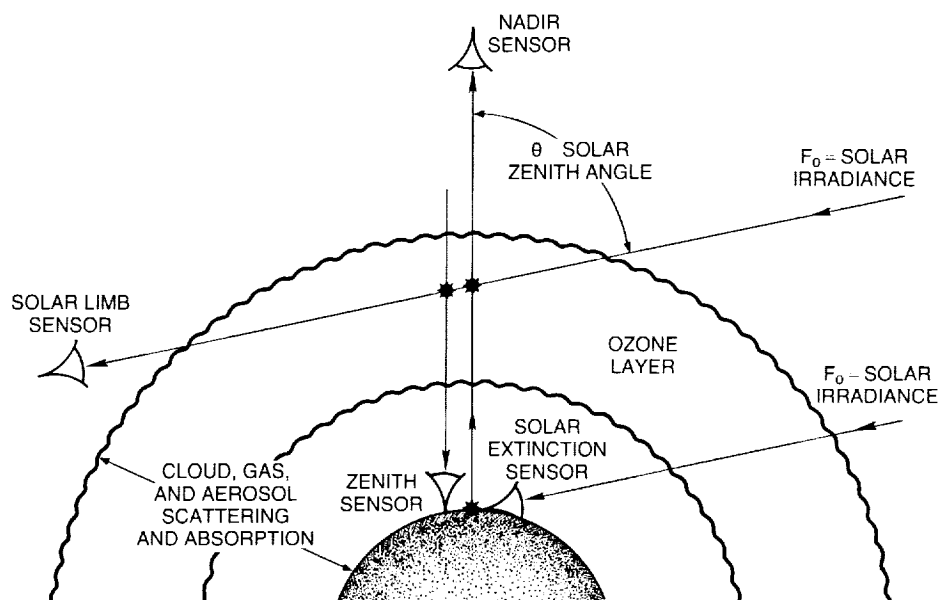


Figure 10.1 Geometries for ozone passive remote sensing. Configurations for both space-based and ground-based sensors are indicated.

It should be noted that multiple scattering is often ignored (at least in its details) in the analysis of stratospheric remote sensing data. A discussion of the analytical approaches employed in ozone remote sensing is given in Chapters 2 and 3. In full generality, the solution for remote sensing involves multiple-nested integrations over particle sizes, ray paths, and diffuse radiation fields, and may involve a further integration over wavelength and instrument band-pass function.

Most atmospheric aerosols exhibit only weak absorption at visible wavelengths (i.e., $\eta_i \sim 0$ and $\omega_0 \sim 1$). Moreover, the normal particle-size dispersions encountered in atmospheric settings yield extinction coefficients that vary with wavelength approximately as λ^{-1} . From the previous exposition, and the known properties of atmospheric aerosols including dependencies on wavelength, the simple λ^{-1} rule should be used only as a rough representation.

Complications to the above analysis arise from anisotropic scattering by particles, polarization effects, and the presence of nonspherical particles. Because large particles (exceeding a few tenths of a micron in size) have restricted sources and very short residence times in the upper atmosphere, their concentrations are typically quite low. On the other hand, the optical properties of very small nonspherical particles may still be adequately described using the Rayleigh theory. Corrections for anisotropy also can be made empirically. Hence, these complications may be treated in data retrieval algorithms.

10.2.4 Measured Properties of Aerosols

Measurements of atmospheric aerosols generally yield a specific property or subset of properties of the particles under observation. However, the analysis of satellite radiances may call for other properties that must be inferred from the measurements. For example, a lidar can measure the light backscatter efficiency for an aerosol, but a satellite sensor may detect the light scattered at some other, arbitrary angle. Or an aerosol size distribution may be measured in situ

at a few discrete points, and the entire size range fit to a standard distribution from which optical coefficients are then calculated.

Some of the commonly measured parameters are:

- Total extinction optical depth of the atmosphere, $\tau_{e\lambda}$, by observation of solar attenuation; typically, $\tau_{e\lambda}$ is referred to the zenith even when slant observation paths are used. The extinction optical depth is thus the height integral of the extinction coefficient (or extinction profile).
- Integrated lidar backscatter coefficient, with units of sr^{-1} , defined as the altitude integral of the measured backscatter coefficient, $\beta_{b\lambda}$. Because the backscatter coefficient involves an integral over the aerosol size distribution (see Section 10.2.3), the backscatter coefficient may be related to the total aerosol mass if the particle size distribution parameters can be determined independently.
- Lidar backscatter ratio, at each point along the observation path, is the ratio of the measured total aerosol plus molecular Rayleigh backscatter intensity (for light scattered from the lidar beam) to the modeled (or otherwise determined) Rayleigh (clear air) backscatter intensity alone.
- Volume scattering ratio, which is the quotient of the total light scattering from a unit volume of air (integrated over all angles, for all particles and gases), to the scattering caused by air molecules alone. For nonabsorbing aerosols, the volume scattering ratio is equivalent to the extinction ratio, defined in an analogous manner for a unit length of the observation path.
- Particle size ratio, defined as the quotient of the number of particles that are larger than two specific radii (usually 0.15 and 0.25 μm).
- Aerosol mass mixing ratio, defined as the mass mixing fraction of particles, either measured directly using aerosol filter collection techniques or deduced from size distribution measurements as

$$M_p = \int_0^\infty \frac{4}{3}\pi r^3 \rho_p n_p(r) dr,$$

where ρ_p is the particle density (g/cm^3).

- Lidar depolarization ratio, defined as the intensity of the backscattered light, after filtering by a polarizer set 90° to the polarization of the incident lidar beam, divided by the intensity of the incident linearly polarized beam; generally speaking, more irregular particles will produce larger depolarizations than more spherical particles, thus allowing some discrimination between liquid and solid aerosols.

10.2.5 Aerosol Microphysical Parameters

In dealing with atmospheric aerosols and their differences from gaseous species, several key microphysical processes must be defined. Detailed descriptions of these microphysical processes are available (Twomey, 1977; Pruppacher and Klett, 1978). Among the more important processes (see Table 10.2 and Turco et al., 1982) are:

AEROSOL ABUNDANCES AND DISTRIBUTIONS

Gravitational Sedimentation

Particles will fall relative to the surrounding atmosphere under the influence of gravity. For particles in the submicron size range at stratospheric altitudes, the fallspeed is roughly proportional to the particle radius. With a particle density of 1 g/cm^3 , the fall velocity of a $0.1 \text{ }\mu\text{m}$ radius spherical aerosol at 20 km is about $3 \times 10^{-3} \text{ cm per second}$, or about 1 km per year. In this particle size regime, the fall velocity is proportional to the particle density and inversely proportional to the air density (see Table 10.2).

For particles greater in radius than a few microns, the fall velocity is roughly proportional to the particle radius squared. Thus, a $10 \text{ }\mu\text{m}$ radius particle of unit density at 20 km would fall at about 2.5 cm per second, or about 2 km per day. The fallspeed is proportional to the particle density and is approximately independent of the air density (and thus height) in this size regime.

Coagulation

The collision and adhesion of small particles undergoing Brownian diffusion is the primary coagulation mechanism for stratospheric aerosols. For the purpose of estimating stratospheric time scales, a coagulation coefficient, K_c , of $1 \times 10^{-9} \text{ cm}^3 \text{ per second}$ is appropriate, and the time constant for coagulation is

$$t_c = (K_c n_o)^{-1},$$

Table 10.2 Time Constants* for Aerosol Processes

Process	Time constant	Conditions
1. Sedimentation** $\tau \approx \Delta z/v_f(r)$	$\approx 4 \times 10^7 \text{ sec}$	$0.1 \text{ }\mu\text{m}$ radius unit density ($\rho = 1 \text{ g/cm}^3$) ice sphere falling 1 km at 20 km altitude ($p = 50 \text{ mb}$)
$v_f(r) \propto \rho r^\alpha / p^\beta$	$\approx 3 \times 10^6 \text{ sec}$	$1 \text{ }\mu\text{m}$ particle
$1 \leq \alpha \leq 2$	$\approx 7 \times 10^4 \text{ sec}$	$10 \text{ }\mu\text{m}$ particle
$1 \geq \beta \geq 0$	$\approx 10^3 \text{ sec}$	$100 \text{ }\mu\text{m}$ particle
2. Coagulation $\tau \approx 1/[n_o K_c(r)]$	$\approx 10^8 \text{ sec}$	$1 \text{ }\mu\text{m}$ radius particle with $n_o = 10/\text{cm}^3$ $K_c = 10^{-9} \text{ cm}^3/\text{sec}$
3. Condensation/ evaporation $\tau \approx c \frac{r(S+1)}{p\xi S}$	$\approx 10^5 \text{ sec}$	$1 \text{ }\mu\text{m}$ radius particle at 10% supersaturation ($S = 0.1$) at 20 km ($p = 50 \text{ mb}$) for 1 ppbv of condensing vapor ($\xi = 1 \times 10^{-9}$). A unit accommodation coefficient is assumed.
$S = \left \frac{n}{n_v} - 1 \right $		

*Time constants may be estimated for other conditions by scaling according to the parameter relationships given (from Hamill et al., 1988).

**For submicron particles, $\alpha \approx 1$ and $\beta \approx 1$; for supermicron particles, $\alpha \approx 2$ and $\beta \approx 0$.

where n_0 is the background particle concentration (number/cm³). For a typical stratospheric aerosol abundance of about 10/cm³, the coagulation time constant is ~3 years. Hence, coagulation is important primarily with enhanced particle concentrations, as may occur following major volcanic eruptions.

Condensational Growth

The growth of aerosols by the condensation of a vapor depends on the concentration of the vapor in the vicinity of the particle, the supersaturation of the vapor (i.e., the ratio of its concentration to its equilibrium vapor pressure at the ambient temperature, minus unity—or $S = n/n_v - 1$), and the particle radius. Because of the complexity of these dependencies, growth rates are more difficult to estimate than settling and coagulation rates. To grow a spherical droplet of 1 micron radius at 20 km in a vapor with a concentration of 1 ppbv and a supersaturation of 10 percent would take about 1 day. Table 10.2 gives an approximate relation for scaling this growth rate to other conditions.

The evaporation of volatile aerosols can occur on even shorter time scales when the air mass holding the aerosols is heated, because the vapor pressures of the volatile components usually increase exponentially with increasing temperature.

10.3 LONG-TERM AEROSOL DATA BASES

In order to understand the effects of aerosols on ozone trend analyses, the long-term behavior of upper atmospheric aerosols must be known. Although long-term data sets have been obtained at a few fixed observational sites during the last 10 to 30 years, these data pertain to specific aerosol characteristics such as broadband spectral transmissions, laser radar (lidar) backscatter at fixed wavelengths, or particle size distributions above certain threshold sizes. Some systematic information is also available from in situ aircraft and balloon sampling and airborne remote sensing, but these data sets generally correspond to shorter time intervals. Of the types of measurements noted, the lidar observations provide the longest data base at multiple sites, although all of the data sets extending over several years or more were taken in the Northern Hemisphere above about 19°N. For example, lidar data are available from the NASA Langley Research Center (37°N, Hampton, Virginia) from 1974. The University of Wyoming (41°N) balloon sampling program offers a 15-year data base for specific aerosol properties obtained through a consistent series of measurements. A global data base has evolved from satellite observations by the SAM-II, SAGE-I, SAGE-II, and SME systems beginning in 1978; thus, archived satellite data now span a period of about 5 years.

10.3.1 Mauna Loa Observations

Figure 10.2 shows the longest continuous aerosol data base known. The observations have been recorded at Mauna Loa, Hawaii (19°N), since 1958 using an Eppley normal-incidence pyrheliometer to measure the broadband (290–2,500 nm) solar transmission of the atmosphere. Figure 10.2 gives the difference between the measured total transmission and a transmission calculated for a Rayleigh-scattering atmosphere without aerosols. Water vapor effects, which are not considered significant for the broadband transmission, are not included in the analysis. The largest features in the plotted residual transmission deficits are associated with perturbations (actually decreases in transmission) caused by the volcanic eruptions of Agung in 1963 and El Chichón in 1982. There also appear to be seasonal variations in the residual (aerosol) transmissivity, although the signals are quite small.

AEROSOL ABUNDANCES AND DISTRIBUTIONS

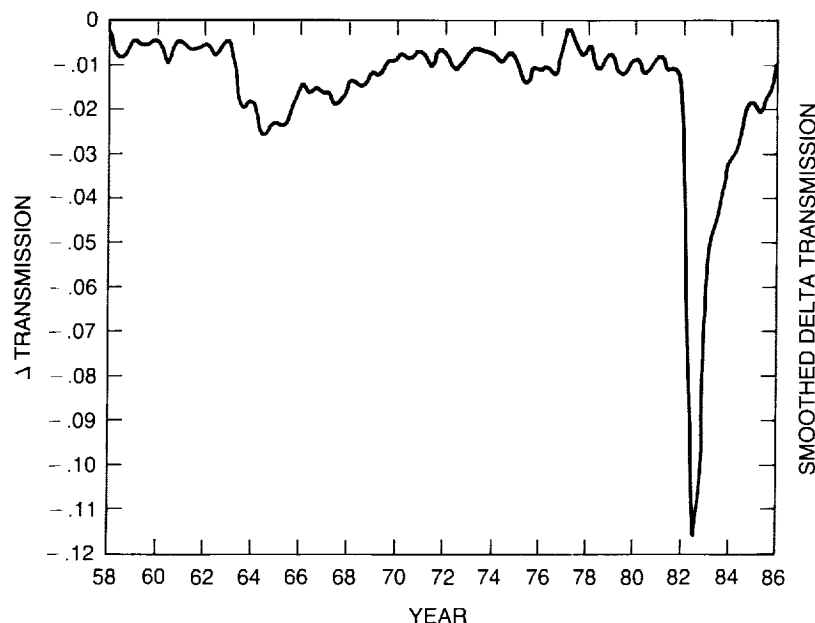


Figure 10.2 Decrease in direct solar transmission due to aerosol turbidity (extinction) at Mauna Loa, Hawaii, from 1958 to 1986, based on broad-band solar pyrheliometer measurements (J. DeLuisi, private communication, 1987).

As mentioned in the introductory comments, lidar systems have contributed significantly to the knowledge of the long-term behavior of stratospheric aerosols, at Mauna Loa and elsewhere. Lidar systems project a pulse of coherent laser radiation into the atmosphere and collect with a telescope the radiation that is backscattered toward the transmitter (Fiocco and Grams, 1964; Fox et al., 1973). In modern systems, the laser pulse at a fixed wavelength is about 10 meters in length. The delay between pulse transmission and backscatter collection provides a means of determining the distance of individual scattering elements from the instrument. The range-resolved backscatter intensity yields a profile of the scattering elements along the beam path. The background molecular scattering component is removed by normalizing the scattered intensity in a region where few aerosols are believed to exist (e.g., near the tropopause, or at ~ 30 km). The integrated differential backscatter along the beam path is a measure of the total aerosol mass or optical depth along the path, after assumptions are made about the particle size distribution, composition, and shape.

Because of the vertical profiling capability of lidars, and the relatively high mixing ratios of particles in the lower stratosphere, lidars have found extensive use as remote stratospheric aerosol sounders. Table 10.3 summarizes the lidar sites worldwide that have long-term (more than 3-year) operations.

Figures 10.3a and 10.3b show integrated aerosol backscatter versus time from 1974 to the present for the lidar systems located at Mauna Loa and Hampton, respectively. On the abscissa are indicated the volcanic eruptions that could have perturbed the stratospheric aerosol significantly. A comparison of the lidar records in Figures 10.3a and 10.3b show differences that reflect the widely separated geographical locations of the instruments, the frequency of sampling, and the variation in temporal and spatial responses of the aerosol layer to volcanic influences. Following the El Chichón eruption in 1982, the lidar signals have been dominated by a steady decay of the stratospheric aerosol layer (see Section 10.4 for a complete discussion).

Table 10.3 Sites of Long-Term Aerosol Lidar Observations

Location	Latitude	Longitude	Dates
Mauna Loa, Hawaii; National Oceanic and Atmospheric Administration	19.5°N	156.6°W	1974 to Present
Hampton, Virginia; NASA Langley Research Center	37.1°N	76.3°W	1974 to Present
Garmisch-Partenkirchen, West Germany; Fraunhofer Institute for Atmospheric Environmental Research	47.5°N	11.0°E	1976 to Present
Tsukuba/Yatabe, Japan; National Institute for Environmental Studies	36.0°N	140.0°E	1983 to Present
Verrieres le Buisson, France; Observatoire de Haute Provence	43.9°N	5.7°E	1981 to Present
Aberystwyth, Wales; University College of Wales	52.4°N	4.1°W	1985 to Present
Fukuoka, Japan; Kyushu University	33.7°N	130.4°E	1983 to Present

10.3.2 University of Wyoming Dustsonde

The basic dustsonde instrument flown by the University of Wyoming research group is a balloonborne light-scattering photoelectric-detector particle counter. Basically, the instrument measures the number of particles in air drawn through the detector, from which the ambient particle concentrations are deduced. The system employs a coincidence sensor to eliminate spurious counting caused by cosmic rays at high altitude and to reduce Rayleigh-scattering background at low altitudes. The development of the instrument began in 1961, and the first flight occurred in August 1963, just after the Agung volcanic eruption (Rosen, 1964). Systematic measurements were not begun until October 1971 from Laramie, Wyoming (41°N). The pre-1971 soundings lacked a reliable calibration scheme, and cannot easily be compared quantitatively to later measurements.

It is usually assumed—based on observational evidence—that the background stratospheric aerosols (as well as aged volcanic aerosols) are supercooled liquid droplets and, hence, also spherical (Rosen, 1971). This allows reliable theoretical (Mie scattering) calculations of the aerosol optical properties, as well as confident analytical interpretation of data obtained with light-scattering instruments such as the dustsonde. The response of the dustsonde to spherical nonabsorbing particles of varying size and index of refraction has been studied in considerable detail (Pinnick et al., 1973; Pinnick and Hofmann, 1973). These investigations show that for particle sizes below about 0.25 μm radius, the response of the instrument is strictly single valued and not very sensitive to index of refraction. Further, because the response is proportional to a high power of the particle size, small errors in the signal discrimination level do not lead to significant errors in the deduced particle size.

AEROSOL ABUNDANCES AND DISTRIBUTIONS

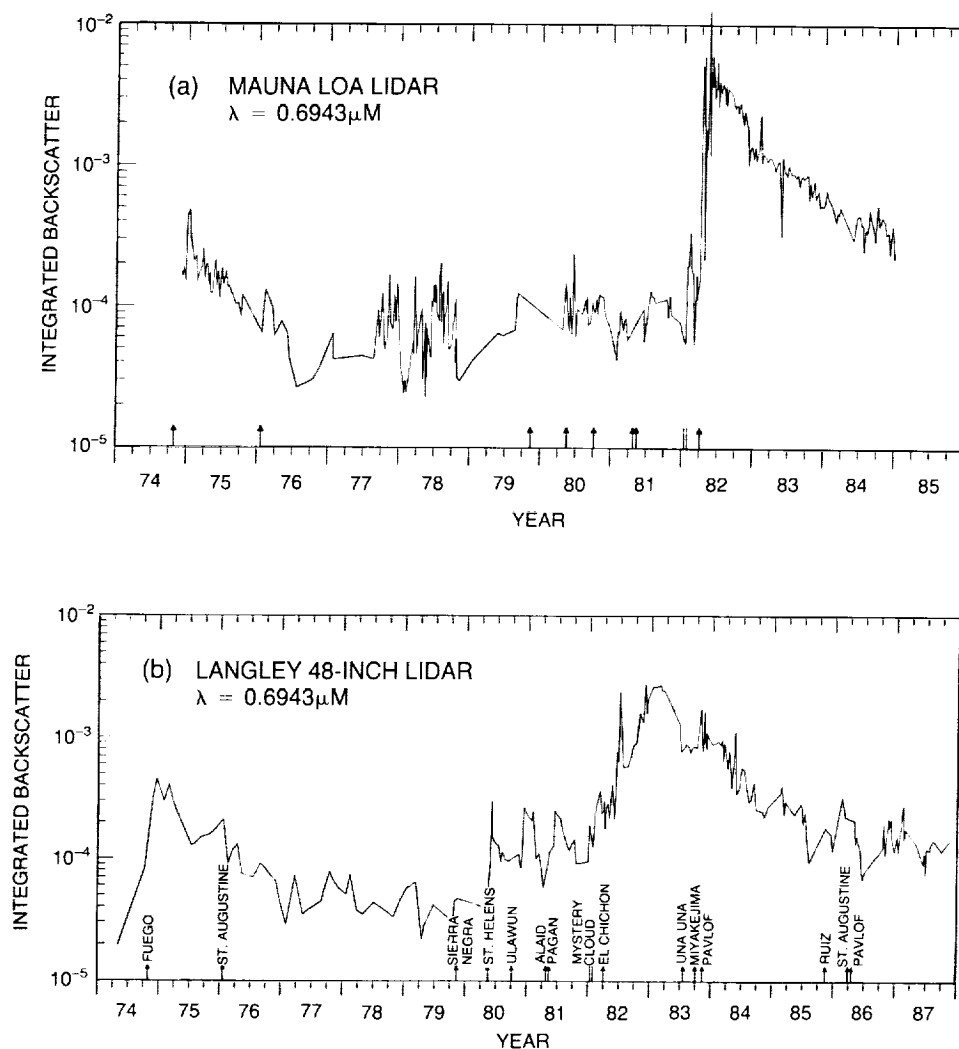


Figure 10.3 Integrated lidar backscatter intensities over the decade 1974 to 1985 for a wavelength $0.6943 \mu\text{m}$ at two sites: (a) Mauna Loa (DeLuisi et al., 1982; J. DeLuisi, private communication, 1987); (b) Hampton, Virginia (M.P. McCormick, private communication, 1987). The backscatter radiance includes contributions from air molecules and aerosols. The data correspond to the stratospheric component of the scattering.

Since about 1970, the basic dustsonde has been adjusted to detect particles with radii $>0.15 \mu\text{m}$ and $>0.25 \mu\text{m}$. These are the two operational channels most commonly used, although the instrument can be set to operate over a much wider range of sizes. The cosmic ray interference (from scintillation in the glass of the photodetectors) effectively limits the aerosol detection threshold to about 10^{-2} particles/ cm^3 in the $0.15 \mu\text{m}$ channel and to about 10^{-4} to 10^{-3} particles/ cm^3 in the $0.25 \mu\text{m}$ channel.

The standard two-channel dustsonde measurement is subject to uncertainties associated with the sample flow rate, sharpness of the size discrimination, statistical fluctuations in the counting rate, calibration accuracy, and particle index of refraction (Russell et al., 1981). The net uncertainty in measured stratospheric aerosol concentrations is estimated to be about 10 percent. The reproducibility of measurements is considerably better than 10 percent, however; identical instruments flown in parallel typically agree to within a few percent (Hofmann et al., 1975).

The standard dustsonde has been applied in other configurations to measure the "total" aerosol concentration ($>0.01\ \mu\text{m}$, often referred to as "condensation nuclei" or cn), or the concentration of very large particles ($>1\ \mu\text{m}$) in the atmosphere (Rosen and Hofmann, 1986). In practice, the lowest particle concentration that can be observed with the modified dustsonde is $\sim 10^{-6}/\text{cm}^3$.

Although the concentration of the largest particles may be measured only to within an order of magnitude, the total aerosol mass determined by integrating the measured size distribution may have as little as ~ 10 percent uncertainty. Comparisons between direct measurements of stratospheric aerosol mass (and optical properties) and values calculated from dustsonde data generally agree to within 10 percent (Russell et al., 1981; Rosen and Hofmann, 1986).

Dustsondes also have been used to examine the correlation between the structures in aerosol and ozone profiles (Rosen, 1966 and 1968). Figure 10.4 illustrates a very distinct ozone/aerosol layer at 11 km transported from more northerly latitudes; the layer has descended several kilometers over the horizontal range, bringing ozone- and aerosol-rich air to low altitudes. Such circumstances are frequently observed at midlatitudes, emphasizing the role of ozone transport compared to chemical processes at these altitudes. The correlation of aerosol and ozone profiles in polar regions may, therefore, represent an important diagnostic for high-latitude dynamics and chemistry, including the seasonal formation of the "ozone hole."

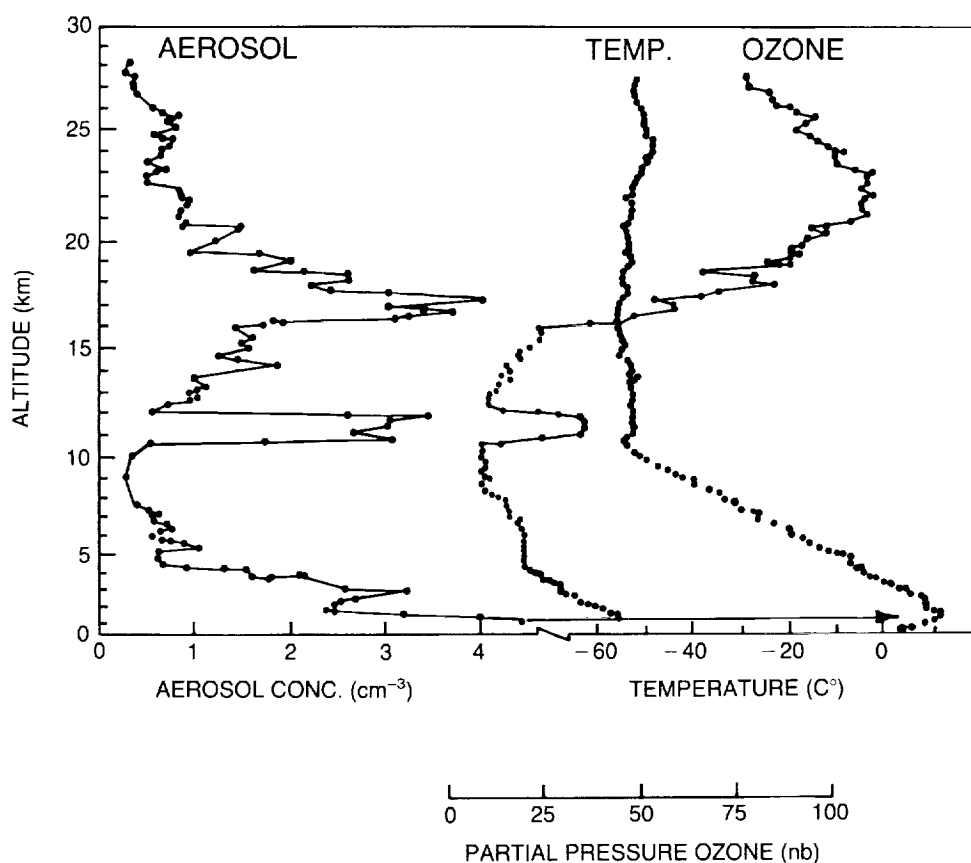


Figure 10.4 Simultaneously measured aerosol and ozone profiles over Minneapolis, Minnesota, on December 22, 1965. The aerosol concentration corresponds to particles with sizes greater than about $0.15\ \mu\text{m}$ radius (Rosen, 1966).

AEROSOL ABUNDANCES AND DISTRIBUTIONS

Figure 10.5 illustrates results obtained with the dustsonde expanded to six size channels during a volcanically disturbed period. First, as is usually the case even under background conditions, the total aerosol population ($r > 0.01 \mu\text{m}$) exhibits a fundamentally different profile than the concentration of larger particles, with no relative maximum of the former at the level of the classical "Junge" layer. Also note, however, the unusual circumstance that a cirrus cloud can be identified in the sounding by the fact that the two largest particle channels show exactly the same counting rate, indicating that the particles are larger than the size thresholds for these channels and have a low concentration. The cirrus cloud does not appear to have affected the concentrations of the smaller aerosols.

Long-term observation of the stratospheric aerosol layer using the dustsonde (and lidar) clearly shows that volcanic eruptions cause the most prominent changes in the layer. Figure 10.6 gives the peak mass mixing ratio of the aerosols deduced from dustsonde measurements of the aerosol size distribution since about 1972. The eruption of El Chichón in 1982 obviously caused the largest perturbation since the beginning of the dustsonde measurements. Moreover, El Chichón was apparently the only eruption in the last 15 years to produce a large and persistent increase in the average particle size. Even as late as May 1987, the stratosphere had not completely recovered from the El Chichón event. Smaller eruptions such as Nevado del Ruiz (5°N , November 1985) may have delayed somewhat the recovery of the upper atmosphere from El Chichón.

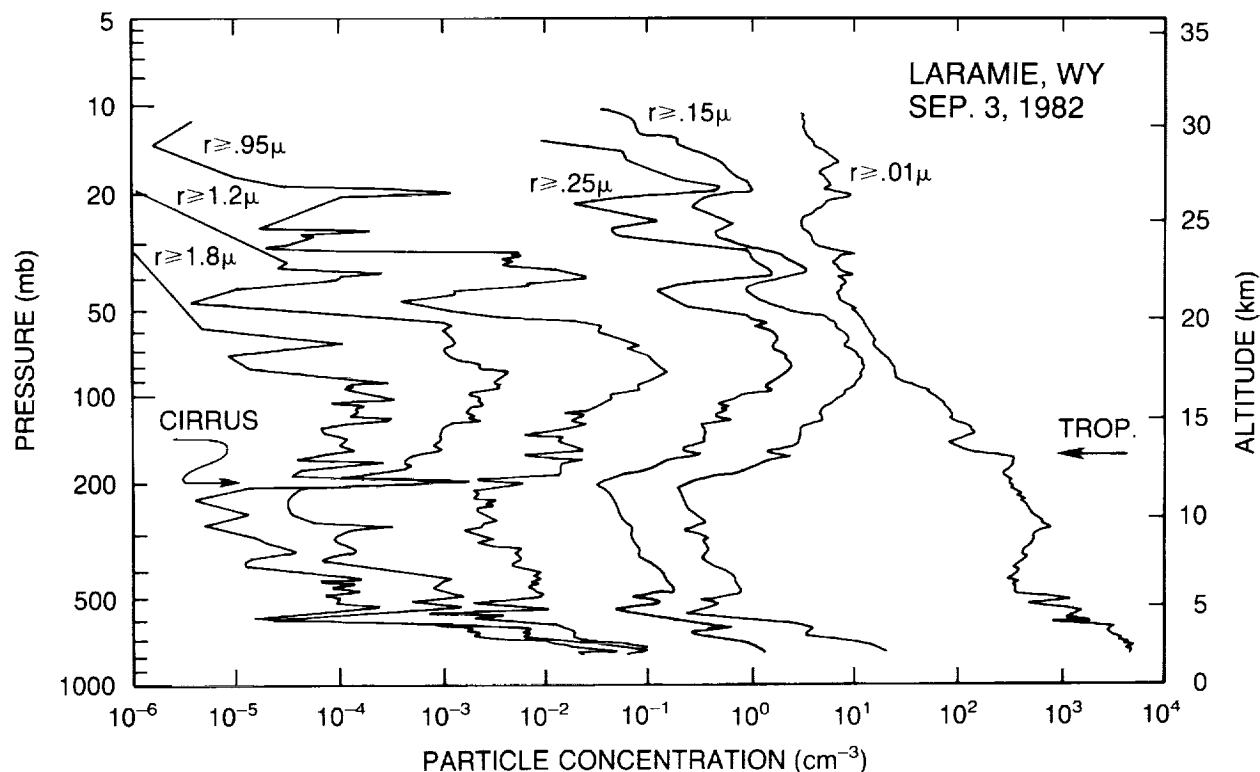


Figure 10.5 Aerosol vertical profiles obtained with the six-channel dustsonde. The concentrations range over 10 orders of magnitude. A subtle anomaly in the profiles associated with a cirrus cloud layer is indicated; although the cirrus cloud could be seen in the sky on the day of the sounding, it is nevertheless difficult to detect in the measured aerosol profiles (Rosen and Hofmann, 1977).

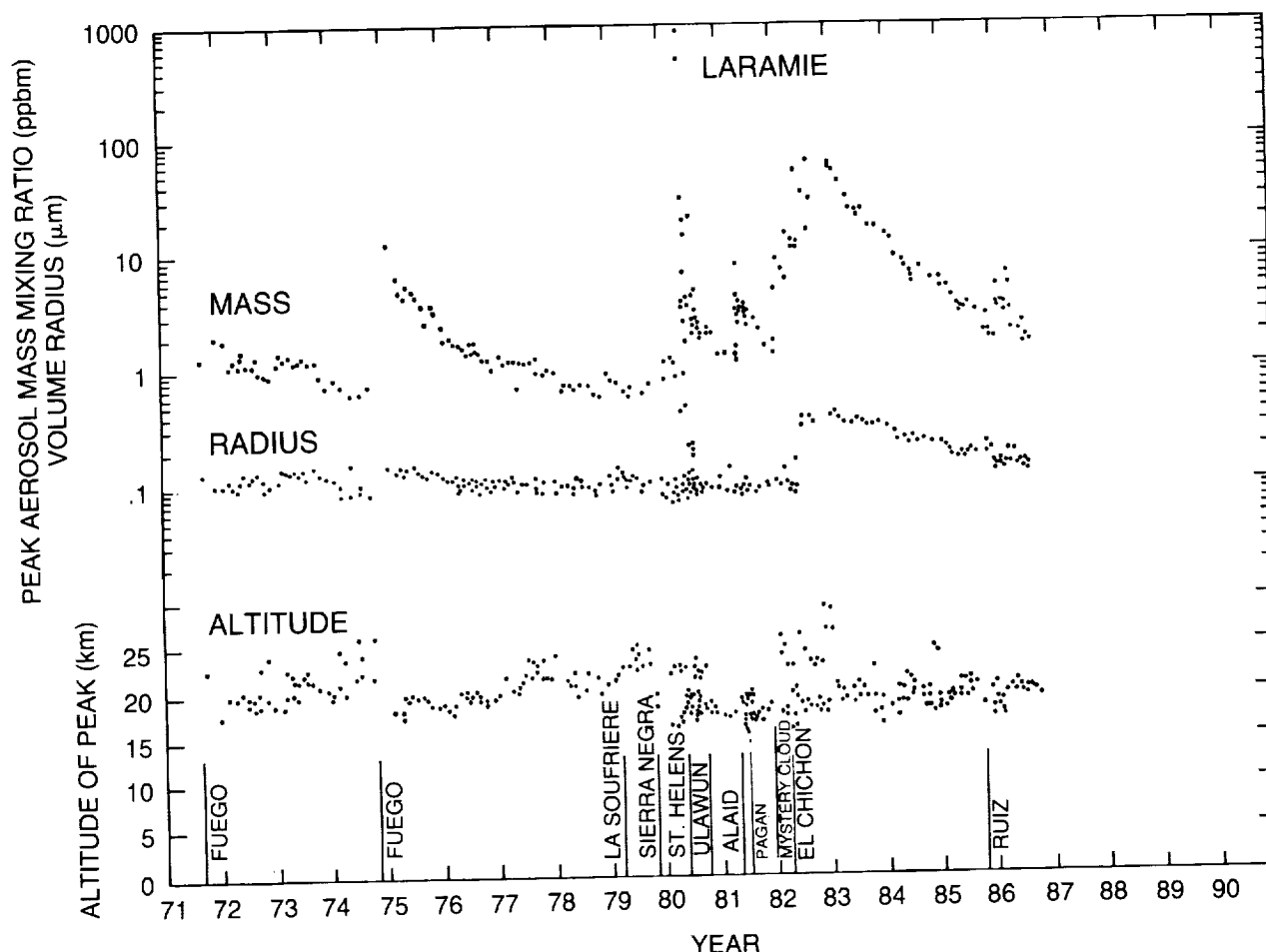


Figure 10.6 Time development of the peak mass mixing ratio of the stratospheric aerosol layer over Laramie, Wyoming, during the entire period of regular dustsonde operations at that site. Also shown are the altitude of the mass peak and the average volume-weighted particle radius at that height. The abrupt change in the mass peak and the average volume-weighted particle radius in 1982 is associated with the eruption of El Chichón. The calculations of aerosol mass from the measured aerosol size data are described by Rosen and Hofmann (1986).

10.3.3 Satellite Systems: SAM, SAGE, SME

10.3.3.1 SAM and SAGE

Table 10.4 lists satellite instruments that have collected data bearing on the long-term behavior of stratospheric aerosols. The SAM-II (Stratospheric Aerosol Measurement II) and SAGE (Stratospheric Aerosol and Gas Experiment) systems were developed specifically for performing stratospheric aerosol measurements by the technique of solar limb extinction (McCormick et al., 1979; also see Chapters 2 and 3). During each spacecraft sunrise or sunset, the instrument locks onto the centroid of the Sun's disc in azimuth (yaw) and scans vertically across the disc with an optics field of view of about 0.5 arc minutes. The instrument continues to track the Sun as it rises or sets with respect to the spacecraft. The small field of view provides roughly a 1 km vertical resolution for the observations. In obtaining data well above the limb (atmosphere) during each sunrise or sunset event, the measurements are self-calibrated relative to the absolute solar irradiance.

AEROSOL ABUNDANCES AND DISTRIBUTIONS

Table 10.4 Long-Term Aerosol Measurements From Satellites

Satellite Instrument*	Period of Operation	Aerosol Channel(s) (μm)	Lower Altitude Limit	Latitude Coverage
Solar limb extinction				
SAM-II	October 1978 to Present	1.00	Surface	64°–80°N 64°–80°S
SAGE-I	February 1979 to November 1981	1.02 0.45	Surface 10 km	75°S–75°N
SAGE-II	October 1984 to Present	1.02 0.53 0.45 0.38	Surface 6.5 km 10.5 km 14.5 km	80°S–80°N
Solar limb scattering				
SME	October 1981 to October 1986	0.44	30–50 km	Sunlit latitudes; 3–5 longitudes per day

*For additional specifications on these satellite systems, see Chapter 2.

For aerosol observations, SAM-II, SAGE-I, and SAGE-II all use a primary spectral channel at 1.0 μm wavelength. Both SAGE instruments also use a second channel at a shorter wavelength to obtain information on the wavelength dependence of the aerosol extinction. In the case of SAGE-I, measurements are made simultaneously for ozone and nitrogen dioxide absorption; in the case of SAGE-II, water vapor near-infrared absorption is also measured. These additional data are used to make small corrections to the aerosol measurements (and to deduce the ozone, NO_2 , and water vapor profiles, as discussed in Chapter 3). Forward scattering of light by the aerosols does not introduce a significant error in these systems.

The basic aerosol property measured by the SAM and SAGE instruments is the path-integrated aerosol extinction at one wavelength (1 μm) versus the tangent altitude of the solar ray. The path extinctions for various tangent heights are converted to a vertical extinction profile using a homogeneous atmospheric shell model. The height integral of this extinction profile yields the vertical optical depth at 1 μm of the aerosols between the lowest and highest altitudes of the observations. In Figure 10.7 this optical depth is plotted for the altitude interval from 2 km above the tropopause to about 30 km; weekly averaged optical depths are given for SAM-II sunrise measurements, which occur over the Antarctic, and for SAM-II sunset measurements, which occur over the Arctic. Optical depths are calculated only for heights well above the tropopause to exclude the effects of high-altitude tropospheric clouds. For each SAM-II measurement, the altitude of the local tropopause is determined from the National Weather Service gridded analysis.

In Figure 10.7, strong effects are seen from volcanic eruptions that were powerful enough to inject into the stratosphere a large quantity of debris, some of which was subsequently transported to the polar region. The Arctic aerosols show strong effects of eruptions such as Mount St.

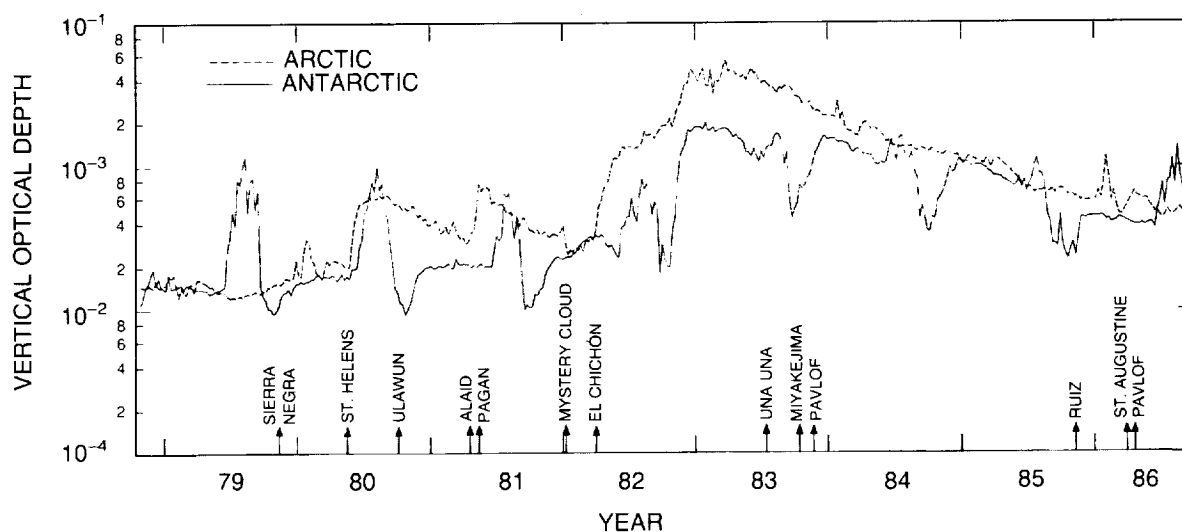


Figure 10.7 Optical depth of aerosols in the polar stratosphere at a wavelength of 1 micron measured by the SAM-II satellite from October 1978 through September 1986. Optical depths are given separately for the Arctic and Antarctic regions. The optical depths represent vertical projections of particle extinctions measured along satellite slant observation paths. A distinct seasonal variation is seen in the optical depth because of the formation of polar stratospheric clouds in the winter season; this variation is particularly noticeable in the Southern Hemisphere. The El Chichón aerosols also have an obvious effect on the polar optical depths in both hemispheres (McCormick and Trepte, 1987).

Helens (1980) and El Chichón (1982). The El Chichón eruption is also obvious in the Antarctic record, although most other eruptions (during the period of the SAM observations) are not. Notably, most of these eruptions were smaller, Northern Hemisphere events.

Clearly evident in the Antarctic aerosol record are the order of magnitude optical depth enhancements caused each austral winter by PSC's. These clouds are composed of ice and nitric acid condensed at temperatures below about 195 K (see Section 10.6). Interestingly, minimum optical depths are seen each austral spring in October, after stratospheric temperatures have warmed and the PSC's have evaporated, suggesting a cleansing of the upper atmosphere. However, by the first week of November, the winter polar vortex has weakened or moved off the pole; aerosols are thus advected from lower latitudes into the polar regions, increasing the optical depths there. Although PSC's are also evident in the Arctic aerosol record from December to February, they are much less frequent on a weekly average basis.

Volcanic aerosol injections can change the character of the seasonal variation in the polar aerosol optical depth. For example, particles generated by El Chichón partially masked the Antarctic winter PSC peak for several years, although the spring (October) aerosol minimum remained apparent.

The SAGE-I and -II instruments provide aerosol data for latitudes up to about 70°. The highly precessing orbits of these spacecraft (about 56° inclination) cause satellite sunrises and sunsets to vary over a wide range of latitudes each month. In Figure 10.8, a month of SAGE-I extinction profiles have been used to construct an average optical depth map for the Mount St. Helens eruption cloud in summer 1980. These data show a clear tendency for the aerosol to drift toward high latitudes and the persistence of inhomogeneities in the aerosol clouds. Both effects are relevant to the observation of ozone using techniques that are sensitive to the presence of aerosols.

AEROSOL ABUNDANCES AND DISTRIBUTIONS

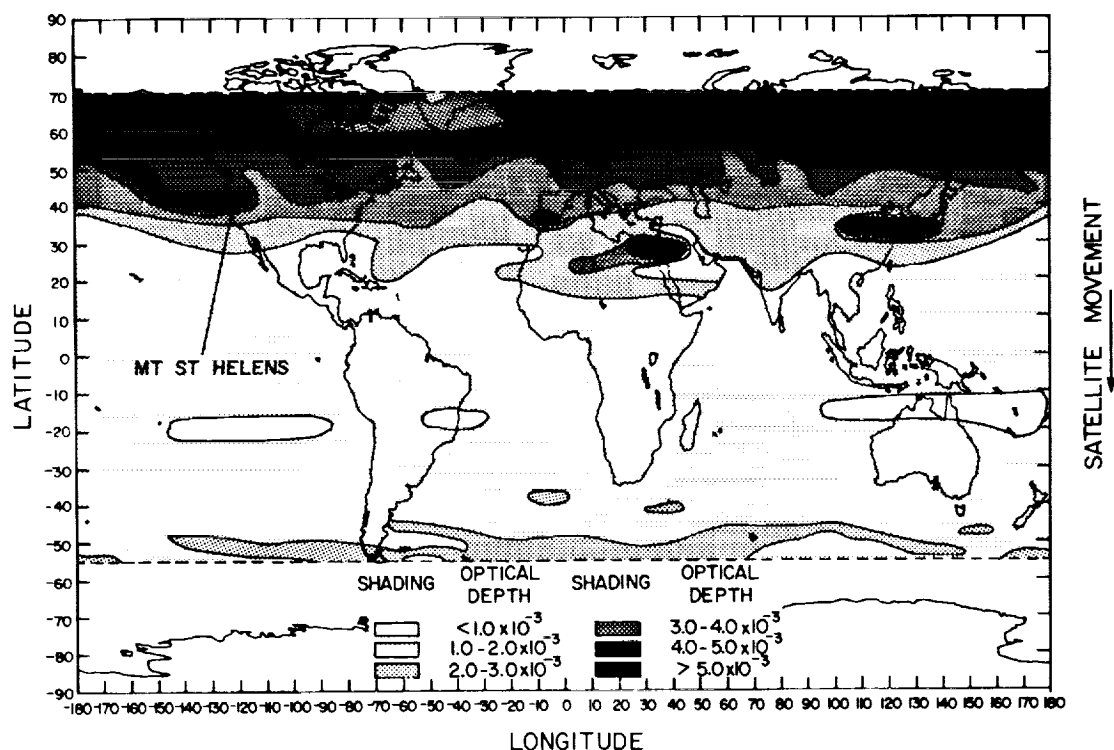


Figure 10.8 Global distribution of the aerosol optical depth (measured at a wavelength of $1\ \mu\text{m}$) roughly 2.5 months after the eruption of Mount St. Helens in May 1980. The map was constructed using approximately 450 SAGE satellite observations for the period July 21 to August 26, 1980. Particularly noteworthy is the heavy concentration of volcanic aerosol at high northern latitudes (the eruption occurred at 46°N) (Kent and McCormick, 1984).

10.3.3.2 SME

The Solar Mesosphere Explorer (SME) satellite was launched on October 6, 1981, into a near-polar Sun-synchronous orbit. The mission was designed to provide stratospheric and mesospheric limb sounding profiles at $\sim 5^\circ$ latitude and 3.5 km altitude resolution for 3 to 5 longitudes per day for all sunlit latitudes. The SME complement of ultraviolet, visible, and thermal infrared spectrometers has operated continuously from the end of 1981 through the end of 1986. The extensive observations of stratospheric aerosols include data covering the El Chichón eruption of April 1982 (Barth et al., 1983).

The SME aerosol observations consist of two distinct remote-sensing techniques. The infrared observations, at $6.8\ \mu\text{m}$ and $9.6\ \mu\text{m}$, are sensitive to thermal emission from H_2SO_4 aerosol. Sulfuric acid has a very large imaginary index of refraction at these wavelengths ($>10^{-2}$), such that H_2SO_4 aerosols emit in the infrared with an intensity proportional to the total aerosol mass. The SME $6.8\ \mu\text{m}$ radiances were inverted to obtain stratospheric sulfate aerosol mass loading for 1982 to 1983, including the period of initial injection, peak mass loading, and initial decay of the aerosol perturbation (Thomas et al., 1983; see Figure 10.9, and note that the extinction at $6.8\ \mu\text{m}$ is normally much smaller than the extinction at visible wavelengths). The infrared analysis is relevant primarily for sulfate aerosols between 20 km and 30 km altitude, where the infrared aerosol emission was several times the expected emission from stratospheric water vapor (for which the SME $6.8\ \mu\text{m}$ channel was designed).

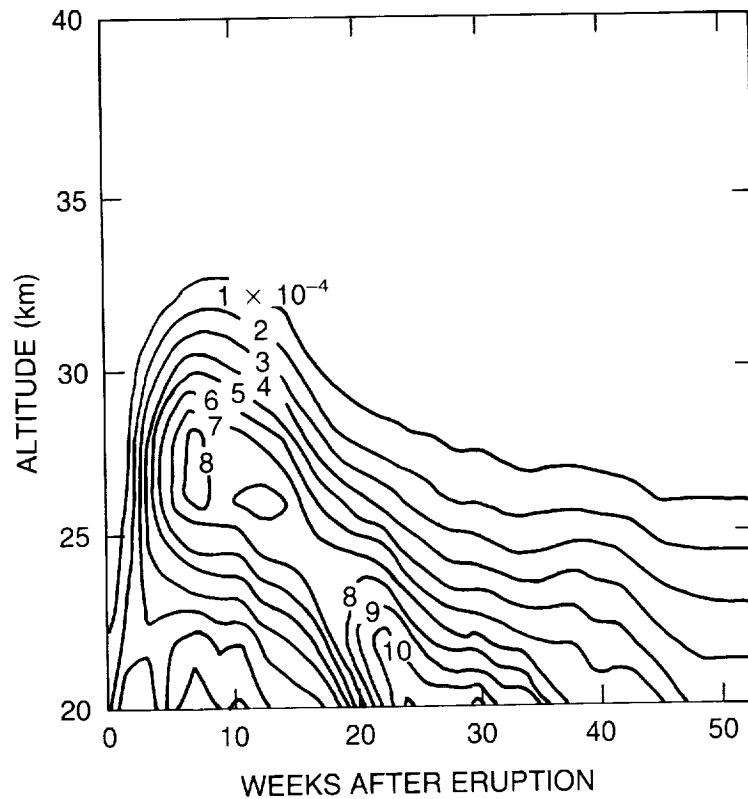


Figure 10.9 Contours of inferred vertical and temporal variations in the aerosol extinction at a wavelength of $6.8 \mu\text{m}$ (given in units of 10^{-4} km^{-1} , with values indicated on the contours) from SME infrared radiometer data for the first year following the El Chichón eruption of April 4, 1982 (Thomas et al., 1983).

A second independent set of aerosol observations was derived from limb profiles of visible sunlight scattered by the neutral atmosphere and aerosols in the middle and upper stratosphere (30 km to 50 km). These profiles indicate distinctly non-Rayleigh (nonmolecular) scale heights. The data were converted to volume-scattering ratios for 1982 to 1984 (Clancy, 1986). Inherent in the analysis scheme is the removal of any component of particle scattering that may be due to vertically well-mixed aerosol, as this radiance component would be interpreted as molecular scattering. Hence, the derived residual aerosol scattering may be a lower limit, although other factors contribute to uncertainties in the interpretation of the observed excess limb radiances.

The SME limb analysis has recently been extended through the middle of 1986 with significant improvements in the data processing and inversion schemes. Figures 10.10 and 10.11 display the latitudinal, vertical, and temporal behavior of the aerosol volume-scattering ratio derived from the SME visible-light (440 nm) limb profiles. Because the SME scattered-light observations are constrained to scattering angles between 40° and 130° , the volume-scattering ratios in Figures 10.10 and 10.11 depend on the assumed aerosol size distribution. A standard gamma distribution (mean radius = $0.1 \mu\text{m}$, variance = $0.05 \mu\text{m}$) was used in the data analysis. The uncertainty in the size distribution of the aerosol introduces a substantial uncertainty into the derived aerosol concentrations (see Section 10.2.3.3).

The SME observations suggest significant aerosol radiance effects above 30 km. For example, the data indicate that (1) the El Chichón eruption cloud had risen to an altitude of 30 km within 1 to 2 weeks after the eruption, then took 1 to 2 months longer to penetrate to 40 km, (2) a topside

AEROSOL ABUNDANCES AND DISTRIBUTIONS

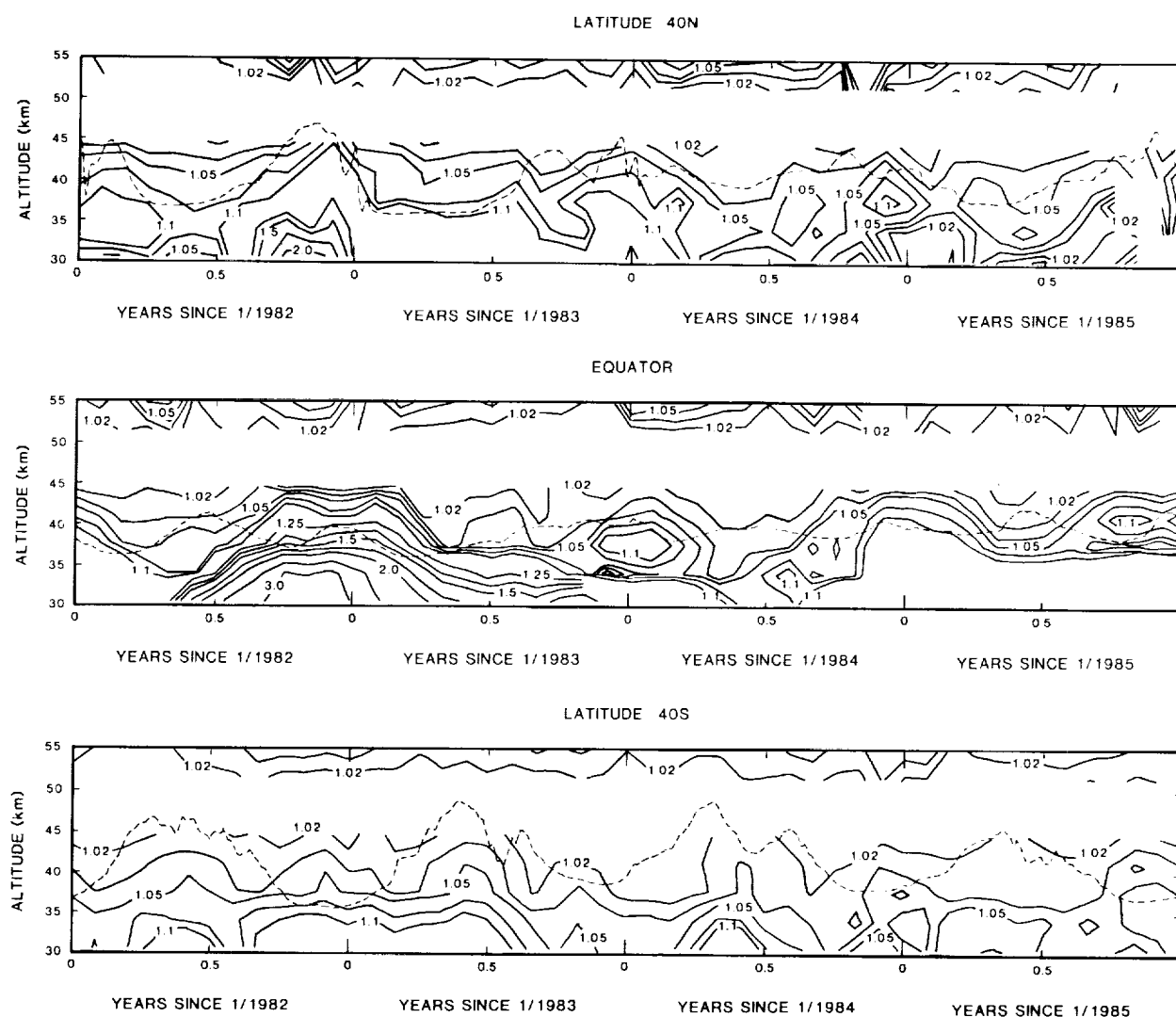


Figure 10.10 Contours of volume-scattering ratios at a wavelength of 440 nm from the SME visible spectrometer for observations at 40°N, the Equator, and 40°S, covering the period 1982 through mid-1986. The dashed line indicates the altitude at which an H_2SO_4 mass mixing ratio of 4×10^{-10} would be saturated, assuming NMC temperature and pressure profiles and a 75 percent sulfuric acid aqueous solution (R.T. Clancy, private communication, 1987).

boundary to the aerosol layer appeared to form near 40 km (possibly reflecting sulfuric acid vapor supersaturation only below this level, assuming a global average H_2SO_4 mixing ratio of about 4×10^{-10} ; see the dashed lines in Figure 10.10), (3) there may be a seasonal variation in the altitude of this topside boundary due to seasonal changes in stratospheric temperatures, (4) a 1-year lifetime may be deduced for the principal injection of El Chichón, with a much longer lifetime for the residual aerosol loading, and (5) a new enhancement of the upper aerosol layer in late 1985 may be partly associated with the Nevada del Ruiz eruption.

The overall uncertainty inherent in the SME visible-light scattering analysis for aerosols could be reduced through corroborative analyses using the SME 6.8 μm radiance data above 30 km. A

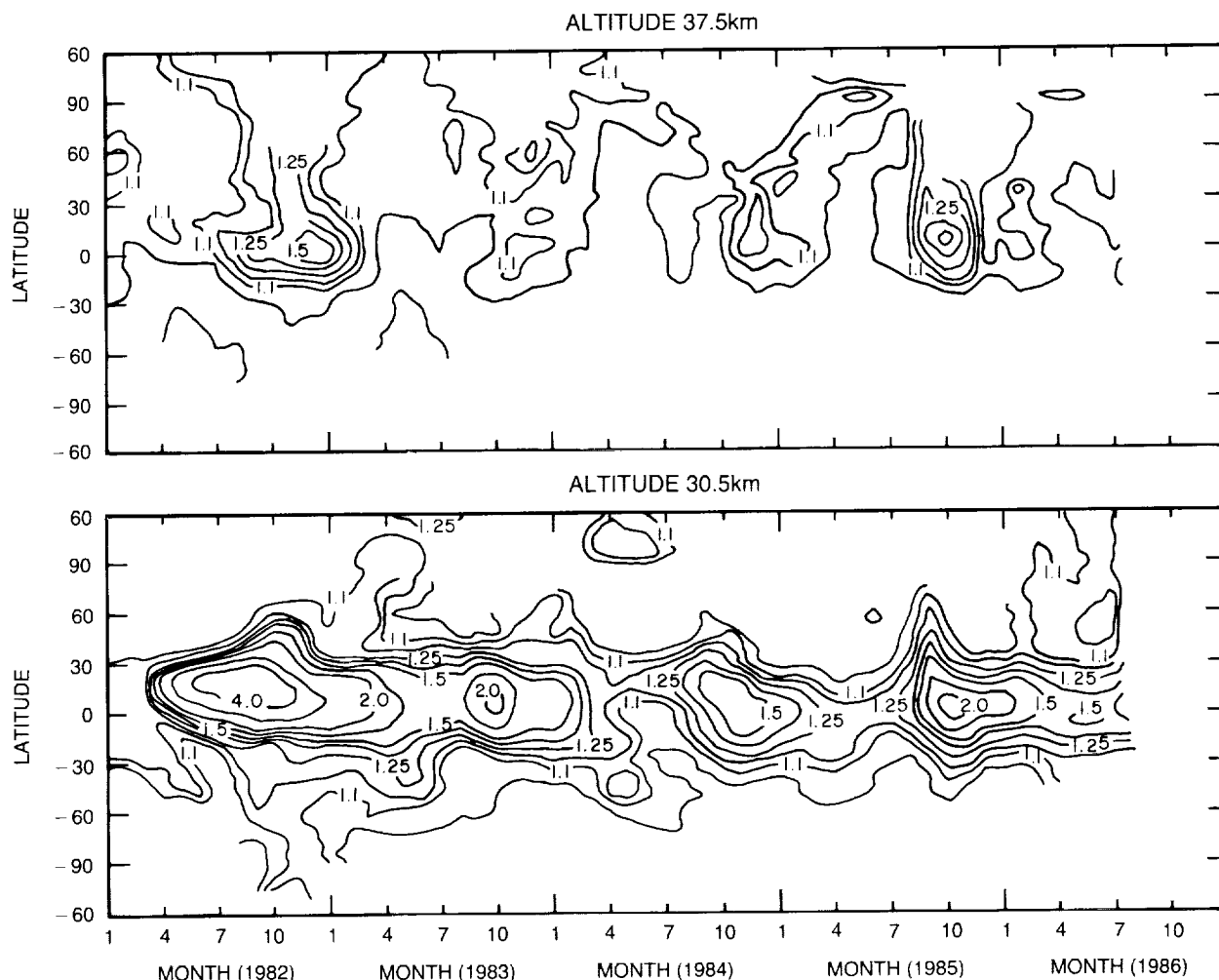


Figure 10.11 Time-longitude contours of SME visible-wavelength (440nm) volume-scattering ratios at equatorial latitudes, for altitudes of 37.5 km and 30.5 km (R.T. Clancy, private communication, 1987).

recent study of these radiances by Jakosky et al. (1988) also indicates substantial pre-El Chichón aerosol loading above 30 km from January–March 1982. Very preliminary results of visible–infrared comparisons in March 1982 and 1985 suggest that agreement between the two sets of SME data can be achieved if it is assumed that the aerosol between 30 km and 40 km consists of $\sim 0.1 \mu\text{m}$ radius sulfate particles with a peak concentration of $\sim 15/\text{cm}^3$ (mass mixing ratio of 2×10^{-9}).

The deduced particle number *concentration* is roughly consistent with values measured in situ by Hofmann and Rosen during February to March 1985 (i.e., $\sim 10\text{--}15/\text{cm}^3$ at ~ 30 km; J. Rosen, private communication, 1987). However, the particle size limits for these balloon observations are $0.01 \mu\text{m} < r < 0.15 \mu\text{m}$, with actual particle sizes probably lying closer to the smaller end (e.g., Rosen and Hofmann, 1983). Accordingly, the aerosol *mass* concentrations inferred from the Hofmann and Rosen data seem to be much smaller than those inferred above from the SME observations.

AEROSOL ABUNDANCES AND DISTRIBUTIONS

10.3.3.3 SAGE/SME Intercomparisons

On occasion, the SAM-II, SAGE-I and -II, and SME satellites obtain paired measurements that are nearly coincident in time and space. Hence, opportunities exist for intercomparing the aerosol properties obtained by these related sensors. Comparisons of the aerosol extinction profiles obtained with the SAM-II and SAGE-I (Yue et al., 1984) and with SAM-II and SAGE-II (Yue et al., 1989) show excellent agreement. The paired data sets, obtained using similar solar extinction techniques, appear to be self-consistent.

The SME satellite measures the scattering of solar rays at a specific scattering angle determined by the viewing geometry at the time of the observation. The SME data can be converted to equivalent volume-scattering coefficients (or extinction coefficients, since the two parameters are analogous for nonabsorbing aerosols) by assuming a particle size distribution, calculating a scattering phase function, and normalizing the observed scattering to the predicted phase function. Typically, the measurements are expressed in terms of the volume-scattering ratio (see Section 10.2.4). The conversion of raw observational data on scattered light to volume-scattering coefficients is very sensitive to the assumed particle size distribution used in the conversion calculation.

The SAM and SAGE systems measure the aerosol extinction directly (albeit along an oblique path). Measurements of extinction do not depend on the viewing angle, unlike measurements of scattering. Thus, extinction is a more easily defined property of aerosols. Because the size distributions of particles above ~ 30 km are highly uncertain, the conversion of scattering measurements to equivalent extinction profiles, or vice versa, is subject to significant error. An illustration of this problem is given in Figure 10.12, in which extinction ratios measured by SAGE are compared with equivalent volume-scattering ratios deduced from coincident SME scattering data using two particle size distributions. To achieve reasonable agreement near 30 km, the assumed SME particles must be of the order of $0.1 \mu\text{m}$ in radius; if the particles are assumed to have a radius of $0.045 \mu\text{m}$, the agreement is very poor. However, the implied aerosol mass with $r \sim 0.1 \mu\text{m}$ exceeds the direct measurements of aerosol mass that are available (see the discussion in the previous section). The SAGE instrument, which provides a direct measurement of extinction, has not detected significant aerosol effects above approximately 35 km. SME also shows small extinction ratios at altitudes above ~ 35 to 40 km, except during a short period following the El Chichón eruption.

It might be concluded that the inversion scheme applied to SME radiance measurements, which depends on knowledge of the aerosol-scattering phase function, requires more precise calibration. Such a calibration could be based on the SAGE extinction data, if these were more reliable at the higher altitudes. Tentatively, it is fair to conclude from the preliminary SAGE/SME intercomparison that there is little direct evidence for the presence of optically significant, widespread aerosol layers in the region above about 35 km.

10.4 AEROSOL PERTURBATIONS: EL CHICHÓN AND OTHER EVENTS

In previous sections, the observational basis for understanding upper atmospheric aerosols was established. In certain places, reference was made to perturbations of the aerosols, particularly those caused by major volcanic eruptions that directly inject huge quantities of dust and gas into the upper atmosphere. In this section, a more detailed account is given of knowledge of the most recent aerosol perturbations that might be expected to influence atmospheric radiances and, hence, the remote sensing of ozone concentrations and distributions.

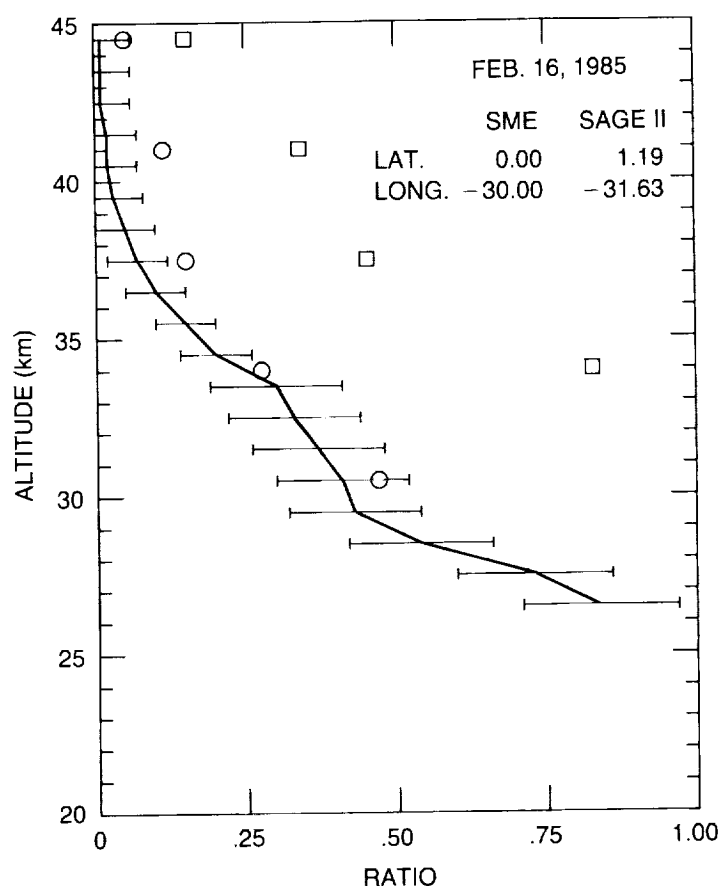


Figure 10.12 Comparison of extinction ratios (here, the ratio of aerosol extinction to molecular Rayleigh extinction, at a wavelength of 450 nm) from SAGE-II limb extinction measurements and from SME light-scattering measurements converted to extinction (volume scattering) using two distinct aerosol size distributions. The solid line with error bars shows the SAGE-II profile. Circles show SME data calculated by assuming a standard gamma distribution, with $r_g = 0.1 \mu\text{m}$ and variance $= 0.0025 \mu\text{m}^2$ (the total number of particles is $\sim 15/\text{cm}^3$, and the mass mixing ratio is 2 ppbm). Squares show SME data calculated for another standard gamma size distribution, with $r_g = 0.14 \mu\text{m}$ (number $\sim 3/\text{cm}^3$ and mass mixing ratio 1 ppbm). In the latter case, one would obtain the same result using a log-normal size distribution, with $r_g = 0.045 \mu\text{m}$, $\sigma = 2.5$, and $n = 1/\text{cm}^3$ (G. Yue and R.T. Clancy, private communication, 1988).

10.4.1 El Chichón

The El Chichón volcano is situated in Mexico at 17.3°N latitude and 93.2°W longitude. Four major eruptions took place between March 28 and April 4, 1982, when the final and largest explosion occurred. The GOES and NOAA-6 satellites observed the clouds from these eruptions, indicating that at least two had penetrated the tropopause (Bandein and Fraser, 1982). The cloud quickly spread westward over the Pacific Ocean. Lidar observations made at the Mauna Loa Observatory on April 9 showed a scattering layer at an altitude of 26 km; the scattering ratios were the greatest ever observed at Mauna Loa (DeLuisi et al., 1983). Subsequent lidar measurements (McCormick et al., 1984b) and in situ dustsonde observations (Hofmann and Rosen, 1983a) showed that the bulk of the injected material had dispersed up to 30 km, and two distinct stratospheric layers had formed with a demarcation at about 21 km marked by minimum aerosol concentrations. These layers appeared to be controlled by upper level wind systems.

AEROSOL ABUNDANCES AND DISTRIBUTIONS

The development of the eruption clouds was monitored by the Nimbus-7 Total Ozone Mapping Spectrometer—TOMS (Krueger, 1983), SME (Barth et al., 1983)—and the AVHRR sea surface temperature sensor (Strong, 1984). The stratospheric aerosols have been studied extensively, often by coordinated missions. Table 10.5 summarizes the principal observational studies. The early period just following the eruption was the most intensively investigated. However, routine measurements of the aerosol cloud, both by remote and in situ techniques, have continued to the present.

Table 10.5 Observational Methods Used To Study the Stratospheric Effects of the El Chichón Volcanic Eruption

Technique	Notes	References
<i>Ground-Based</i>		
Lidar backscatter	Numerous stations, mainly in the Northern Hemisphere.	McCormick, 1985; Jager et al., 1984; DeLuisi et al., 1983; Reiter et al., 1983; Adriani et al., 1983; Post, 1985; Uchino, 1985; Clemesha & Simonich, 1983; Shibata et al., 1984; Iwasaka et al., 1985a.
Solar and stellar photometer optical depth	Part of long-term data sets from Mauna Loa, Hawaii, and Flagstaff, Arizona.	DeLuisi et al., 1983; Lockwood et al., 1984.
Spectrophotometer		Evans and Kerr, 1983.
SO ₂ Measurements	Used to estimate total SO ₂ injection.	
<i>Airborne and Balloon</i>		
Lidar backscatter	Numerous flights by NASA-LaRC.	McCormick & Swissler, 1983; McCormick et al., 1984.
In situ sampling of aerosol size and composition	Aircraft flight altitude limits sampling to lower part of aerosol cloud.	Oberbeck et al., 1983; Knollenberg & Huffman, 1983; Gooding et al., 1983; Gandrud et al., 1983; Woods & Chuan, 1983; Mroz et al., 1983.
In situ gaseous sampling or overburden measurement	Aircraft flight altitude limits sampling to lower part of aerosol cloud.	Vedder et al., 1983; Evans & Kerr, 1983.
Balloon-based particle counter	Numerous flights to 30 km by U. of Wyoming.	Hofmann & Rosen, 1983a,b; Hofmann & Rosen, 1984, 1985.
Infrared transmission	Additional absorption features due to El Chichón effluents measured.	Whitteborn et al., 1983.

Table 10.5 (continued)

Multiwavelength Sun photometer	Measures wavelength dependence of optical depths.	Dutton & DeLuisi, 1983; Swissler et al., 1983; Spinhirne, 1983; Shah and Evans, 1985.
<i>Satellite</i> Nimbus-7 TOMS	Shorter wavelengths used to map SO ₂ cloud.	Krueger, 1983.
NOAA 7 & GOES	Mapped spreading of dust cloud.	Robock & Matson, 1983.
SME thermal emission	Mapped initial distribution of aerosol cloud.	Barth et al., 1983; Thomas et al., 1983.
AVHRR	Negative bias on sea surface temperature indicated locations of aerosol cloud.	Strong, 1984.
SAM-II	1 μm optical depth, in polar regions only.	McCormick, 1985.
SAGE-II	Since October 1984 only.	Mauldin et al., 1985a,b.

10.4.1.1 Cloud Characteristics and Behavior, April–December 1982

Global Dispersion

The early dispersal of the stratospheric eruption clouds is most clearly delineated on satellite images from NOAA-7, GOES-E, and GOES-W (Robock and Matson, 1983). The cloud spread westward from Mexico in a restricted longitudinal band, circumnavigating the globe by April 25, about 3 weeks after the major eruption. The cloud passed over Mauna Loa, where lidar backscatter ratios exceeded 300; the densest part of the cloud was at 26 km, with an upper boundary at about 35 km (DeLuisi et al., 1983). Local optical depths at a wavelength of 425 nm reached 0.7 that April, compared with normal background values of ~ 0.02 .

Meridional spreading of the cloud was recorded by lidar probes at middle and high latitudes. At Tsukuba, Japan (30°N, 140°E), a dense aerosol layer was detected at 15 km on April 25 (Uchino, 1985). At the NASA Langley Research Center (37°N, 76°W), a particle layer was seen at a similar altitude on April 29 (McCormick et al., 1984b). This low-altitude cloud (lying below about 21 km) reached European lidar stations soon afterward. It was observed over Garmisch-Partenkirchen (47°N, 11°E) on May 3, 1982 (Reiter et al., 1983), and over Frascati, Italy (42°N, 23°E), on May 13 (Adriani et al., 1983). Movement of the cloud into the Southern Hemisphere proceeded more slowly. Lidar observations at San Jose dos Campos (23°S, 40°W) showed the first major enhancement in July 1982; as in the Northern Hemisphere midlatitudes, the peak scattering intensity originated below 20 km (Clemesha and Simonich, 1983).

These lidar observations are supported by concurrent satellite measurements. Data from SME at a wavelength of 6.8 μm taken on May 21 placed the bulk of the injected aerosol between

AEROSOL ABUNDANCES AND DISTRIBUTIONS

the Equator and 30°N; a less dense layer at lower altitudes extended to about 60°N (Barth et al., 1983). Traces of volcanic aerosol had reached higher northern latitudes by this time. Close examination of SAM-II satellite profiles reveal particle layers below 20 km arriving at latitudes of 65°–80°N by May 1982.

An accurate description of the longer term meridional and vertical distribution of the El Chichón cloud was obtained using the NASA Langley Research Center airborne ruby lidar system on a flight between NASA Wallops Flight Center and the Caribbean between July 9–12, 1982. Individual vertical profiles showed a layer peak at an altitude of about 26 km with maximum scattering ratios of about 50. The main layer above 21 km remained essentially confined to the latitude band between about 27°N and 5°–10°S, although the aerosol below 20 km had spread much farther north. A second lidar expedition in October 1982, covering the latitude range 46°N to 46°S, showed aerosol distributed over this entire span. However, maximum concentrations in the upper layer were still limited to a band from about 10°S to 30°N (McCormick et al., 1984b; McCormick and Swissler, 1983). By the end of 1982, the distinction between the upper and lower layers had largely disappeared.

SAM-II data for the Antarctic region obtained in December 1982 revealed that, by this time, the aerosol had reached high southern latitudes (60°–65°S). Simultaneously, in the Arctic region, the optical depths at a wavelength of 1 μm were close to their peak values of approximately 0.1 (weekly averaged).

Gas and Aerosol Properties

Estimates of SO₂ concentrations in the El Chichón eruption plume were made using satellite data (Krueger, 1983), in situ aircraft measurements (Vedder et al., 1983), and ground-based observations (Evans and Kerr, 1983). The SO₂ cloud spread westward from Mexico with the aerosol cloud. Satellite measurements suggest that approximately 3×10^6 tons of SO₂ were injected into the stratosphere. In situ measurements in the lower part of the cloud during 1982 yielded SO₂ mixing ratios of 8 to 132 pptv. Ground-based observations of the SO₂ column content over Mauna Loa, in combination with airborne measurements of the vertical and horizontal distributions of the volcanic clouds, suggest a substantially larger SO₂ injection of up to 13.4×10^6 tons (Evans and Kerr, 1983).

Size-specific composition measurements of the aerosols in the lower part of the cloud using a quartz crystal microbalance (Woods and Chuan, 1983) revealed a complex aerosol evolution. During the first months after the eruption, the aerosol mass was dominated by solid micron-sized particles, some having the appearance and composition of halite crystals. Submicron particles composed of sulfuric acid were also present. By November and December 1982, few of the large solid particles were evident, presumably depleted by sedimentation. Gooding et al. (1983) obtained similar results for aircraft samples collected at altitudes up to 19 km between 10°S and 75°N.

Balloonborne measurements in the El Chichón clouds have shown in detail the variation of particle concentration, size distribution, and mass-mixing ratio to altitudes of about 30 km (Hofmann and Rosen, 1983a,b, 1984). The measurements confirm the formation of two major layers differentiated at an altitude of 21 km. The mean radius of the particles in both layers increased with time. In the upper layer (above about 20 km), the radius peaked at $\sim 0.3 \mu\text{m}$ about 4 months after the eruption; in the lower layer, the size increased more slowly to $\sim 0.2 \mu\text{m}$ within 1 year. Figure 10.13 shows a balloon sounding made on December 9, 1982, when the highest

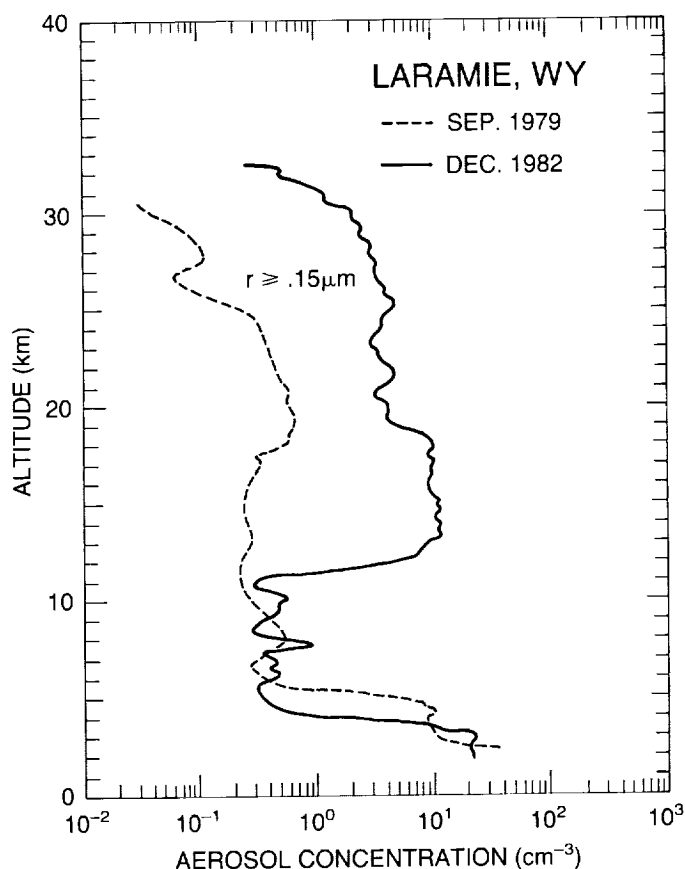


Figure 10.13 Balloonborne dustsonde measurements of the vertical concentration profile of particles with radii greater than $0.15\ \mu\text{m}$ over Laramie, Wyoming. The dashed curve represents a typical background prevolcanic aerosol layer. The large enhancement in aerosols is due to the El Chichón eruption (J. Rosen, private communication, 1987).

stratospheric aerosol concentrations were observed over Laramie. These are the greatest values seen in the last 25 years.

In the upper layer, the early-time particle size distributions also exhibited a small particle mode with radii near $0.02\ \mu\text{m}$, which is consistent with the formation of new particles by nucleation of H_2SO_4 vapor.

Mass Loading

Estimates of the aerosol mass produced by El Chichón range from roughly 7×10^6 tons by Krueger (1983), to $8\text{--}20 \times 10^6$ tons by Hofmann and Rosen (1983a,b), to 27×10^6 tons by Evans and Kerr (1983) (where measurements of SO_2 emission have been converted to an equivalent 75-percent- H_2SO_4 /25-percent- H_2O aerosol mass using a multiplicative factor of 2, although the conversion factor would vary according to the actual aerosol composition). The highest figures are probably overestimates of the El Chichón emissions. Nevertheless, the total stratospheric aerosol mass generated by El Chichón may be comparable to that of the Agung eruption of 1962. In Figure 10.2, for example, the El Chichón eruption (17.3°N , April 1982) caused a much larger transmission anomaly at Mauna Loa (19.5°N) than did the Agung eruption (8.3°S , March 1963).

AEROSOL ABUNDANCES AND DISTRIBUTIONS

The time delay to the apparent maximum in the aerosol mass loading following El Chichón varied with latitude from about 3 months at latitudes near that of the eruption to about 1 year at high northern latitudes. Viewed globally, the total aerosol mass may have peaked in about 5 to 6 months (between August and September 1982; McCormick, 1984). The latitude distribution of the mass loading, roughly 7 months after the eruption, is illustrated in Figure 10.14 (McCormick and Swissler, 1983). Globally averaged stratospheric aerosol optical depths during the period of maximum loading varied from 0.03 to 0.15 at visible wavelengths, with the highest values observed at about 20°N (Spinhirne, 1983; Shah and Evans, 1985). Minimum optical depths were also observed in the vicinity of 35°N.

10.4.1.2 Cloud Characteristics and Behavior, 1983–1986

During 1983 to 1986, the aerosol generated by the El Chichón eruption steadily decayed. The decline was interrupted only briefly in late 1985 by the eruption of Ruiz in Colombia. The El Chichón particulate spread relatively uniformly over the globe during this period. Balloonborne particle detectors flown over Antarctica in October 1983 showed a substantial aerosol layer within the south polar vortex at 78°S (Hofmann and Rosen, 1985). Figure 10.15 indicates the complex structure in the geographical distribution of the residual aerosols of El Chichón; such variability has been detected in other volcanic clouds as well (Kent and McCormick, 1984).

M.P. McCormick and T. Swissler (private communication, 1987) employed lidar and satellite extinction data to estimate the decay rate of the El Chichón aerosol mass. The decay rates were

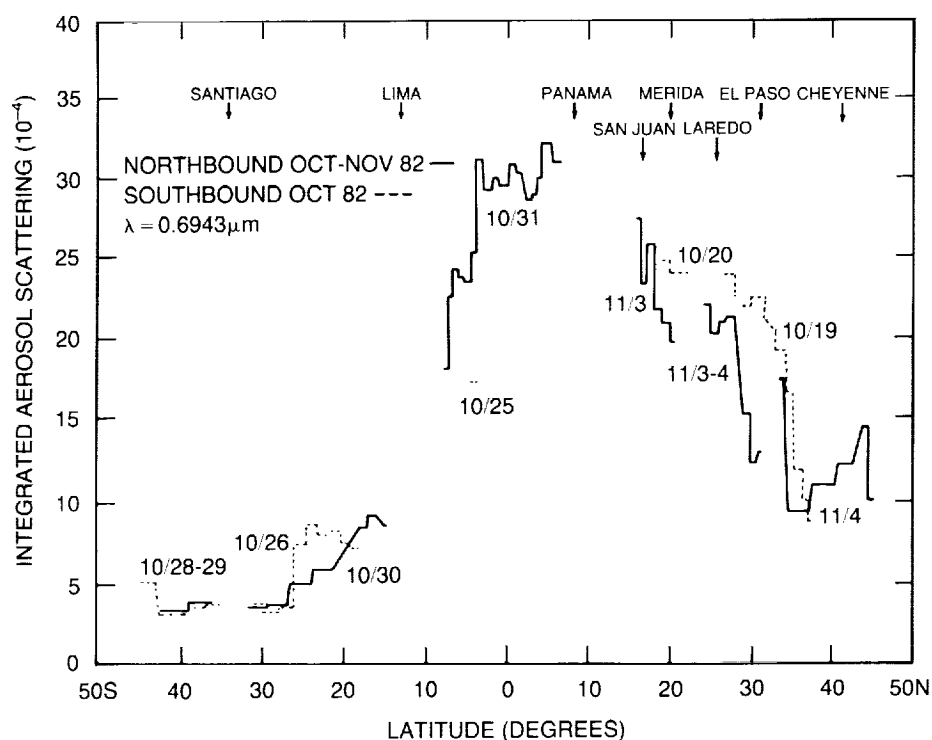


Figure 10.14 Integrated lidar aerosol backscatter intensity (in units of 10^{-4} sr^{-1}) for the stratosphere (i.e., from the tropopause upward) versus latitude from an aircraft survey (McCormick and Swissler, 1983). The integrated backscatter can be related to the aerosol mass if the size distribution and composition of the particles are known (see Section 10.2).

found to depend on latitude and the period of observation. The average e-folding time in the Northern Hemisphere for periods extending over a year or more was roughly 10 to 11 months. Similar stratospheric decay lifetimes were deduced for other volcanic events.

While the El Chichón aerosol mass decayed, the mean particle radius in the upper cloud layer decreased (Hofmann and Rosen, 1984), and the altitude of the layer dropped from about 26 km in August 1982 to about 21 km in August 1983 (McCormick, 1984). Lidar backscatter measurements at $10.6\mu\text{m}$ —a wavelength sensitive to the larger particles in the cloud—and at 40°N showed similar decreases in the peak scattering intensity and layer height (Post, 1985). Post estimated that the time constant for the aerosol backscatter decay was about 7 months. A research flight to the Arctic in March 1983 yielded evidence of downward transport of the volcanic aerosol in a tropopause fold on the flank of the polar vortex (Shapiro et al., 1984). A similar stratosphere–troposphere exchange of volcanic particles was observed following the eruption of Mount St. Helens in 1980 (Kent et al., 1985a).

10.4.2 Mount St. Helens and Other Volcanic Eruptions

In addition to the eruption of El Chichón, which produced an order-of-magnitude increase in the stratospheric aerosol loading, several other recent smaller eruptions led to measurable stratospheric perturbations. Table 10.6 lists three of the most massive historical eruptions as well as the more recent events that have affected the stratosphere. There is no reason to believe that the frequency of occurrence of such perturbing eruptions recorded in Table 10.6 is unique to the last decade of intensive monitoring. Accordingly, relatively frequent volcanic disturbances at irregular intervals must be anticipated for the future. On the other hand, eruptions of the magnitude of El Chichón (in atmospheric effects) would be expected only once every few decades statistically (Self et al., 1981; Simkin et al., 1981). Although it is difficult to estimate accurately the frequency of volcanic eruptions as a function of eruption size (measured by the mass of the aerosol injection at high altitudes), it appears that stratospheric injections of $\sim 10^5$ tons or more can occur, on average, about once every year.

The background stratospheric aerosol mass loading reached its lowest recorded global level, about 0.5×10^6 tons, in 1979. The eruption of El Chichón increased the total loading above background by a factor of about 20. As a result, during the period from April 1982 through 1984, eruptions even the size of Mount St. Helens would have been difficult to detect, except in the first few days when the clouds would be localized and very dense.

Following the volcanic injection of gases and ash, the globally integrated optical extinction typically rises to a maximum in roughly 3 months (Turco et al., 1982). This is followed by a decay in the aerosol optical effects with a time constant of about 6 to 12 months. The early rise in the perceived average particle extinction is caused by the spreading of the dense emission cloud and the conversion of sulfur gases to sulfuric acid aerosols. The larger ash particles generally fall out during this period. The decay in extinction following the maximum is associated with the global dispersal and thinning of the clouds and with the removal of sulfuric acid aerosols from the stratosphere. The variation in recovery time from eruption to eruption does not appear to be large. Figure 10.16 shows the changes in mean global aerosol optical depths between February 1979 and November 1981. Over this period, five eruptions caused significant stratospheric effects. The data illustrate the rise to a maximum optical depth (extinction) about 3 months after each eruption, followed by a slower decay. Because there have not been any recent large volcanic events, it is not possible to say if this regular temporal pattern of growth and decay would also occur in such cases.

AEROSOL ABUNDANCES AND DISTRIBUTIONS

Table 10.6 Volcanic Eruptions Known To Have Injected Material Into the Stratosphere

(a) Massive Eruptions Prior to 1974

Date	Volcano	Location	Total Global Injection* (10 ⁶ metric tons)	Source
August 1883	Krakatoa	6.1°S, 105.4°E	50	Deirmendjian (1973)
June 1912	Katmai	58.3°N, 155.0°W	20	Deirmendjian (1973)
March 1963	Agung	8.3°S, 115.5°E	16	Deirmendjian (1973)
			30	Cadle et al. (1976, 1977)

(b) Eruptions Since 1974

Date	Volcano	Location	Total Global Injection* (10 ⁶ metric tons)	Source
October 1974	Fuego	14.5°N, 90.9°W	6	Cadle et al. (1976, 1977)
			3	Lazrus et al. (1979)
January 1976	Augustine	59.4°N, 153°W	0.6	Cadle et al. (1977)
February 1979	Soufriere	13.3°N, 61.2°W	0.002	McCormick et al. (1981)
November 1979	Sierra Negra	0.8°S, 91.2°W	0.16	Kent & McCormick (1984)
May 1980	St. Helens	46.2°N, 122.2°W	0.55	Kent & McCormick (1984)
October 1984	Ulawun	5.0°S, 151.3°E	0.18	Kent & McCormick (1984)
April 1981	Alaid	50.8°N, 155.5°E	0.50	Kent & McCormick (1984)
May 1981	Pagan	18.1°N, 145.8°E	0.85	Mroz et al. (1983)
January 1982	Mystery Volcano			
April 1982	El Chichón	17.3°N, 93.2°W	12.0	McCormick (1984)
November 1985	Ruiz	4.9°N, 75.4°W		

*Mass of stratospheric aerosol

The dispersal of volcanic debris clouds is initially zonal in character (e.g., Robock and Matson, 1983). The rate and detailed nature of the dispersion depend on the latitude and season of the eruption and on the heights of debris injection. Wind shears tend to distort the clouds, creating large geographical inhomogeneities, and local fluctuations in the zenithal extinction. Over the course of several weeks or months, the clouds become more uniform in their zonal distribution. Meridional mixing also occurs with the following general behavior (Kent, 1986):

- The majority of the material injected by high-latitude eruptions remains within the same hemisphere.
- The material injected by low-latitude eruptions disperses into both hemispheres, with the transport rate being seasonally modulated and most rapid into the winter hemisphere.
- The volcanic debris tends to collect into three latitude bands—20°S to 20°N, >40°N, and >40°S.

For example, the aerosol injected by Mount St. Helens (46°N) remained almost entirely within the Northern Hemisphere (see Figure 10.8), while that from Sierra Negra (1°S) dispersed over several months into both hemispheres. Material injected by El Chichón (17°N) at somewhat higher latitudes than Sierra Negra remained largely in the Northern Hemisphere, although an appreciable fraction drifted into the equatorial regions and thence into the Southern Hemisphere (see Figure 10.15).

As the aerosols move poleward from the latitude of injection, the altitude of the cloud decreases. This is the same tendency seen in the meridional distributions of trace gases, and reflects the downward slope of isentropic surfaces toward the poles. The removal of the aerosols from the stratosphere probably occurs at midlatitudes as well as in the winter polar vortex. However, the details of the removal mechanisms are not well characterized. The initial height of injection, particle sedimentation, stratosphere-troposphere exchange, and polar subsidence all may have roles in purging the stratosphere of volcanic debris (Post, 1985; Kent et al., 1985a,b).

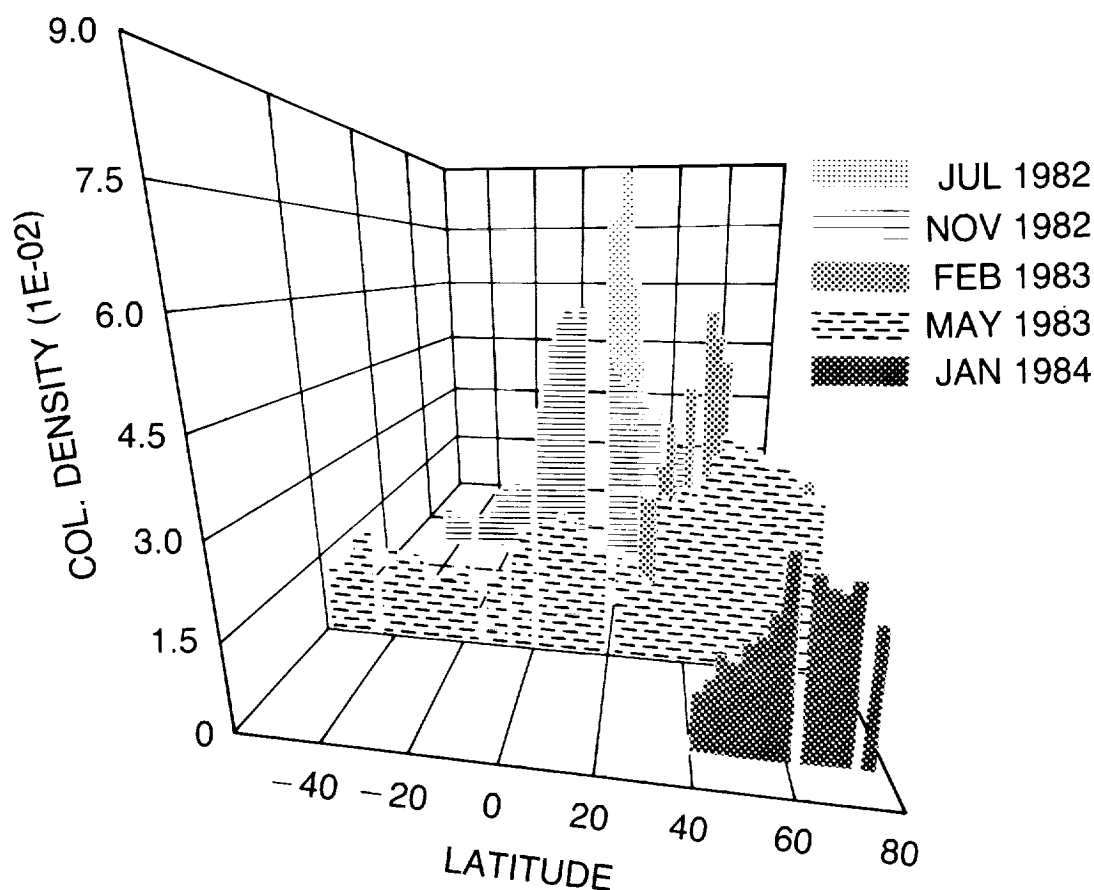


Figure 10.15 Perspective plot of the integrated stratospheric lidar backscatter intensity versus latitude for different times after the El Chichón eruption. The backscatter data have been converted to a vertically integrated aerosol column mass density (g/m^2) using an appropriate aerosol size distribution/composition model (McCormick et al., 1984). The data were collected by aircraft survey at the times indicated in the legend.

AEROSOL ABUNDANCES AND DISTRIBUTIONS

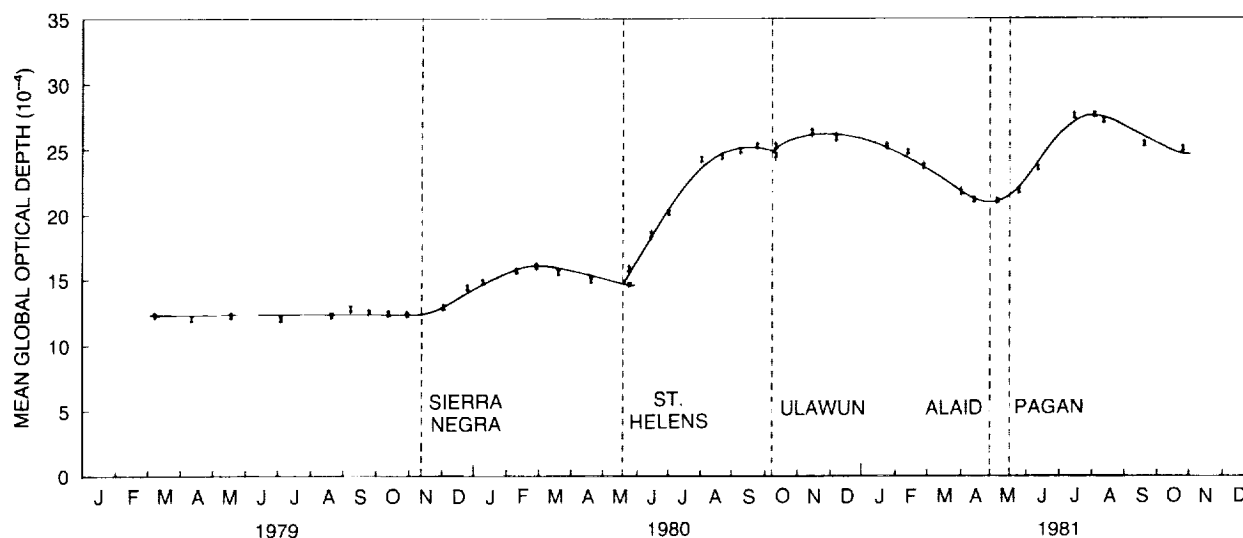


Figure 10.16 Time development of the global-average stratospheric aerosol optical depth, referred to the zenith, at a wavelength of $1 \mu\text{m}$. Data were obtained from the SAGE and SAM-II satellite systems. The points correspond to derived observational values, while the solid curve is an empirical fit to the data (G.S. Kent, private communication, 1987).

10.5 AEROSOL IMPACT ON OZONE OBSERVATIONS

Passive remote-sensing techniques not specifically concerned with the detection of aerosol properties generally assume an atmosphere containing molecular Rayleigh scatterers and gaseous absorbers or emitters. Limited attention has been given to the possible effects of aerosols on remote ozone observations. In the near and thermal infrared wavelength regions, including the $8\mu\text{m}$ to $12\mu\text{m}$ window, molecular scattering is negligible. Typically, aerosols will have an effect only if a substantial concentration of micrometer-size particles is present. Nevertheless, tropospheric aerosols can produce substantial radiance signals in systems that use near-infrared bands to measure surface properties, and in certain wavelength channels of atmosphere-observing systems such as the AVHRR.

Much of the attention focused on the remote-sensing impacts of aerosols has emphasized the errors generated in ozone measurements at visible and near-ultraviolet wavelengths. In this section, aerosol interference in the ground-based Umkehr and space-based Solar Backscatter Ultraviolet (SBUV) methods of determining the vertical ozone profile are described, and problems encountered in correcting for the aerosol interference are discussed. The Umkehr and SBUV errors exhibit different sensitivity to the vertical ozone distribution and the optical properties of the particles. Hence, different approaches to analysis must be taken in each case.

10.5.1 Umkehr

10.5.1.1 Description of the Aerosol Error

The standard C-wavelength-pair (311.4 nm and 332.4 nm) Umkehr device measures the ratio of the cloud-free zenith sky intensities (skylight) at these wavelengths as the solar elevation angle changes from 0° to 30° (solar zenith angle changes from 90° to 60°) during sunrise or sunset. Measurements normally are taken at 12 to 14 solar elevations, although only 12 observations are

used to determine the ozone profile. The Umkehr algorithm for deriving the ozone profile is based upon a mathematical model of radiative transfer in a molecular scattering and absorbing atmosphere (Bojkov, 1969a). Particle effects are neglected in the standard algorithm for several reasons: the perturbations caused by the presence of background stratospheric aerosols are estimated to be quite small; accurate quantitative information on the distribution and properties of aerosols over Umkehr sites is not generally available; and inversion algorithms including aerosols are considerably more complex.

The Umkehr method yields ozone profile information at large solar zenith angles—essentially approaching twilight conditions. Hence, the direct rays of the Sun (particularly at the longer of the two Umkehr wavelengths) must traverse a long optical path through the stratospheric aerosols before being scattered vertically downward to the instrument (see Figure 10.17). The solar rays that produce the zenithal scattered light at the shorter of the wavelength pair have passed through air layers at higher altitudes, where the ozone absorption is small enough to allow penetration of the solar beam. Accordingly, the short wavelength radiation should be much less affected by aerosols than the long wavelength radiation, because the aerosol concentrations are smaller at higher altitudes; nevertheless, the zenithal scattered light is modified in traversing the underlying aerosol (and ozone) layer (Figure 10.17). The difference in the effect

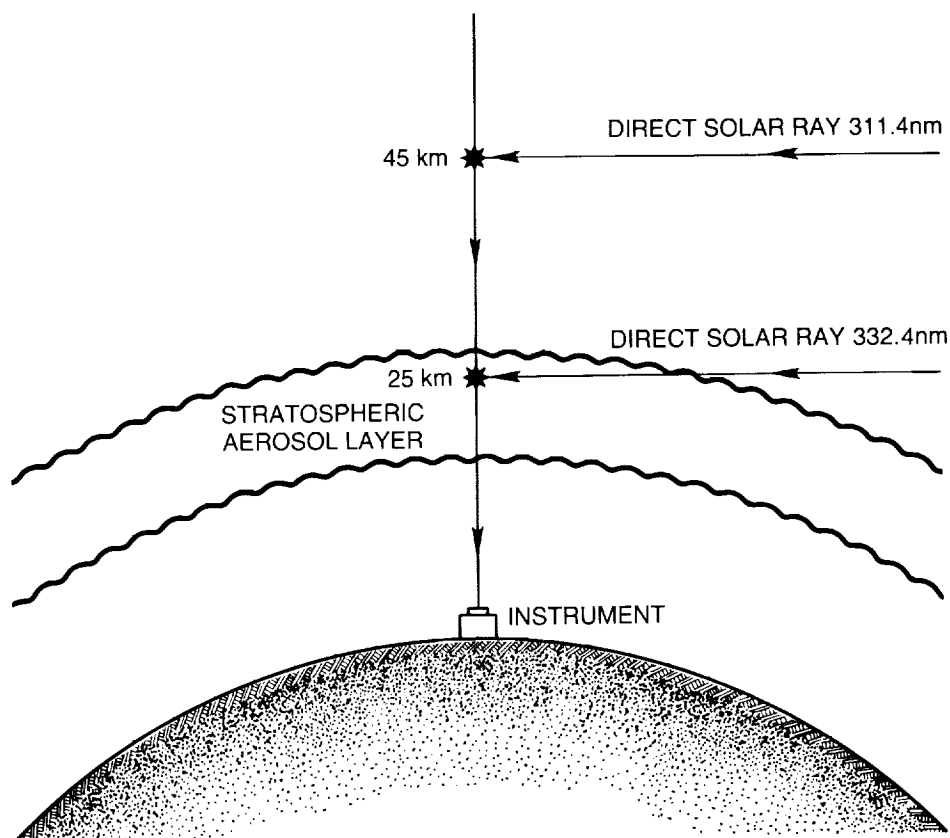


Figure 10.17 Illustration of the geometry for zenith Umkehr observations of scattered solar radiation, with the Sun at an elevation of 0° . In the near-ultraviolet spectrum, different wavelengths of light penetrate to different depths in the atmosphere and are scattered by air molecules with different efficiencies (see Figure 10.18). The optimum tangent rays corresponding to the Umkehr C-pair of wavelengths are shown. The 332.4 nm ray is scattered mainly in the region of the stratospheric aerosol layer.

AEROSOL ABUNDANCES AND DISTRIBUTIONS

of aerosol extinction between the long and short wavelengths leads to an ozone error in the Umkehr inversion, because the aerosol signal is misinterpreted as a *deficit* of ozone above the ozone maximum and as an *excess* of ozone below the maximum. The aerosol extinction optical depth is, therefore, of first-order importance in this error-generating process.

The location of the aerosol layer in relation to the ozone maximum is also important (DeLuise, 1969). The altitude distribution of aerosols affects the severity of the error because it modulates the differential impact of aerosols between the two independent scattering regions (Figure 10.18). The scattered radiation at the longer wavelength, for example, originates at about 20 km to 25 km near twilight, while the radiation at the shorter wavelength originates much higher. As

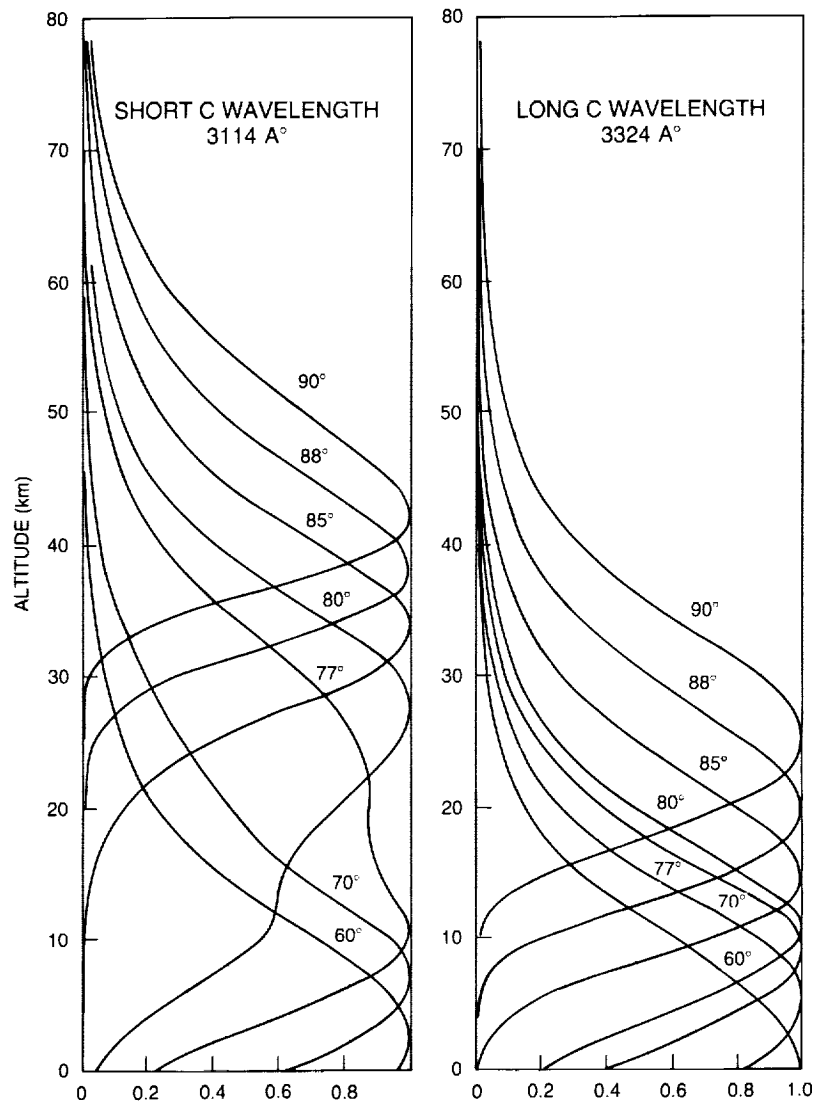


Figure 10.18 Normalized contribution functions (i.e., the relative vertical intensity profiles for primary scattered radiation, which are related to the weighting functions of Chapter 3) for the Umkehr C (311.4 and 332.4 nm) wavelength pair at several solar zenith angles. The profiles illustrate the strong overlap between the region of long wavelength scattering and the stratospheric aerosol layer. The contribution functions move downward as the solar zenith angle decreases from 90° (Mateer, 1964).

a result, a small aerosol-induced Umkehr "N-value" (see Section 3.3.4) is superimposed on the normal Umkehr N-value for a pure molecular atmosphere (or at least a relatively particle-free stratosphere). The normal N-value ranges from about 50 at a solar zenith angle of $\sim 60^\circ$, to a peak value of about 130 at a solar zenith angle of $\sim 85^\circ$. The magnitude of the anomalous aerosol contribution is illustrated in Figure 10.19 as a function of the solar zenith angle for the aerosol profiles given in Figure 10.20.

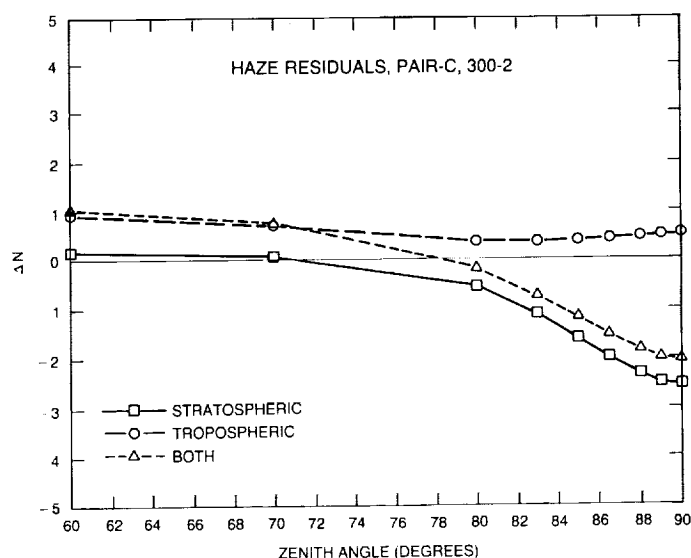


Figure 10.19 Residual, or aerosol-induced, ΔN -values in the Umkehr C-pair measurement versus solar zenith angle for three aerosol fields: tropospheric aerosols only, optical depth = 0.188, Haze L aerosol model; stratospheric aerosol only, optical depth = 0.0147, Haze H; both tropospheric and stratospheric aerosols (Haze L and H are standard aerosol size distribution models; the particle index of refraction is 1.5 - 0.03i). The vertical aerosol distributions are presented as profiles 1 and 3 in Figure 10.20. Effects of multiple scattering are included (J. DeLuise, private communication, 1987).

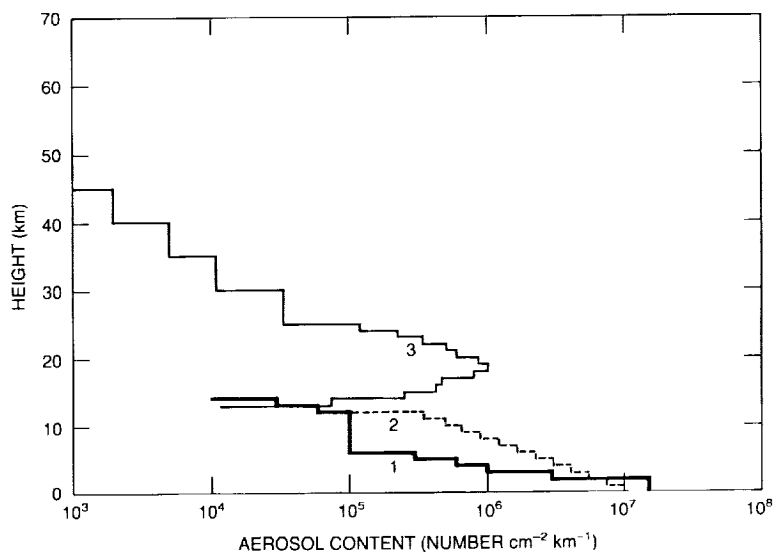


Figure 10.20 Model profiles for aerosol concentration that have been used in ozone/aerosol Umkehr error calculations. Profiles 1 and 2 correspond to the background tropospheric aerosols; profile 3 corresponds to a moderately (volcanically) perturbed stratospheric aerosol (Dave et al., 1979).

AEROSOL ABUNDANCES AND DISTRIBUTIONS

The aerosol “residual” contribution varies with solar elevation because the two scattering levels (Figure 10.18) move in relation to the ozone and aerosol layers in different ways as the solar zenith angle varies. Conversely, for a fixed solar zenith angle, the aerosol Umkehr term varies according to the relative position of the aerosol profile with respect to the ozone profile. Since the vertical distributions of stratospheric aerosols are somewhat constrained by physical processes, the impact of uncertainty in the aerosol profile on Umkehr ozone measurement accuracy is expected to be of second order.

Variable particle scattering and absorption properties (particularly the phase function) produce a small perturbation in the scattered radiance field (see Section 10.2). Again, the optical properties of the stratospheric aerosols are sufficiently constrained that uncertainty in the phase function should not seriously degrade the Umkehr data analysis. The stratospheric aerosols are, moreover, not usually highly absorbing, and single-scatter albedos ~ 1 can be assumed with little error.

Table 10.7 summarizes the sensitivity of the Umkehr technique to variations in several aerosol properties, as discussed above. Umkehr ozone retrievals are most sensitive to the total aerosol optical depth (or equivalently, the integrated extinction).

Table 10.7 Aerosol Impact on Umkehr and SBUV Measurement Systems, in Order of Importance of Aerosol Properties to Each System

Umkehr	SBUV
1. Optical depth	1. Profile and phase function
2. Profile	2. Optical depth
3. Phase function and refractive index	3. Refractive index

Note: The specification of both the aerosol profile and optical depth as parameters may appear to be redundant. However, a specific observational system may derive one parameter independently of the other at a particular wavelength. For example, a sunphotometer measurement from the surface may provide only optical depth information. (J. DeLuisi, private communication, 1987).

10.5.1.2 Calculation of Umkehr/Aerosol Errors

If the aerosol size distribution, refractive indices at the relevant wavelengths, and vertical distribution are known, the resulting error in the Umkehr measurement can be calculated theoretically (e.g., Dave et al., 1979). An intensive study of the Umkehr errors introduced by the El Chichón eruption is being conducted by J. DeLuisi and coworkers (private communication, 1987). Results from these error calculations are consistent with empirically deduced errors, such as those reported by Reinsel et al. (1984) (additional analyses of Umkehr and lidar observations at Mauna Loa during the El Chichón period provide further support for these error correction schemes; DeLuisi, 1979, and private communication, 1987).

Figure 10.21 shows the potential errors in ozone measurements at each Umkehr level due to stratospheric aerosols. The error is defined as the difference between the Umkehr ozone inversion values with and without stratospheric aerosols present, for a total aerosol optical depth of 0.01. The errors for other aerosol optical depths would be estimated by simple linear scaling of the errors in Figure 10.21, which correspond to an aerosol optical depth of 0.01. The actual error would be somewhat different, depending on the specific vertical distributions of ozone and aerosols, the true optical properties of the aerosols, and geometric factors.

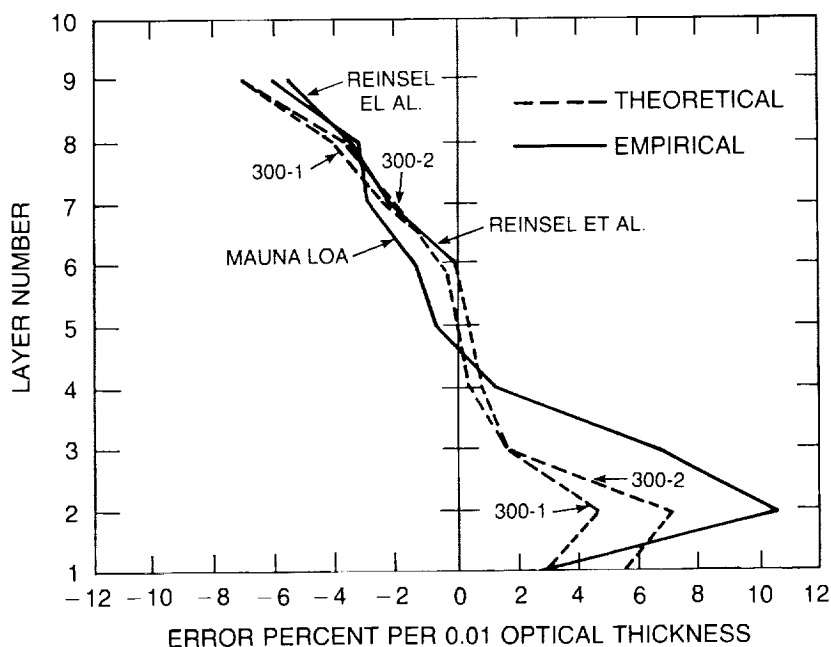


Figure 10.21 Errors in Umkehr ozone measurements resulting from stratospheric aerosol interference. The errors are given at each Umkehr level assuming a total aerosol optical depth of 0.01; that is, the ozone errors are normalized to a stratospheric optical thickness of 0.01. The theoretical errors were calculated by Dave et al. (1979) as described in the text, for two initial ozone profiles (300-1 and 300-2). The empirical errors were derived from combined Umkehr and lidar measurements at Mauna Loa from 1983 to 1986 (J. DeLuise, unpublished data) and elsewhere (Reinsel et al., 1984; J. DeLuise, private communication, 1987).

In Figure 10.21, the errors were determined by two independent procedures, with fairly consistent results. The “empirical” error estimate was derived from direct simultaneous measurements of ozone and aerosols. In one case, the Mauna Loa lidar and Umkehr data records for 1983 to 1986 were used to study the statistical correlations between changes in the stratospheric optical depth as sensed by lidar, and the (apparent) changes in ozone as deduced by Umkehr. The resulting correlation at each Umkehr level could then be expressed as a statistical error in the apparent ozone concentration at that level for a standard optical depth of 0.01, assuming that the errors at other aerosol optical depths could be estimated using a linear relationship between optical depth and error over the range of interest.

The “theoretical” errors in Figure 10.21 were calculated in accordance with a procedure described by Dave et al. (1979). In this case, a radiative transfer code was used with an observed ozone profile and a measurement-based aerosol model to calculate explicitly the aerosol interference (or apparent ozone error). Two examples of such a computation are shown in Figure 10.21. The aerosols are characterized by their total optical depth, vertical distribution, and physical parameters (i.e., size distribution and index of refraction, assuming homogeneous composition and spherical shape). Figure 10.22 illustrates a midlatitude stratospheric aerosol optical depth model constructed from lidar data and applied to analyze northern midlatitude Umkehr station observations during the El Chichón epoch (J. DeLuise and D. Longenecker, private communication, 1987). The aerosol vertical profile and physical properties are based on in situ measurements (e.g., Dave et al., 1979). Typically, climatological ozonesonde data are used to initialize the ozone profile for estimating the Umkehr errors; iterative schemes using derived ozone profiles to improve the error estimate are also available.

AEROSOL ABUNDANCES AND DISTRIBUTIONS

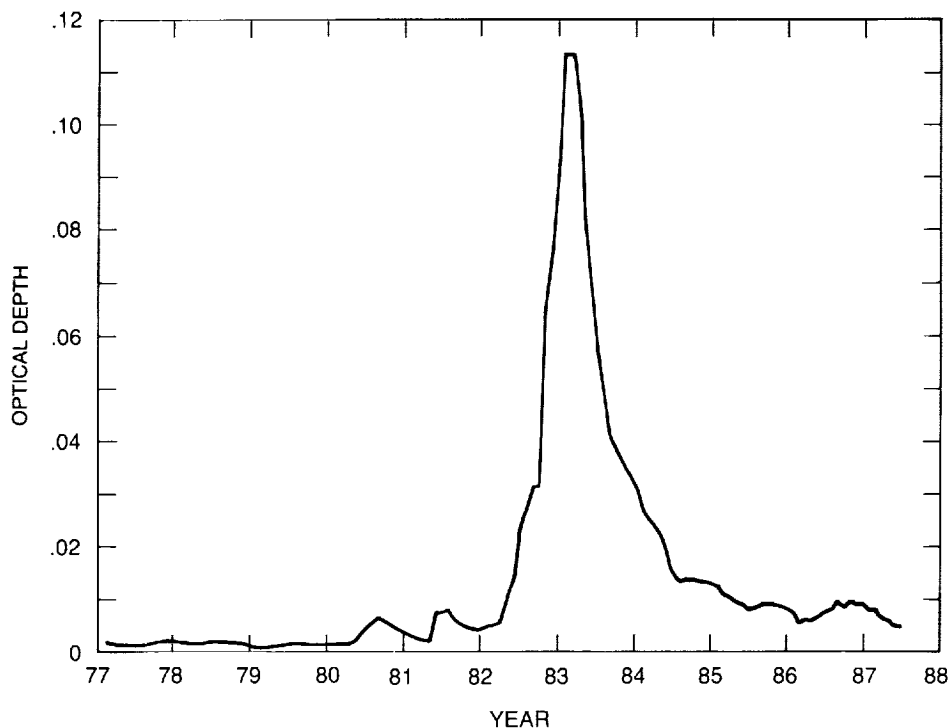


Figure 10.22 Monthly averaged midlatitude stratospheric aerosol optical depth (above 15 km) versus time, as compiled from lidar measurements at four sites in the United States, Wales, Germany, and France (J. DeLuisi and D. Longenecker, private communication, 1987).

The data in Figure 10.21 indicate that aerosols can have a major impact on Umkehr observations. In the lower Umkehr layers (1 to 3), the error in apparent ozone concentrations for a particle optical thickness of 0.01 can range up to 10 percent, and is at least a few percent. During volcanically disturbed periods, stratospheric aerosol optical depths of ~ 0.1 to 0.2 may exist for a year or more, leading to potential Umkehr errors of tens of percent. These errors can be corrected by the procedures discussed above (DeLuisi, 1979; Dave et al., 1979; Reinsel et al., 1984; J. DeLuisi, private communication, 1987).

Nevertheless, the residual error associated with uncertainties in the properties of the aerosols that are affecting the Umkehr system is not well defined. Lidar backscatter measurements are rarely made concurrently with Umkehr observations. Moreover, although lidar data provide information on the vertical distribution of particles, independent measurements are needed to define the other aerosol properties that are relevant to the Umkehr system. The use of average aerosol models or climatological data in correcting the Umkehr measurements leaves open the possibility of significant residual errors during volcanically perturbed times, particularly when observations from dispersed Umkehr sites are treated as a uniform data set.

J. DeLuisi (private communication, 1987) has made a preliminary detailed analysis of Umkehr errors and corrections following the El Chichón eruption. He concludes that the aerosol-induced Umkehr error can be reduced to a magnitude that is less than the standard Umkehr error (see Chapter 3), if adequate accurate aerosol data are available for the correction process. Considering past Umkehr observations, the quality and quantity of the aerosol data available for accurate correction are questionable. Accordingly, historical Umkehr data collected during volcanic

epochs, even after correction, should be treated cautiously in ozone trend analysis. Based on the error estimates in Figure 10.21, aerosol problems would seem to be most manageable in the middle Umkehr levels (4 to 7), but potentially serious in the lowest and highest levels.

The aerosol error could be minimized in future Umkehr measurements through careful monitoring of the stratospheric aerosols over key Umkehr sites by local lidar and remote satellite observations (also see Section 10.5.3 below).

10.5.2 Solar Backscatter Ultraviolet (SBUV)

10.5.2.1 Description of the Aerosol Error

The SBUV measures solar ultraviolet radiation that is scattered back to space by the atmosphere; the geometry is illustrated in Figure 10.23. Atmospheric layers that contain aerosols can affect the scattered radiance detected at the satellite, thus affecting the ozone retrieval process. In general, the resulting ozone concentrations are underestimated in the region of the aerosol

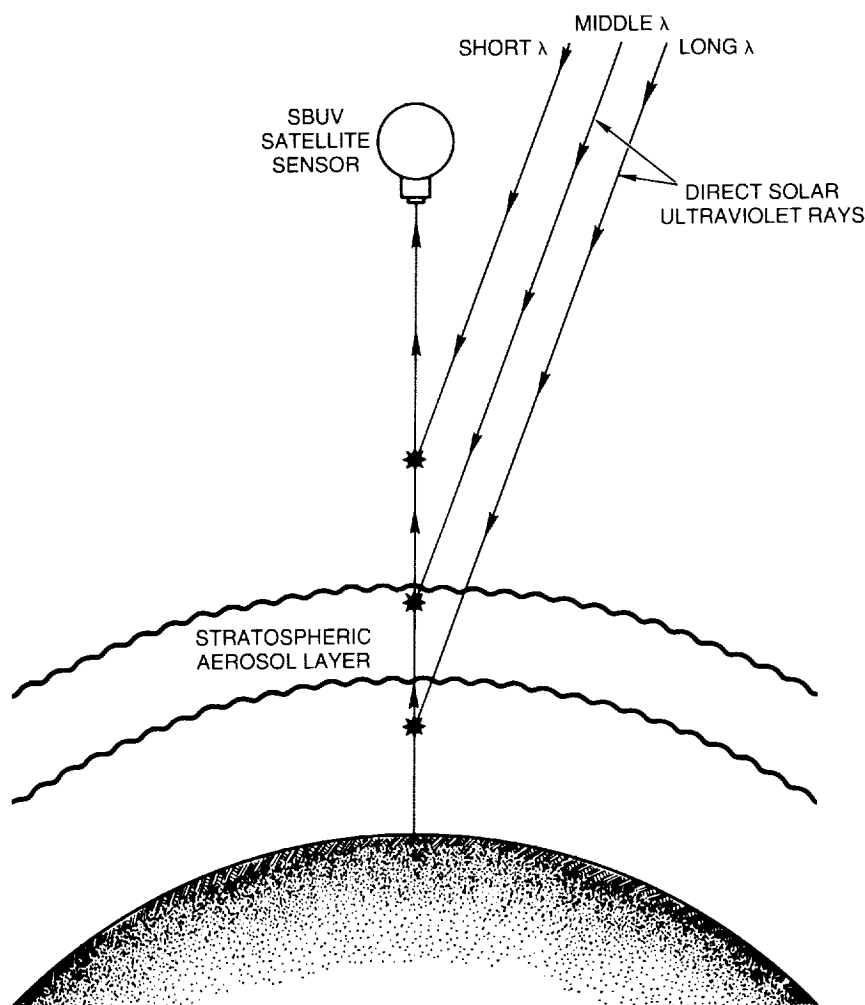


Figure 10.23 Illustration of the geometry for SBUV nadir observations of scattered solar radiation. The longer wavelength radiation reaching the sensor may be scattered from, or traverse, the region occupied by stratospheric aerosols.

AEROSOL ABUNDANCES AND DISTRIBUTIONS

layers. In contrast to Umkehr, the aerosol light-scattering phase function is an important factor in the SBUV error signal, because the SBUV normally operates over a much wider range of scattering angles. The aerosol optical depth is also important. For retrieval heights above the stratospheric aerosol layer, the SBUV-derived ozone profile is not affected by aerosol scattering. By contrast, in the Umkehr technique, all ultraviolet radiation reaching the instrument must pass through the ozone and aerosol layers, affecting the retrieval at all heights.

Current theoretical calculations of aerosol effects on SBUV ozone measurements are concerned primarily with perturbations connected with the El Chichón eruption (R.D. Hudson, private communication, 1987). While the ozone error may be especially sensitive to volcanic aerosols residing above 30 km, the SBUV system overall is much less sensitive to aerosol interference than Umkehr. Moreover, independent measurements of aerosols in the region above 30 km by the SAGE and SME satellite sensors are not completely consistent and remain uncertain (see Section 10.3.3). Accordingly, only a limited research effort has been directed toward defining the magnitude of the aerosol-induced error in SBUV ozone data. A qualitative assessment of the sensitivity of SBUV ozone measurements to aerosol interference is summarized in Table 10.7.

10.5.2.2 Implications of SME Data for SBUV Ozone Trends

Analysis of SME solar-scattering observations (Section 10.3.3.2) suggests that considerable particulate matter may have existed between 30 km and 40 km following the eruption of El Chichón. The effect of such aerosols on the SBUV ozone retrievals during this period is not clear. A substantial uncertainty in the properties of the aerosols above 30 km seems to preclude a definitive assessment at this time. Nevertheless, a preliminary analysis carried out for this report indicates that aerosol-scattering effects probably cannot explain any significant part of the long-term drift in the SBUV ozone observations at altitudes above about 30 km (R.T. Clancy, private communication, 1987).

10.5.3 Aerosol Data Requirements for Ozone Observing Systems

Measurements of the stratospheric ozone profile, and thus ozone concentrations at specific altitudes as well as trends in those concentrations, are routinely made by the Umkehr, SBUV, and SAGE systems. Both the Umkehr and SBUV observational systems are susceptible to error when stratospheric aerosols are enhanced by major volcanic eruptions. Umkehr is more sensitive than SBUV in the high-altitude region from 30 km to 50 km.

Continuous Umkehr and SBUV data records are available since 1958 and 1978, respectively. Interpretations of these data indicate significant trends in ozone concentrations near 40 km (see Chapter 6). Over the same periods of observation, however, volcanic eruptions have injected substantial quantities of particles into the stratosphere on several occasions. Umkehr measurements can be corrected for such aerosol enhancements through the procedures outlined in Section 10.5.1. In a few cases, extensive Umkehr corrections have been calculated and published (Section 10.5.1.2). On the other hand, SBUV observations have not been systematically adjusted for aerosol effects. If the accuracy of archived ozone observations is to be improved, and if maximum information is to be gained from future observations, then appropriate correction algorithms must be designed and the necessary aerosol data base developed.

Stratospheric aerosol data that are most relevant for correcting Umkehr and SBUV observations are not routinely monitored. Although aerosol measurements are frequently made by

lidars as well as aircraft, balloon, and satellite sensors, the quantity and quality of the optical data obtained are insufficient. Moreover, some fundamental information on aerosol composition and scattering properties is very limited. For example, aerosol-scattering intensities over a wide range of scattering angles are needed for SBUV analysis (Table 10.7), but such data are rarely collected. The scattering phase function could be calculated using Mie theory if adequate particle size distribution and composition data were available. Typically, such aerosol data, even when available, are not highly accurate for particles in the most optically active size range.

Most observations of stratospheric aerosols are carried out at visible and near-infrared wavelengths. Yet, for application to ozone-observing systems, it is necessary to obtain aerosol properties at wavelengths in the near-ultraviolet spectrum. Further uncertainties can, therefore, be introduced when aerosol properties are extrapolated to shorter wavelengths.

A complete set of aerosol measurements that could be used in the ozone correction algorithms described earlier (and likely in algorithms yet to be designed for this purpose) to improve the accuracy of Umkehr and SBUV ozone profiles includes:

- The vertical profile of aerosols at several latitudes covering the observational zone—these data could be collected on a continuous basis by lidar and satellite instruments.
- The spectral extinction of the aerosols across the visible spectrum—these data might be obtained by continuous solar photometry or satellite limb extinction measurements.
- The size distribution of the aerosols and its variation with altitude—these data could be taken by occasional in situ sampling or remote-sensing techniques from the ground or space.
- The mass, composition, and morphology of the aerosols—these data might be obtained periodically by in situ analysis from balloon or aircraft platforms.

The time series, global coverage, and vertical resolution for such a data acquisition program would depend on planned uses of the data, the accuracy desired in the ozone/aerosol correction scheme, and the availability of resources. A minimum data collection plan for the Umkehr network would include lidar aerosol sounders at key Umkehr sites.

10.6 POLAR STRATOSPHERIC CLOUDS AND THE OZONE HOLE

Accumulating evidence now suggests that the polar stratospheric clouds that appear over Antarctica in the winter season may play an important role in the formation of the recently discovered “ozone hole” (see Chapter 11). This idea is strengthened by the correlation in time and space between PSC’s and the ozone hole. New physical and kinetic chemical data, as well as direct measurements within the ozone hole (Chapter 11), allow a consistent physical theory for ozone hole formation to be structured around the properties of PSC’s. Accordingly, it is essential to define as completely as possible the distribution, morphology, and physical chemistry of PSC’s. In this section, the characteristics of polar stratospheric clouds deduced from SAM-II satellite measurements and other observations are outlined in some detail. The microphysical processes by which PSC’s may form and evolve are described in view of the present, limited, knowledge. The optical and chemical properties of polar stratospheric clouds that may affect polar ozone concentrations are also discussed.

AEROSOL ABUNDANCES AND DISTRIBUTIONS

10.6.1 Observations and Morphology of PSC's

10.6.1.1 The SAM-II Satellite System

The SAM-II satellite sensor is a single-channel Sun photometer designed to measure solar intensity at a wavelength of $1.0\ \mu\text{m}$ with a 20 nm bandpass.

The instrument is mounted on the Nimbus-7 satellite and is activated each time the satellite enters into or emerges from the shadow of Earth. Because Nimbus-7 is in a Sun-synchronous orbit, the measurement opportunities for SAM-II occur at high latitudes (64° to 84° , depending on the season). During each measurement, the instrument scans the solar disc, recording the intensity as a function of time. A complete discussion of the sensor operation is given by McCormick et al. (1979) (also see Section 10.3.3.1).

The data obtained in each measurement event are used to construct atmospheric limb transmission profiles; the shape of the refracted solar disc and the ephemeris are employed to evaluate the altitudes of the ray paths. The limb transmission profiles are then inverted using the techniques described by Chu and McCormick (1979) to yield a vertical profile of the average $1\text{-}\mu\text{m}$ extinction in each atmospheric layer. An extinction profile is obtained for each sunrise and sunset event with 1-km resolution.

The SAM-II sunset measurements are made at latitudes between about 64° and 84° in the Northern Hemisphere, and the sunrise measurements at latitudes between 64° and 81° in the Southern Hemisphere. The orbital period is 104 minutes, so there can be 14 sunrise and sunset events each day separated by 26° in longitude and by about 0.01° to 0.02° in latitude. Thus, the latitude of the measurement changes very slowly with time (by about 1° per week), varying from the lowest latitude at the solstice to the highest latitude at the equinox.

The SAM-II system originally was intended to determine the climatology of the high-latitude aerosol. A routine analysis of the SAM-II measurements made in the Northern Hemisphere in January 1979 revealed 11 extinction profiles with unusually large aerosol optical depths. One of these profiles is illustrated in Figure 10.24, and should be compared with a "normal" extinction

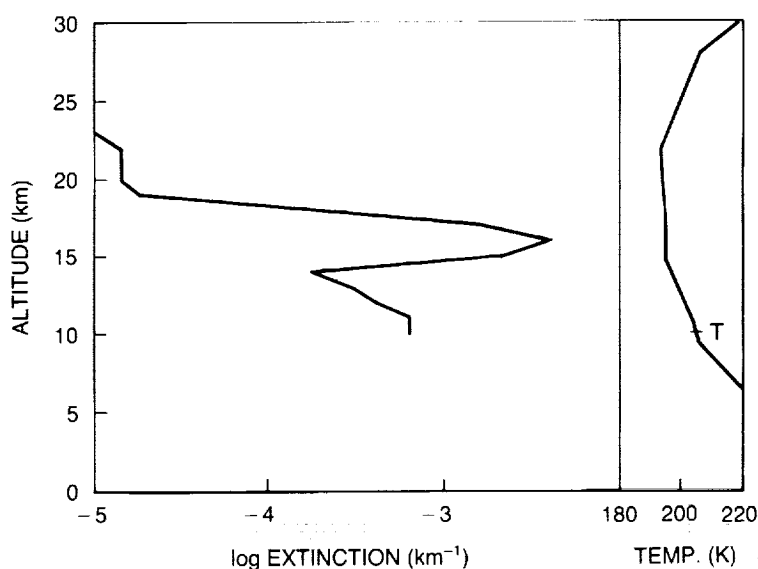


Figure 10.24 A polar stratospheric cloud extinction profile obtained from SAM-II data for January 23, 1979, at 68.7°N and 27°W (McCormick et al., 1982). The right panel shows the corresponding temperature profile.

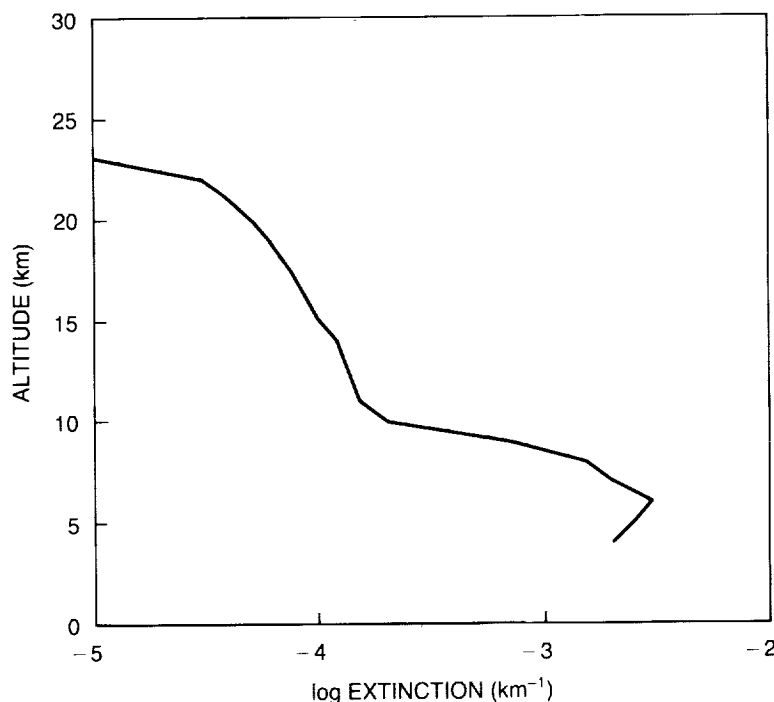


Figure 10.25 Average aerosol extinction profile for January 1979 in the Northern Hemisphere. The data correspond to all of the SAM-II observations for that month (McCormick et al., 1982).

profile, illustrated in Figure 10.25. The large anomalous extinction at about 15 km in Figure 10.24 suggested the presence of an optically dense aerosol layer at this height and location; these unusual aerosol manifestations were named polar stratospheric clouds by McCormick et al. (1982). Note from the accompanying temperature profile in Figure 10.24 the very low temperatures associated with the PSC.

The previously known nacreous or mother-of-pearl clouds are less frequent, lower latitude stratospheric clouds usually formed in the lee of mountain ranges. The relationship of high-latitude PSC's to nacreous clouds is not yet understood; the mother-of-pearl clouds, formed in regions strongly influenced by local dynamics, may be considered a subset of the more frequent PSC's.

An early workshop on the newly discovered polar stratospheric clouds described the initial understanding of this complex phenomenon (Hamill and McMaster, 1984). Considerable knowledge has accumulated since that time, as is summarized below.

10.6.1.2 PSC Properties

PSC's were first discovered in the Northern Hemisphere in January 1979 by the SAM-II satellite. At that time, 11 clouds were recorded. However, the SAM-II instrument samples only a limited part of the polar stratosphere, while PSC's can exist throughout the stratosphere. Indeed, when the south polar data for June to September 1979 were analyzed, hundreds of cloud events were detected, which is now understood to be related to the colder temperatures that exist in the southern winter stratosphere. Typically, the SAM analysis assumes that any observation of an extinction greater than $8 \times 10^{-4}/\text{km}$ at an altitude 3 km or more above the local tropopause constitutes a PSC sighting (McCormick et al., 1982). Although this definition is

AEROSOL ABUNDANCES AND DISTRIBUTIONS

somewhat arbitrary, it does allow a clear distinction between PSC's and the background stratospheric aerosols. Such a distinction could also have been made spectrally if SAM-II had had several wavelength channels for discrimination.

The vertical extinction profile derived from the SAM-II observations is an average value for the slant observation path of the instrument. The cloud actually may be localized along the observation path and within the SAM-II field of view. That field of view extends about 0.5 km vertically and 200 km horizontally at the minimum ray altitude. Thus, a dense (high optical depth) cloud that partially fills the field of view can be indistinguishable from a thinner cloud that completely fills the field of view. Moreover, the distribution of extinction along the observation ray cannot be finely resolved and may be highly localized. Nonetheless, extensive observations of PSC's now suggest that the aerosols are largely distributed as an extended haze, in which case the SAM-II data accurately represent average local extinction values.

Following the eruption of El Chichón, the threshold extinction for PSC detection had to be increased because of the volcanically enhanced background aerosol opacities. Accordingly, there is some ambiguity in the definition of PSC's and in the statistics of PSC's derived from the SAM-II observations, although such ambiguities are easily resolved in the long-term optical depth record from SAM-II (see Figure 10.7, for example).

In describing the general properties of PSC's, data are taken from observations in the pre-El Chichón years of 1979 to 1981, and in 1986. Following the eruption of El Chichón in the spring of 1982, the stratospheric aerosols, including those in the polar regions, were highly disturbed. In taking a conservative approach here, the satellite observations from 1982 through 1985 are not considered in any statistical or morphological analyses.

In 1979, 387 clouds were detected in the Southern Hemisphere in the winter season (June to September). The average cloud thickness was about 4.2 km (note, however, that for individual measurements SAM-II can resolve the vertical thickness only to the nearest kilometer). The average altitude of the peak extinction was ~ 15 km, and the average extinction (averaged over slant path for the layer of observation) was about $1.4 \times 10^{-3}/\text{km}$. The observed clouds were clustered around the longitude of Greenwich, with about 50 percent of the clouds appearing between 40°E and 40°W (see Table 10.8 for additional statistics).

In 1980, 433 clouds were recorded with an average thickness of ~ 5.8 km and an average peak extinction of about $1.4 \times 10^{-3}/\text{km}$. The average altitude of the clouds was near 15.6 km. Once again, the clouds were clustered around Greenwich with about 40 percent lying within 40 degrees of that parallel.

Table 10.8 Observed PSC Properties: 1979 to 1981

Year	Number of Cloud Observations	Average Cloud Thickness (km)	Maximum Extinction (km^{-1}) (km)	Altitude of Maximum Extinction (km)	Minimum Temperature (K)	Altitude of Minimum Temperature (km)
1979	387	4.2	0.00142	14.9	190	17.9
1980	433	5.8	0.00144	15.6	189	19.7
1981	449	4.2	0.00129	14.6	190	18.5

(P. Hamill, private communication, 1987)

In 1981, 449 clouds were seen with an average thickness of about 4.2 km, maximum extinction of about $1.3 \times 10^{-3}/\text{km}$, and average height of 14.6 km. Moreover, 42 percent lay within 40 degrees of Greenwich.

The average longitudinal distribution of the cloud sightings for 1979 to 1981 is illustrated in Figure 10.26. This preference for the clouds to lie near Greenwich is probably associated with the strong stationary wave-number-one feature in the Antarctic circumpolar flow, which is reflected in the temperature structure of the lower polar stratosphere in winter.

There is observational evidence that the heights of the PSC's decrease as the winter progresses. In Figure 10.27, measured cloud heights are plotted over a 13-week period of the Antarctic winter. It appears that the clouds have descended several kilometers over this time. The descent may be explained by the sedimentation of cloud particles or the slow subsidence of air in the winter polar vortex. The actual cause remains unresolved, although recent theories on PSC formation suggest that sedimentation may be sufficient to account for at least part of the decrease in elevation.

The frequency of cloud occurrence as a function of the minimum stratospheric temperature in the vicinity of the cloud (as deduced from NMC temperature fields) is illustrated in Figure 10.28 for the austral winter of 1981. In this year, no clouds were seen when temperatures exceeded about 200 K. Cloud formation seems to have a fairly high probability (~ 30 –50 percent) once the temperatures fall into the range of ~ 189 K to 195 K. At temperatures below ~ 185 K, the probability of PSC's approaches 100 percent. Interestingly, that temperature (185 K) roughly corresponds to the frost point of water at typical stratospheric mixing ratios. Thus, on observational evidence, there seem to be at least two distinct cloud types or growth stages: Type I, which

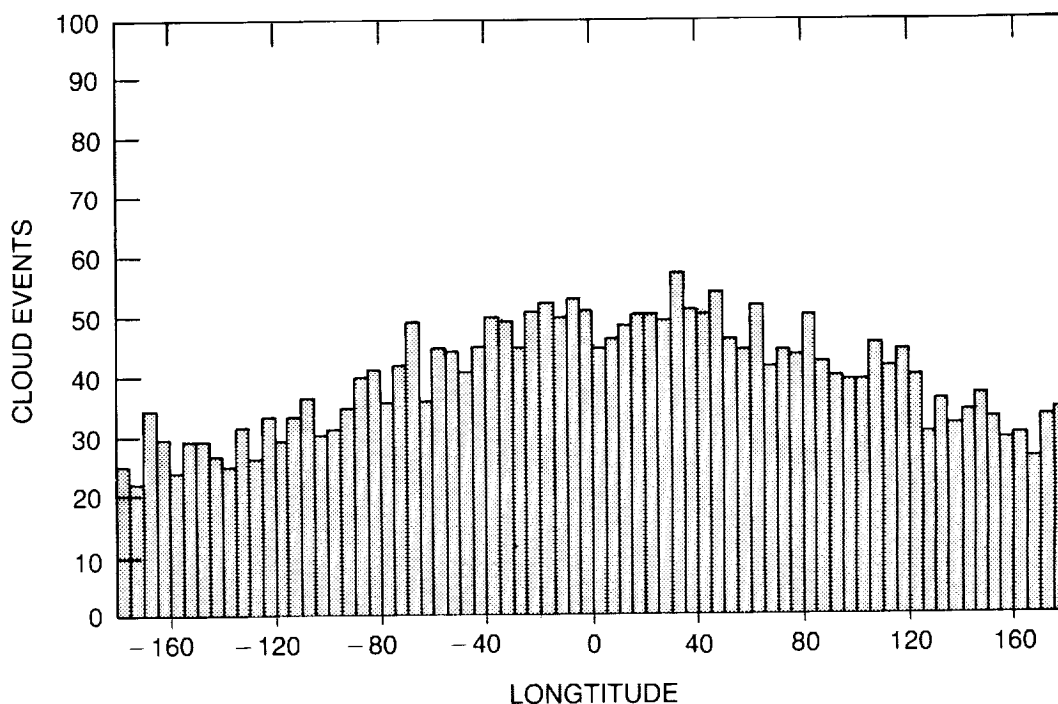


Figure 10.26 Histogram showing the longitudinal distribution of PSC events in the Southern Hemisphere for the winters of 1979–1981 based on SAM-II observations (P. Hamill, private communication, 1987).

AEROSOL ABUNDANCES AND DISTRIBUTIONS

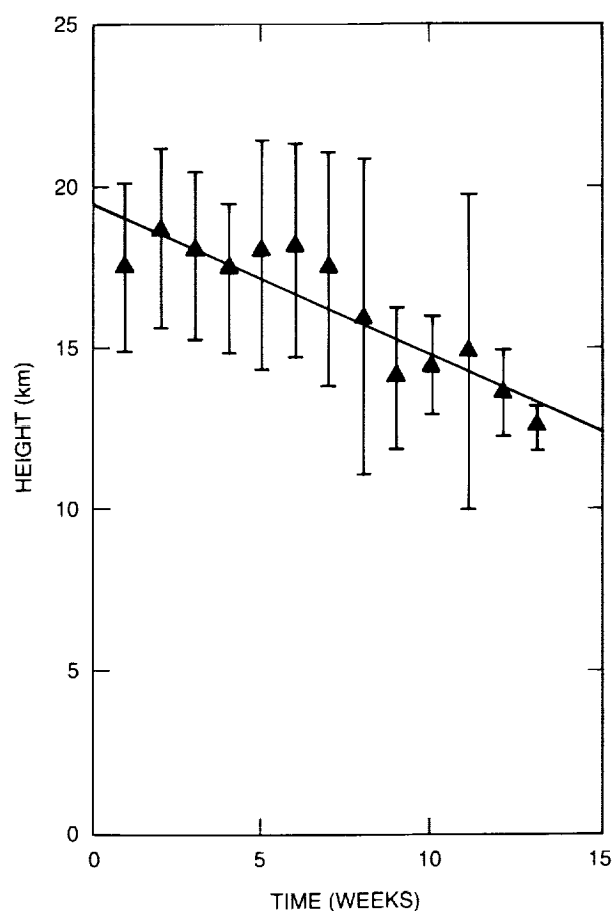


Figure 10.27 Average altitude of the maximum aerosol (PSC) extinction (on the vertical profile of extinction) for SAM-II satellite measurements over Antarctica during 13 weeks of a winter season (P. Hamill, private communication, 1987).

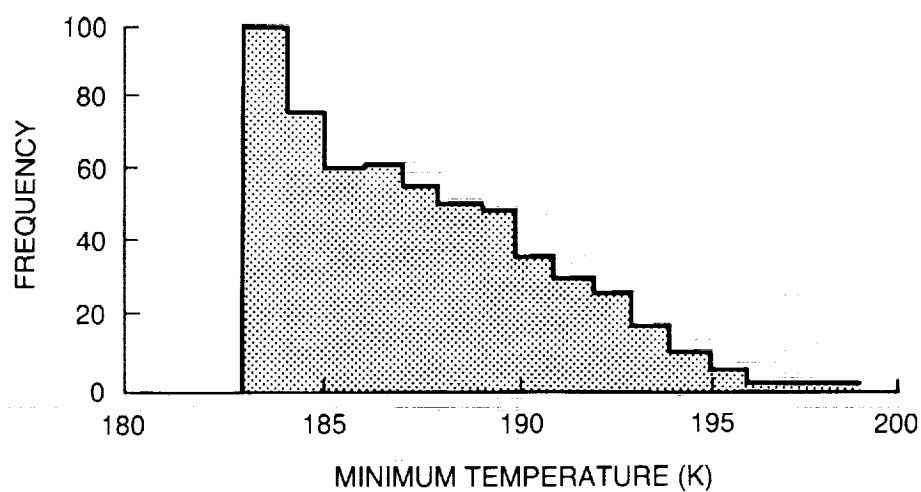


Figure 10.28 Frequency of cloud sightings by the SAM-II detector as a function of the minimum stratospheric temperature in the vicinity of the clouds, during the austral winter of 1981 (P. Hamill, private communication, 1987).

occurs at temperatures from about 195 K to temperatures as low as ~ 185 – 189 K, and Type II, which occurs below ~ 185 – 189 K. The Type II clouds are thought to be water ice clouds. As is discussed below, the Type I clouds are inferred to be composite nitric acid–hydrochloric acid–water ice aerosols (Toon et al., 1986; Crutzen and Arnold, 1986; Poole and McCormick, 1988; Hamill et al., 1988; Wofsy et al., 1988). Other evidence for these distinct cloud types is discussed in Section 10.6.2.4.

The variability in PSC properties can be illustrated by considering the measured cloud extinctions at a fixed pressure level without temporal and spatial averaging. Such a data record is provided in Figure 10.29 at 50 mb for the winter of 1981. The data clearly show that the clouds are highly variable from measurement to measurement, probably reflecting spatial inhomogeneity. Nevertheless, there is a clear trend for the extinction (at 50 mb) to increase during the winter and then decrease in the spring, leaving the stratosphere relatively clean. This observation is also consistent with the data in Figure 10.7, as discussed in Section 10.2.3.

An expanded view of the cloudiest period in Figure 10.29 is given in Figure 10.30. To interpret these data, recall that the satellite orbit precesses in longitude roughly 360° per day. Figure 10.30 shows an apparent periodicity in the extinction corresponding roughly to 24 hours in time or 360° degrees in longitude. This implies that PSC's are preferentially formed in the specific regions of the stratosphere that are the coldest. Support for this idea can be found in the corresponding 50 mb temperatures plotted in Figure 10.31. By comparing Figures 10.30 and 10.31, a close correlation can be seen between low temperature and high extinction with a repetition rate approximately each 360° degrees of scan in longitude. One interpretation of this behavior is that

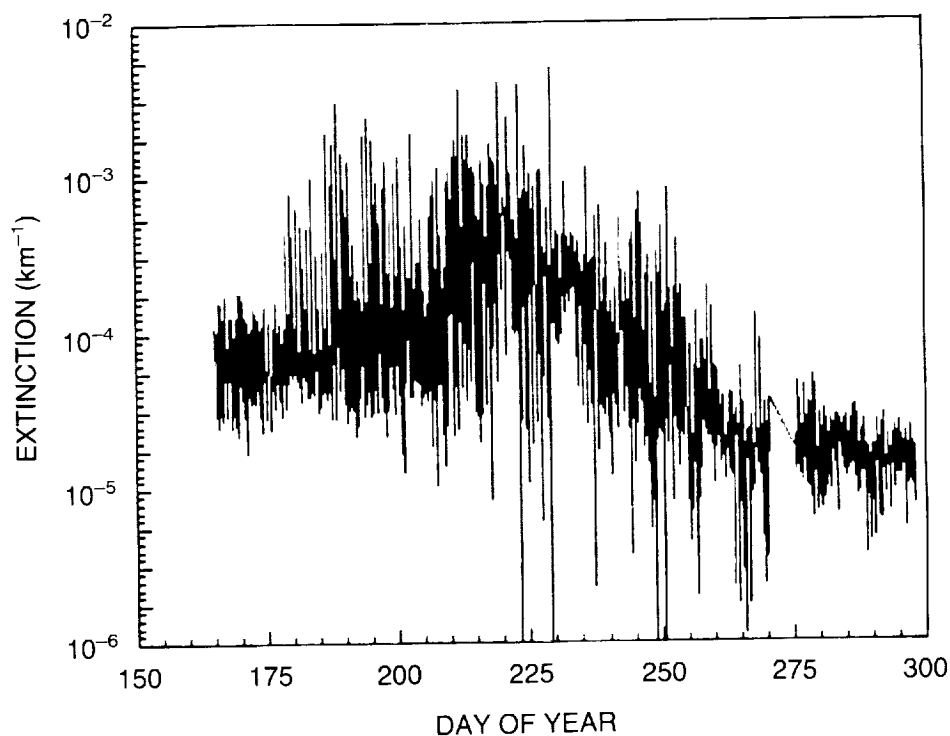


Figure 10.29 Detailed SAM-II extinction measurements at 50 mb over a 130-day period during the austral winter and spring of 1981. The data reflect the actual variability detected by the SAM-II sensor (P. Hamill, private communication, 1987).

AEROSOL ABUNDANCES AND DISTRIBUTIONS

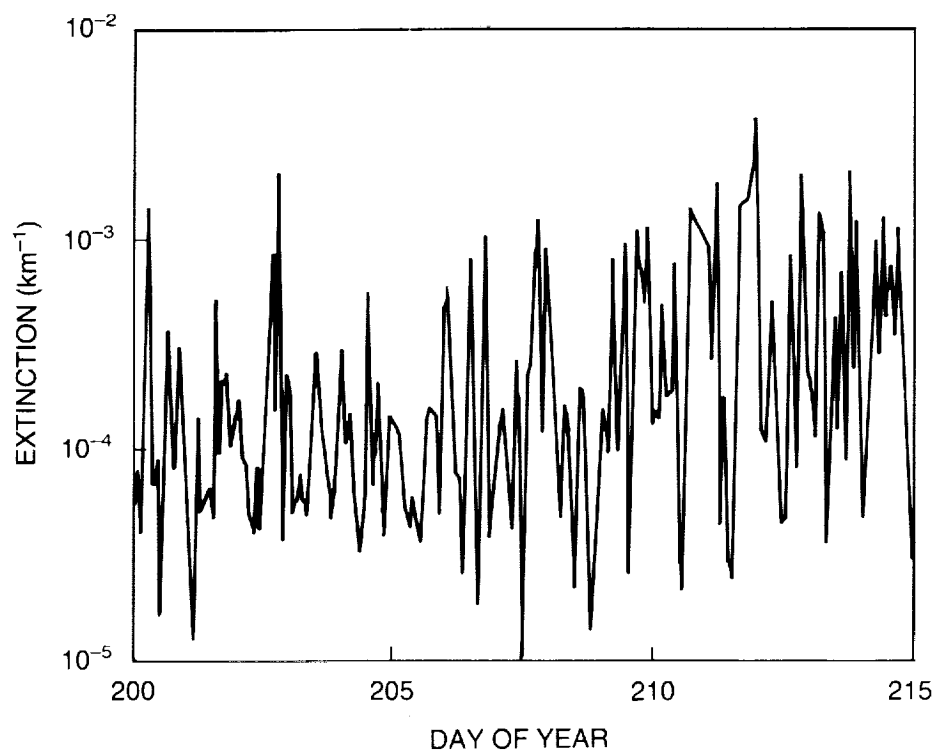


Figure 10.30 An expanded plot of a segment of the data in Figure 10.29 (P. Hamill, private communication, 1987).

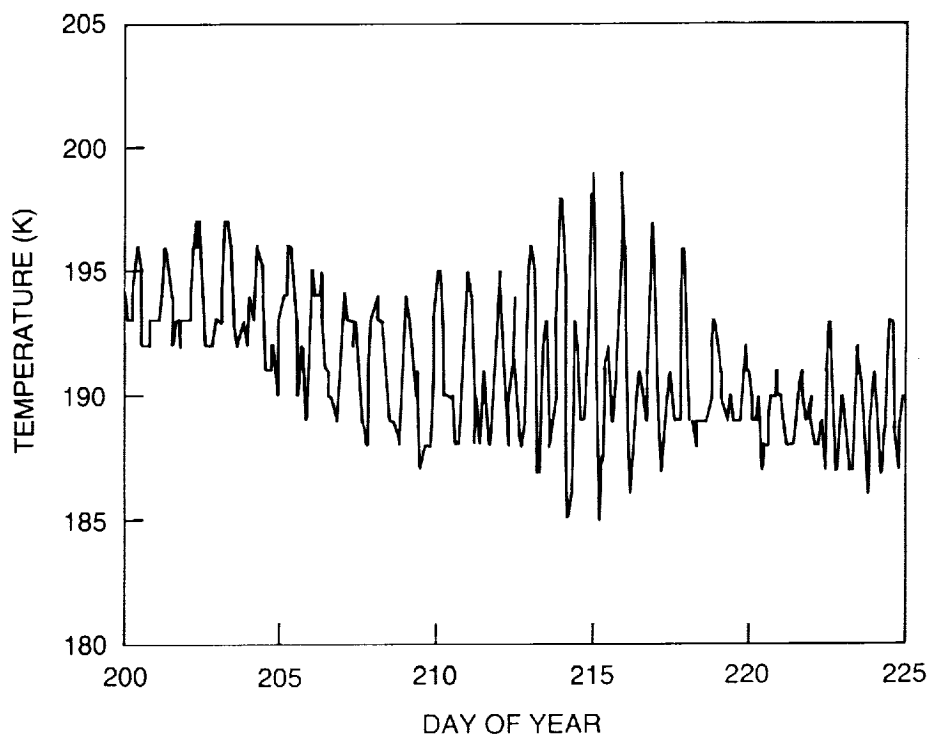


Figure 10.31 Temperature variations at 50 mb for the same period and geographical locations as in Figure 10.30 (P. Hamill, private communication, 1987).

approximately each 360 degrees of scan in longitude. One interpretation of this behavior is that the point of measurement is moving in and out of the cold polar vortex as the satellite precesses in longitude (McCormick et al., 1983). Another explanation is that air is being lifted and cooled locally, with the clouds appearing in the air parcels circulating through these cold regions.

The 1986 SAM-II data are of interest because the upper cutoff for extinction measurements ($10^{-2}/\text{km}$) was relaxed, and events of greater extinction were recorded and analyzed for the presence of polar stratospheric clouds. In that year, the total number of observations of clouds with extinctions greater than $0.8 \times 10^{-3}/\text{km}$ was about 920, with 82 observations of clouds with extinctions exceeding $1 \times 10^{-2}/\text{km}$. To limit the data set, P. Hamill (private communication, 1987) has compiled information on the subset of clouds with observed extinctions greater than $2 \times 10^{-3}/\text{km}$, of which about 290 were sighted during 1986. In Figure 10.32, the statistical characteristics of these Southern Hemisphere PSC's are summarized. The data show clearly that the PSC's began to appear frequently at temperatures below about 195 K, and increased in frequency as the winter season progressed (presumably, as the polar stratosphere continued to cool). Most of the clouds appear to reside between about 14 km and 20 km, but with a significant number of clouds up to about 24 km.

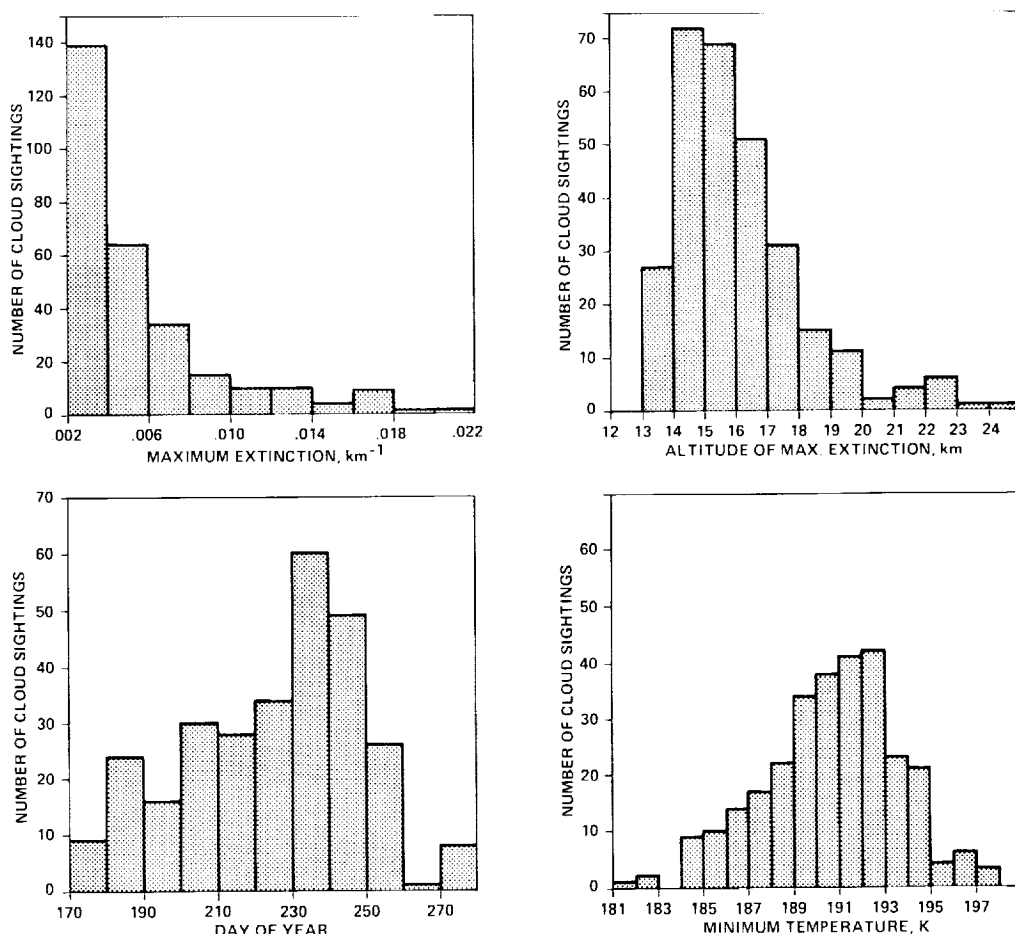


Figure 10.32 Histograms of the statistical characteristics of the total ensemble of Southern Hemisphere PSC's having extinctions greater than 2×10^{-3} detected by the SAM-II satellite in 1986. The number of clouds indicated corresponds to the range of the parameter delimited by the bar (P. Hamill, private communication, 1987).

AEROSOL ABUNDANCES AND DISTRIBUTIONS

10.6.1.3 PSC's in the Northern Polar Vortex

Although considerable attention has been focused on the ozone hole over Antarctica, relatively little attention has been given to the possibility of a similar phenomenon over the North Pole. This neglect is due in part to satellite observations indicating that the total ozone column content does not show a significant depletion in the Arctic spring. However, Evans (1987) has described a series of ozone profiles taken at Alert, Canada (82.5°N), during the breakup of the Arctic winter vortex; the individual profiles are very similar in character to profiles obtained by Hofmann et al. (1987a) from McMurdo during the breakup of the Antarctic vortex, displaying a "notching" effect or ozone depletion occurring in layers throughout the 12 km to 20 km altitude range. This may imply that analogous ozone depletion mechanisms are operating at both poles in the winter season.

Conditions in the core of the Arctic polar vortex may resemble those in the Antarctic, especially during those winters when the vortex is least disturbed and persists longest into the spring. Under these circumstances, some or all of the chemical processes believed to be occurring in the Antarctic stratosphere might be detected in the Arctic stratosphere as well.

Figure 10.33 summarizes the statistical characteristics of the PSC's observed by the SAM-II satellite in the northern polar region in 1986. There are significant differences in comparison to

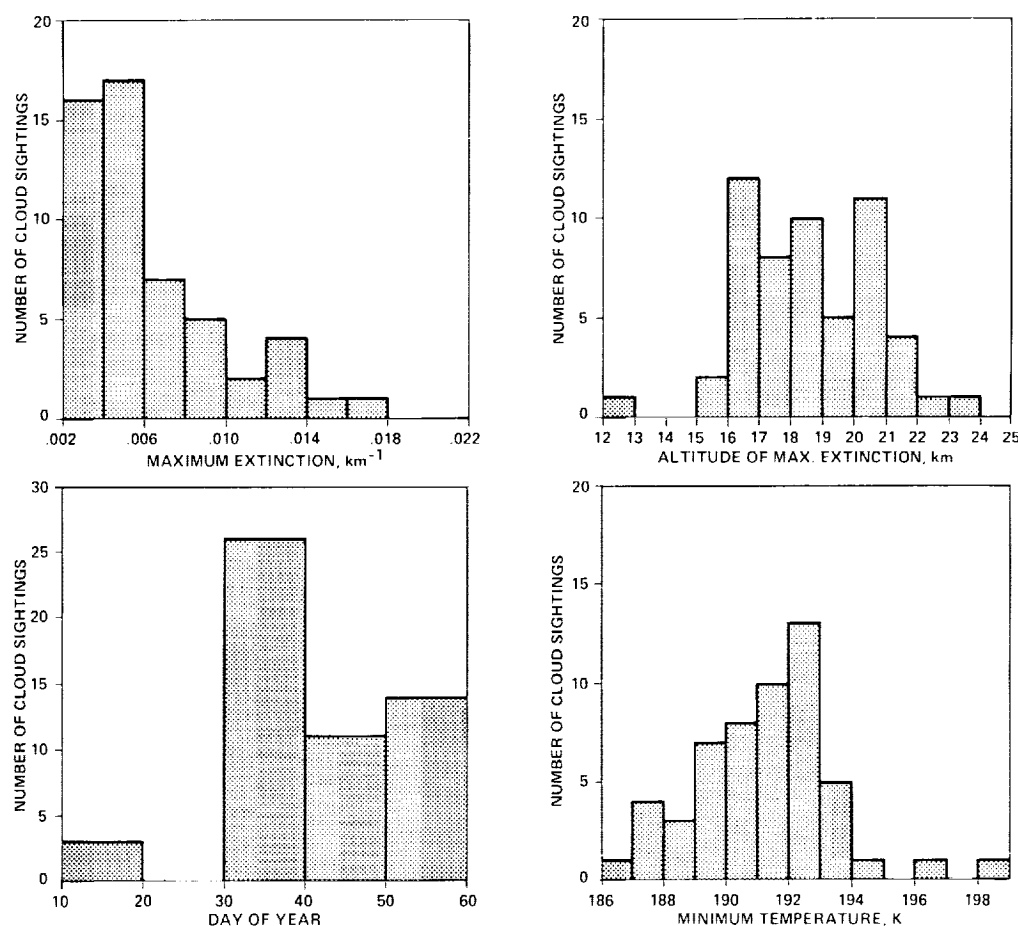


Figure 10.33 As in Figure 10.32, except for the PSC's observed in the Northern Hemisphere in 1986 (P. Hamill, private communication, 1987).

the southern polar data (Figure 10.32). The northern clouds tend to be much less frequent and reside at higher altitudes. However, the optical densities and seasonal behavior are roughly equivalent. Moreover, the frequency of appearance versus temperature is very similar in both hemispheres, suggesting a common microphysics (which is discussed in the next section).

10.6.1.4 Long-Term Trends in PSC Properties

The period of comprehensive observations of PSC's is relatively short, beginning in 1979 and extending to the present. Moreover, from 1982 to 1985, the El Chichón volcanic eruption filled the polar stratospheric regions with aerosols that masked to some extent the direct observations of PSC's (see Figure 10.7). Because of these constraints, it is not yet possible to make a definitive statement about possible long-term trends in PSC properties. Nevertheless, the most recent SAM-II satellite measurements indicate a marked increase in Antarctic PSC occurrence in 1987 as compared to previous years.

Figures 10.34a–d show the individual SAM-II measurements of aerosol extinction in the southern polar region for 1979, 1985, 1986, and 1987. The data are presented in terms of the equivalent local aerosol extinction at 18 km, which is representative of the PSC formation region. The plots clearly show the onset of PSC's in mid-June, with dissipation of the clouds in September. The influence of volcanic aerosols is seen as elevated background extinctions in these figures. There is a noticeable increase in cloud sightings between 1979 and 1985–87; however, keep in mind that the nominal upper extinction cutoff of $10^{-2}/\text{km}$ for PSC's was relaxed in 1986, and more cloud events were subsequently recorded—see Section 10.6.1.2. It appears that the onset of PSC formation is occurring earlier in the winter in recent years, and that the PSC's are persisting longer into the spring, particularly in 1987 (Figure 10.34d). An analysis of the SAM-II data for September 10 to 20 and September 20 to 30 is provided in Figures 10.35a and b, respectively, for each year represented in Figure 10.34. These data indicate that the frequency of cloud events with high extinctions is substantially greater in 1987 later in the spring season than in earlier years (of SAM-II observations). Indeed, PSC events were recorded into October 1987 for the first time. Statistically, the years 1979, 1985, and 1986 are not distinguishable in this regard (allowing for interannual variability seen throughout the SAM-II record).

The earlier onset of PSC's, their greater frequency over the winter, and their persistence into the spring may be associated with a general cooling of the late winter–early spring polar vortex in recent years, with a significant quasi-biennial signal (see Section 11.2.3). The largest Antarctic ozone reductions to date were also measured in 1987, suggesting a possible mechanistic relationship between PSC formation, ozone depletion, and stratospheric cooling (see Sections 6.4.4 and 11.3.3). A trend in the occurrence of PSC's could also be caused by changes in stratospheric composition, including trends in the abundances of water vapor and nitrogen oxides, which condense to form cloud particles (as described in the following section). However, no clear trends in either H_2O or NO_x over the period of PSC observation have been unambiguously identified (see Chapter 8). Because reliable measurements of these trace species are very limited, the possibility of trends in their concentrations cannot be ruled out.

10.6.2 Physical Chemistry and Microphysics of PSC's

Polar stratospheric clouds may influence the formation of the Antarctic ozone hole (Solomon et al., 1986a; Crutzen and Arnold, 1986; McElroy et al., 1986a; Hamill et al., 1986). Recent laboratory studies (e.g., Molina et al., 1987) and field measurements (see Chapter 11) strongly

AEROSOL ABUNDANCES AND DISTRIBUTIONS

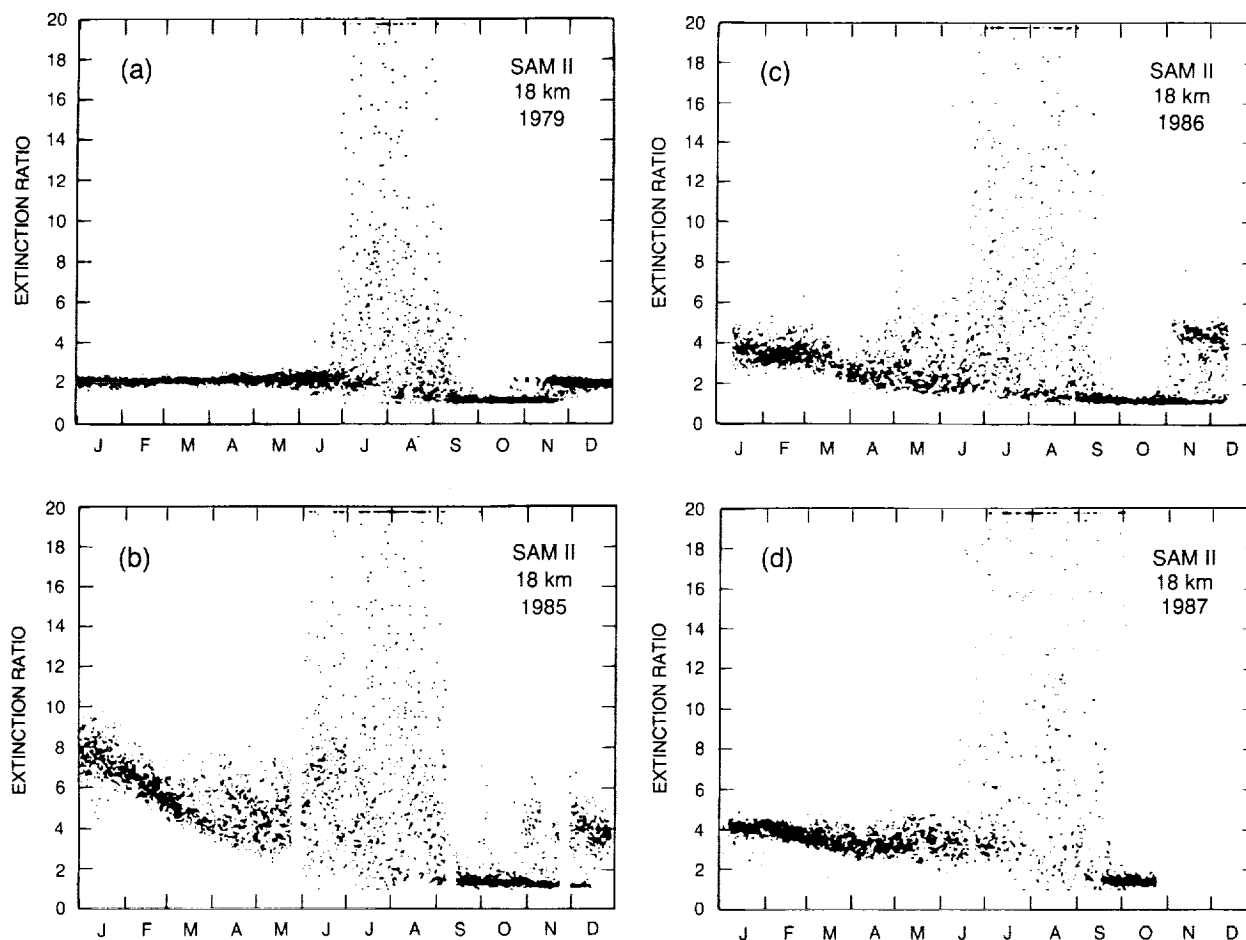


Figure 10.34 Extinction ratios at 18 km versus time as measured by the SAM-II system in the Southern Hemisphere (i.e., the total extinction including aerosol effects obtained by the satellite limb sensor, divided by the extinction caused by molecular Rayleigh scattering obtained from an atmospheric model; ratios that exceed unity are associated with aerosol extinction). The data are presented as scatter plots for a) 1979, b) 1985, c) 1986, and d) 1987. Extinction ratios greater than ~ 20 are aggregated at the top of the plots. The differences between the background levels for each year reflect the presence of volcanic aerosols from the eruptions of El Chichón in April 1982 and Ruiz in November 1985; the volcanic anomaly is seen to decay from 1985 through 1987 (M.P. McCormick, private communication, 1988).

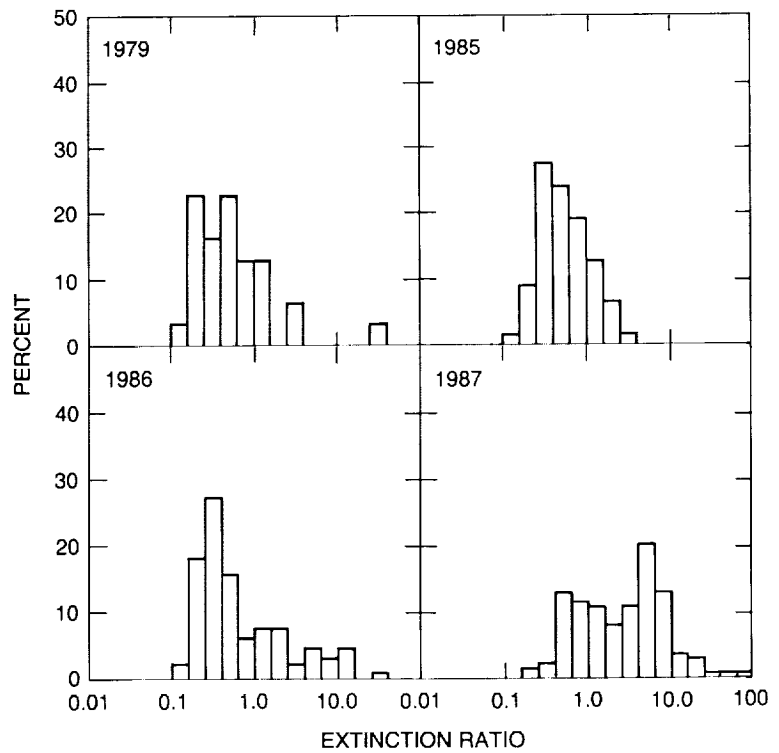
support this idea. The statistical characteristics of PSC's (as described in previous sections) are also consistent with the appearance and behavior of the ozone hole. To evaluate properly the role of PSC's, and to develop a realistic model for cloud-chemistry interactions, it is necessary to understand the microphysics of the cloud particles. The polar stratospheric clouds may be composed of ice crystals condensed on a core of sulfuric acid, or may be frozen nitric acid, or may be a combination of these including condensed hydrochloric acid. Some of these possibilities are discussed below. The microphysical time constants relevant to PSC evolution can be derived from the data in Table 10.2.

10.6.2.1 Sulfuric Acid Ice Clouds

Steele et al. (1983) originally proposed that PSC's were formed on the background stratospheric sulfate particles. If these particles were supercooled droplets, their composition (i.e., the

AEROSOL ABUNDANCES AND DISTRIBUTIONS

(a)
SAM II EXTINCTION RATIO FREQUENCY
SEP. 10—SEP. 20 AT 18 km



(b)
SAM II EXTINCTION RATIO FREQUENCY
SEP. 20—SEP. 30 AT 18km

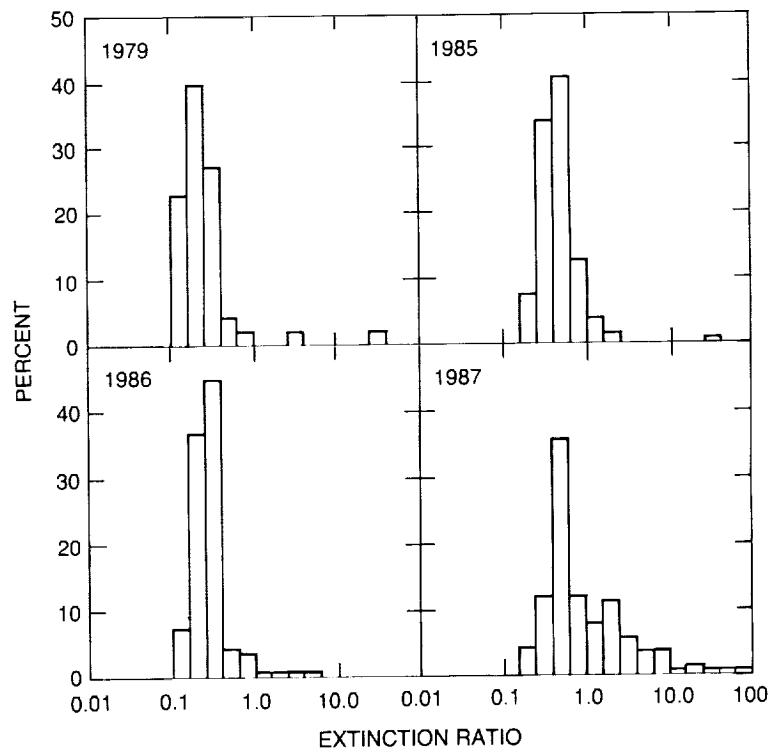


Figure 10.35 Relative frequency (in percent) of observed aerosol extinction ratios at 18 km for 1979 and 1985 through 1987 (as in Figures 10.34a–d) for two specific intervals: (a) September 10 to 20 and (b) September 20 to 30 (M.P. McCormick, private communication, 1988).

AEROSOL ABUNDANCES AND DISTRIBUTIONS

weight fractions of water and sulfuric acid in solution) would maintain close equilibrium with the ambient water vapor concentration at all altitudes, because the water vapor concentration exceeds the sulfuric acid concentration by several orders of magnitude. Hence, as the environmental temperature decreased (for example), the equilibrium H_2O vapor pressure of the solution would decrease, allowing the droplets to absorb additional water and grow larger and more dilute—through the process of heteromolecular condensation (Hamill, 1975). In the later stages of growth, at even lower temperatures, the droplet would be essentially pure water (which might be frozen). At this stage, further growth could not be maintained by continuing dilution, and growth would cease until the temperature had fallen below the local frost point (of water vapor).

Steele and Hamill (1981) first delineated this aerosol growth mechanism for stratospheric aerosols. Steele et al. (1983) showed that the theoretical relationship between aerosol extinction and temperature is in reasonable agreement with the 1979 SAM-II data at the 50-mb and 100-mb pressure levels.

Although the stratospheric aerosols were assumed to be highly supercooled, logically they would eventually freeze. Then, if temperatures fell below the local frost point, water vapor could deposit on the particle surfaces to form a water ice crystal with a dilute sulfuric acid core. If a large fraction of the sulfate particles were thus activated as water ice nuclei, a high concentration of relatively small ($\sim 10\ \mu\text{m}$) ice particles would result. In this case, very large optical depths would occur when temperatures fell below about 185 K. On the other hand, if only a small fraction of the stratospheric aerosols were activated as ice nuclei, fewer larger ice crystals would be formed, with a lower optical depth.

Based on satellite observations, the amount of water vapor in the polar stratosphere is in the range of 3 to 5 ppmv. At a pressure level of 50 mb (about 20 km), the H_2O partial pressure is therefore about $1.5\text{--}2.5 \times 10^{-4}$ mb. The saturation vapor pressure over ice exceeds 2.5×10^{-4} mb for all temperatures greater than 188.6 K (List, 1951). Consequently, pure ice crystals would not form until the air at 50 mb had fallen below this extremely cold temperature. At 100 mb (about 14 km), pure ice crystals could not form until temperatures had dropped below about 192 K. Furthermore, if the air is desiccated, as recent observations indicate (Chapter 11), the formation of pure water ice clouds would require an even larger temperature depression. For example, if the water vapor mixing ratio were 1 ppmv, the temperature required to condense pure ice clouds at 50 mb would be 179 K, and, at 100 mb, 183.4 K.

Extremely low temperatures have been observed in the Antarctic stratosphere, particularly near the pole. However, the SAM-II instrument is restricted to make observations at latitudes below about 83° , while the coldest air masses are generally found at higher latitudes. Even so, temperatures below 190 K are frequently observed at latitudes within the SAM-II field of view (for example, see Figure 10.28). Moreover, individual air parcels within the polar vortex at lower latitudes can be exposed to colder temperatures as the air circulates around the pole and is vertically displaced.

It is possible that ice clouds form during the early part of winter and that sedimentation of the crystals transports water out of the stratosphere. The remaining air would then be drier, which is consistent with observations (Chapter 11). Sanford (1977) rejected this mechanism because the fall velocities of particles about 1 micron in radius (the particle size deduced from the optical manifestations of mother-of-pearl clouds) are too low (see Table 10.2). However, it is possible

that a smaller number of larger ice crystals are nucleated from the stratospheric aerosols within the winter polar vortex, as noted above (Hamill et al., 1988), and that these particles rapidly fall to lower altitudes. Rosen et al. (1988) have suggested that the formation of such polar stratospheric cirrus clouds (Type II PSC's) is more consistent with lidar backscatter and satellite extinction measurements than is the exclusive formation of extended aerosol hazes (Type I PSC's).

10.6.2.2 Nitric Acid Ice Clouds

Recently, Toon et al. (1986) and Crutzen and Arnold (1986) independently suggested that polar stratospheric cloud particles might be formed of frozen nitric acid. Toon et al. proposed that hydrochloric acid ice might condense as well. Figure 10.36 gives the freezing point temperature of aqueous solutions of nitric acid (Pickering, 1893). Nitric acid solutions of any composition should be frozen at the normal temperatures of the lower stratosphere (≤ 220 K), since the minimum freezing point is 229 K (corresponding to the eutectic near 70 percent weight fraction of HNO_3). Likewise, the condensation of nitric acid vapor on pre-existing surfaces should occur in the form of various $\text{HNO}_3/\text{H}_2\text{O}$ crystalline phases.

Toon et al. pointed out that the vapor pressures of both H_2O and HNO_3 over supercooled or frozen nitric acid mixtures at normal stratospheric temperatures are much greater than the respective partial pressures of these species in ambient stratospheric air. Hence, nitric acid particles cannot form in the stratosphere for typical background conditions. Moreover, extrapolations of the vapor pressures of supercooled $\text{HNO}_3/\text{H}_2\text{O}$ solutions indicate that such solutions are unlikely to exist even at the colder temperatures of the polar winter stratosphere.

Rough estimates of the HNO_3 and H_2O vapor pressures over $\text{HNO}_3/\text{H}_2\text{O}$ ice crystals as a function of temperature are presented in Figures 10.37a and b and 10.38 (Clavelin and Mirabel,

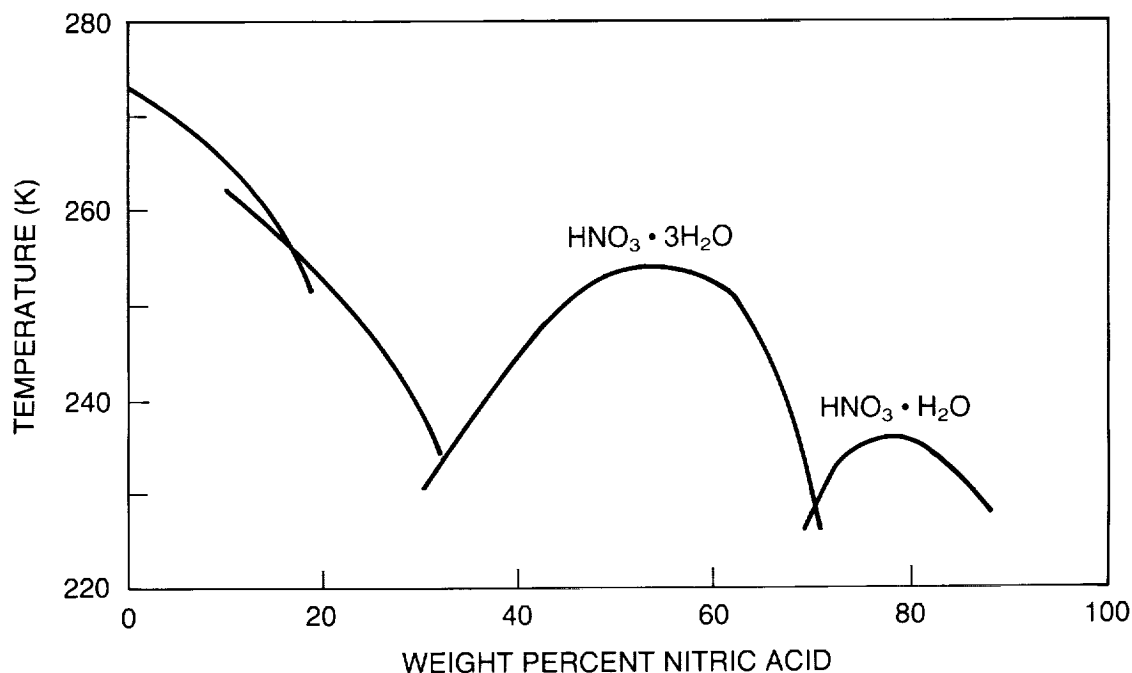


Figure 10.36 Freezing-point curves for nitric acid aqueous solutions as a function of the nitric acid weight percent of the solution at a pressure of 1 atmosphere (Pickering, 1893).

AEROSOL ABUNDANCES AND DISTRIBUTIONS

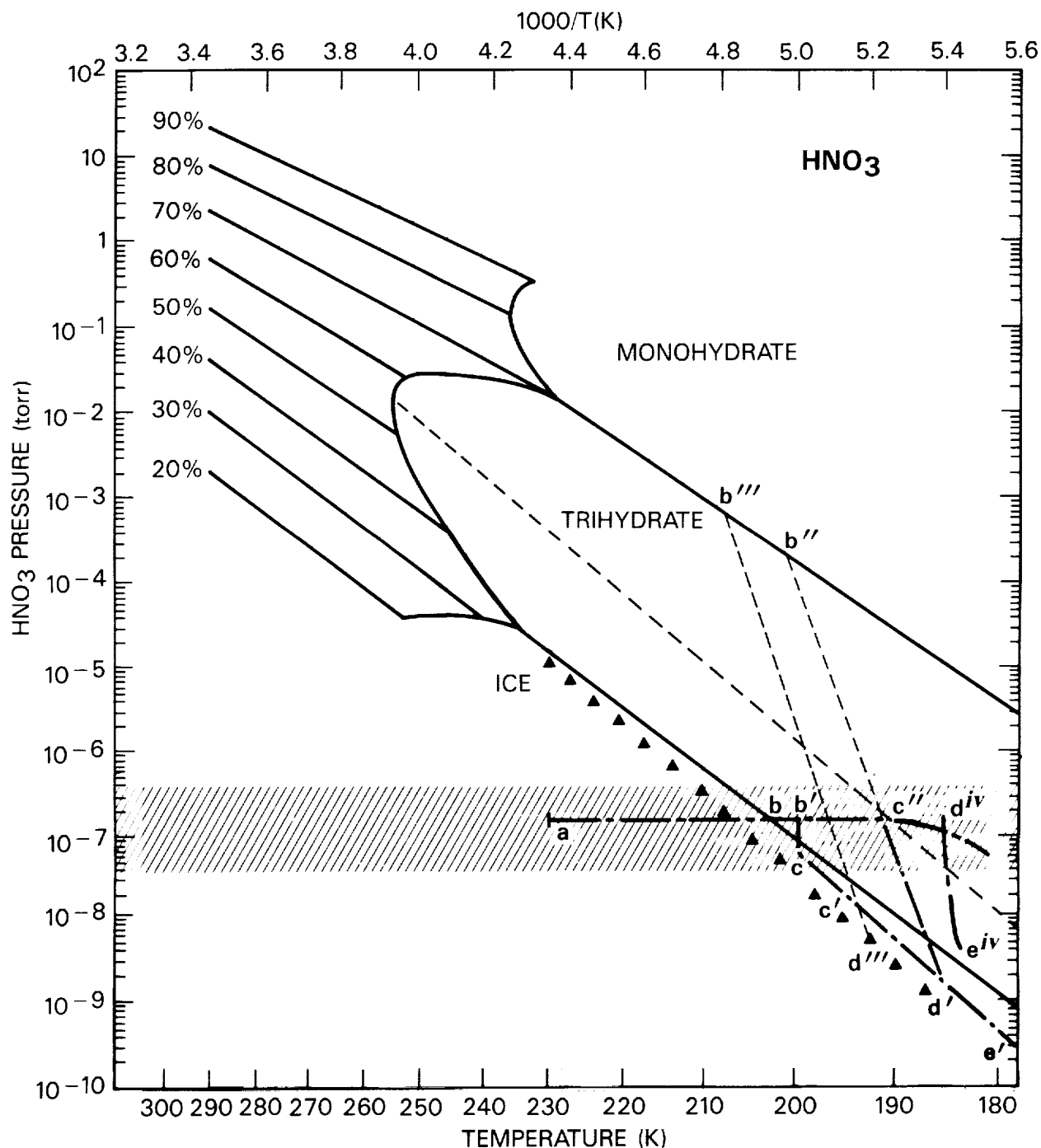


Figure 10.37a Vapor pressures of HNO₃ over aqueous solutions and ices of various compositions as a function of temperature (1000/T). The vapor pressures for the liquid-phase mixtures are based on laboratory data (see Toon et al., 1986). The vapor pressures for the solid phases have been estimated using thermodynamic arguments. Two extrapolations are shown. The solid lines originating at the quadruple points define the phase boundaries between distinct crystalline forms of HNO₃/H₂O ices, and are based on estimates of the partial molar enthalpies of HNO₃ and H₂O in each pure crystalline phase. The dashed lines correspond to the vapor pressure of trihydrate ice that is likely to condense from the vapor phase under stratospheric conditions (Hamill et al., 1988; Turco et al., 1989).

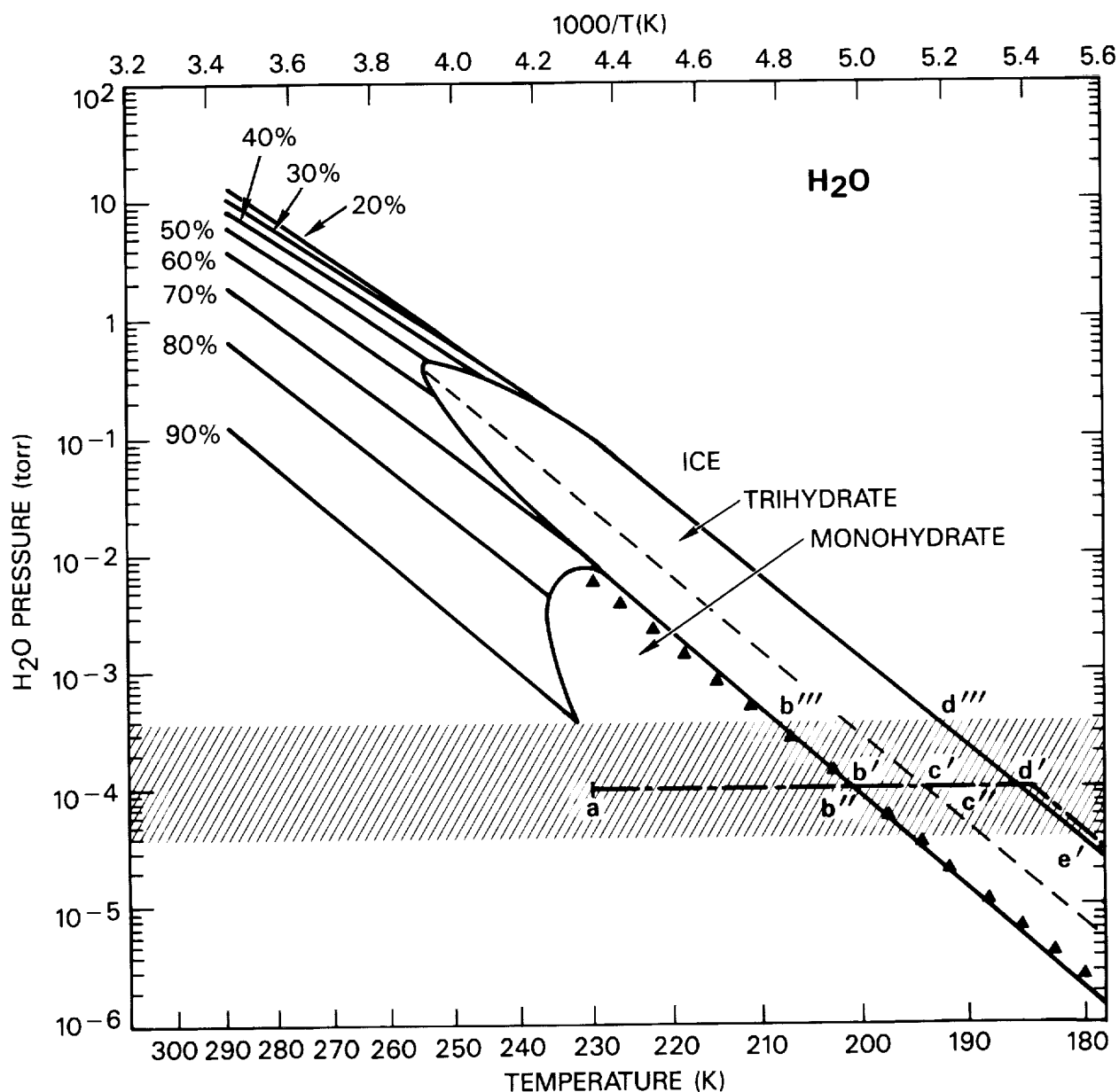


Figure 10.37b Same as Figure 10.37a, except for the H₂O vapor pressures (Hamill et al., 1988; Turco et al., 1989).

1979; Toon et al., 1986; Crutzen and Arnold, 1986; McElroy et al., 1986; Hamill et al., 1988). These vapor pressures are uncertain because measurements corresponding to the extreme conditions of the polar winter stratosphere are lacking. Representative ambient partial pressures of HNO₃ and H₂O in the lower stratosphere are indicated by the hatched bars in Figures 10.37a and b. It is apparent that the partial pressures fall below the vapor pressures of the principal hydrate ice

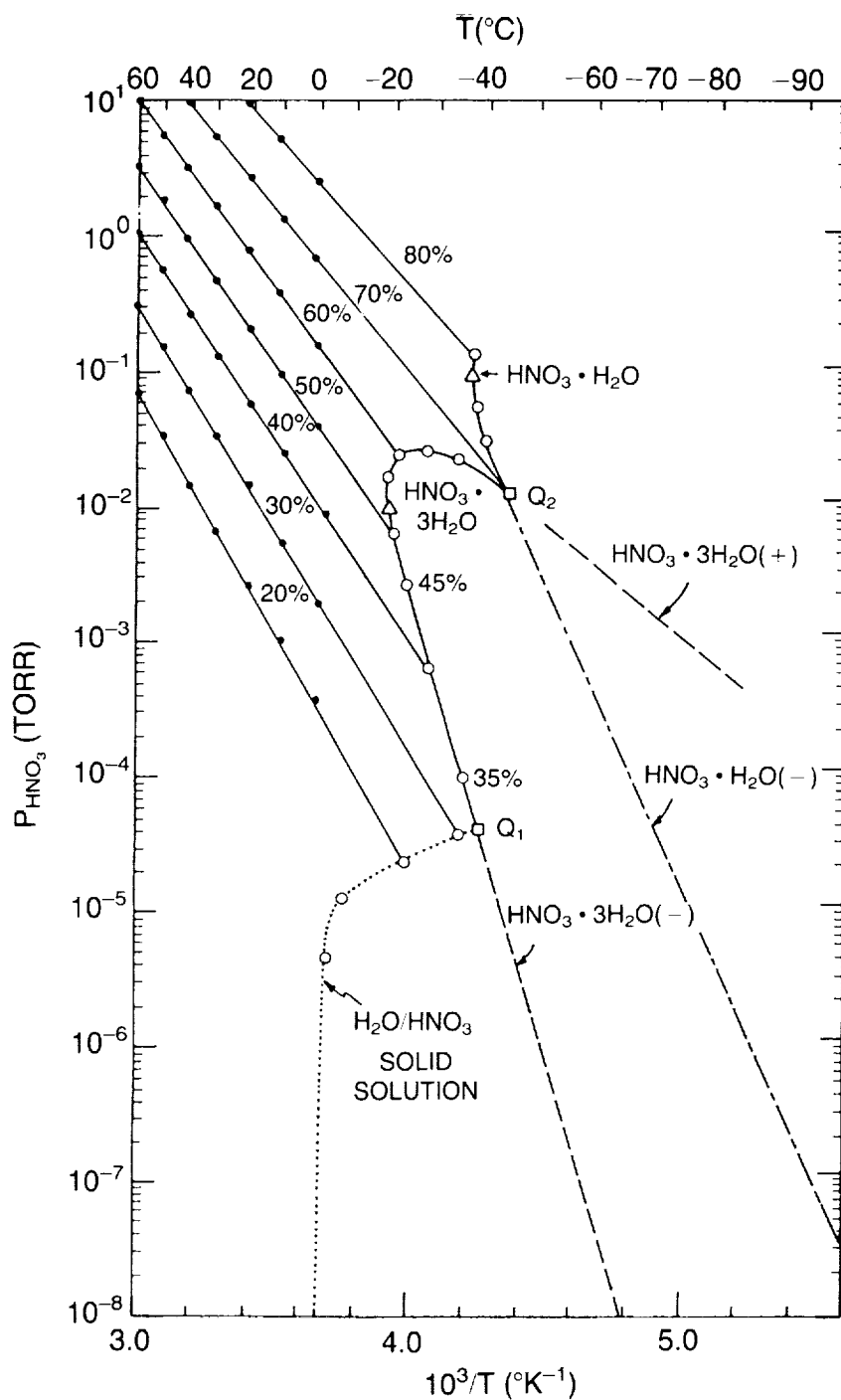


Figure 10.38 HNO₃ vapor pressures over aqueous HNO₃ solutions and solid phases. Closed circles represent HNO₃ fugacities reported by Clavelin and Mirabel (1979), and the open circles represent the freezing points of Pickering (1893) placed on the fugacity lines to define the phase transition. The liquid solution compositions are labeled by HNO₃ weight percentage. The locus of open circles defines the solid-liquid phase boundary. The dotted line denotes the phase boundary between liquid solution and solid solution. The dashed lines depict estimates of the vapor pressures over the crystalline hydrate phases. Imperfect crystal phases depleted in HNO₃ are labeled with (-); phases enriched in HNO₃ are labeled with (+) (From McElroy et al., 1986, with modifications).

forms at temperatures above about 200 K. At lower temperatures, however, crystals with the composition of the trihydrate (~ 54 percent HNO_3 by weight) appear to be thermodynamically stable (Toon et al., 1986; Crutzen and Arnold, 1986; also, Hamill et al., 1988, provide a detailed discussion of the likely composition and morphology of the condensate). An alternative extrapolation of the hydrate vapor pressures is presented in Figure 10.38, from which McElroy et al. (1986a) concluded that crystals nearer to the composition of the monohydrate (~ 78 percent HNO_3 by weight) are preferred thermodynamically.

If the gas phase partial pressures of HNO_3 and H_2O both lie within the vapor pressure stability regimes for a specific hydrate (e.g., as indicated by point c in Figures 10.37a and b), then gas-phase molecules can deposit on pre-existing surfaces as crystals of that hydrate. If either of the partial pressures lies outside of its respective stability regime for that hydrate, or moves outside of the stability regime (for example, because of a change in temperature), then the hydrate is unstable and either will not form or will evaporate. It is unlikely that pure crystal hydrates will precipitate in the stratosphere, however. The expected ice forms would consist of impure crystals, amorphous ices, and solid solutions of HNO_3 in water ice (Hamill et al., 1988).

The germination of polar stratospheric clouds may involve ternary mixtures of H_2SO_4 - HNO_3 - H_2O . The vapor pressures and other properties of such mixtures at low temperatures are unknown. However, the properties may not be too different from those of H_2SO_4 - H_2O and HNO_3 - H_2O binary systems (Kiang and Hamill, 1974).

While it is not possible to deduce precisely the mechanisms by which nitric acid clouds form, it is reasonable to assume that, as the temperature of the stratosphere decreases, crystals of nitric acid ice will condense on frozen sulfuric acid particles.

These frozen $\text{HNO}_3/\text{H}_2\text{O}$ aerosols would initially constitute a haze of micron-sized particles (Type I PSC). The ice aerosols would grow and evaporate as the temperature fluctuated around the condensation temperature. Although the composition of the solid phase is uncertain, it may consist of various impure crystals approaching the composition of nitric acid trihydrate ice (roughly 50 percent HNO_3 by weight). If it is assumed that all of the stratospheric sulfate aerosols are nucleated into nitric acid particles in this way, Type I PSC's would contain about 1 to 10 particles per cubic centimeter. Then, if all of the available nitric acid were condensed onto these particles, the average particle radius would be roughly $0.3\ \mu\text{m}$ to $0.5\ \mu\text{m}$. The smaller the fraction of sulfate aerosols initially converted into nitric acid particles, the greater the average size of the haze particles in Type I PSC's. Moreover, as time progresses, the haze particle size distribution would tend to evolve, under the influence of the Kelvin vapor pressure effect, toward one with a smaller number of much larger particles (Pruppacher and Klett, 1978).

10.6.2.3 Hydrochloric Acid Ice

Toon et al. (1986) suggested that, under the environmental conditions of the polar winter stratosphere, HCl vapor might condense as ice with water vapor. Extrapolating measured vapor pressures of HCl and H_2O for liquid solutions, Toon et al. concluded that the HCl composition of the ice would be less than 20 percent. In other words, the common $\text{HCl}/\text{H}_2\text{O}$ hydrates (dihydrate and trihydrate) could not form (McElroy et al., 1986a), and only amorphous ices or solid solutions of HCl in ice could condense. Recently, Molina et al. (1987) and Wofsy et al. (1988) measured the composition and vapor pressures of HCl solid solutions and confirmed that, under polar winter stratospheric conditions, such condensates are stable (with HCl weight fractions in the range of 1 to 5 percent). It is also expected that HCl would be absorbed into nitric acid ices.

AEROSOL ABUNDANCES AND DISTRIBUTIONS

The presence of HCl in solid solution leads to the possibility of rapid "heterogeneous" reactions involving PSC particles; studies of potentially important heterogeneous chemical processes are discussed in Chapter 11.

10.6.2.4 Ice Clouds

The discussion of water ice condensation on sulfuric acid aerosols in Section 10.6.2.1 applies as well to water ice condensation on nitric acid aerosols below the frost point of water. In this case, a few of the nitric acid crystals would grow rapidly into large ice crystals (Heymsfield, 1986; Rosen et al., 1988; Hamill et al., 1988). Heymsfield (1986) has, in fact, proposed that the PSC's should be more like cirrus clouds than activated aerosol hazes. However, considerable evidence now is available pointing to the existence of two distinct cloud morphologies (Type I and II PSC's) (also see below).

10.6.3 Radiative Properties of PSC's

10.6.3.1 PSC Lidar Backscatter and Polarization Characteristics

In Figure 10.39, a lidar return signal is shown for a PSC at 86°N observed with the NASA/Langley airborne lidar system. Although obtained in the Northern Hemisphere, the enhanced signal is similar to cloud returns measured by Iwasaka (1986) at Syowa Station, Antarctica. The

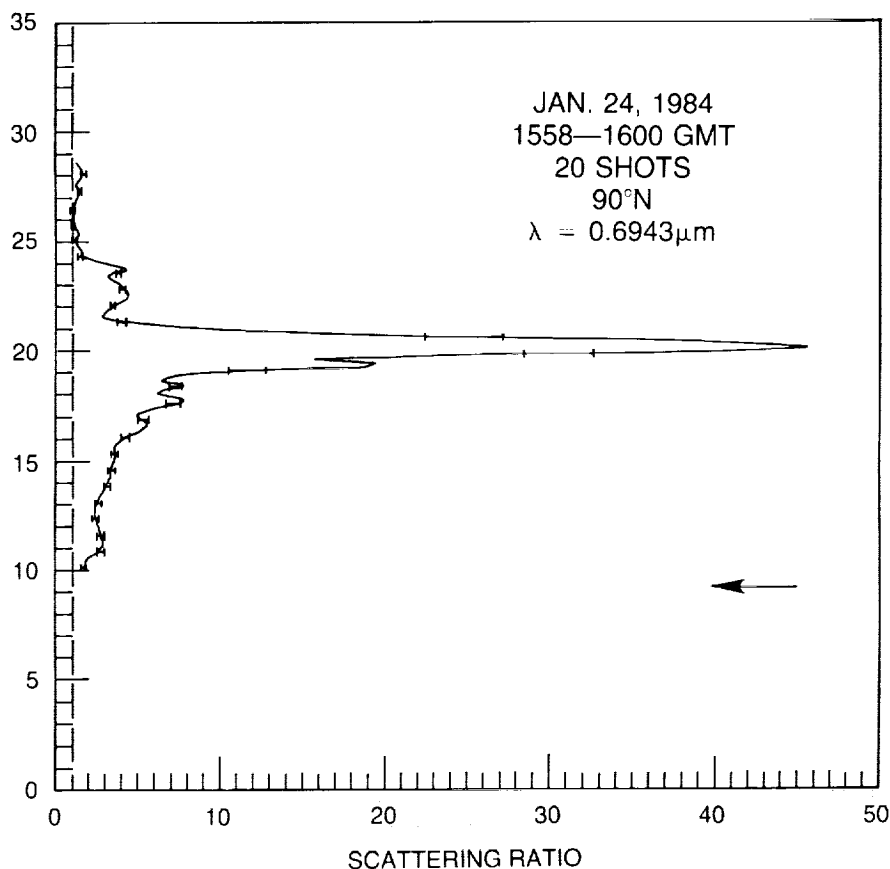


Figure 10.39 Lidar backscatter ratio for a PSC at 90°N measured with the NASA/Langley airborne lidar system (M.P. McCormick, private communication, 1987).

very large backscatter ratio is consistent with a cloud holding up to ~ 10 large ice crystals per cubic centimeter. On the other hand, most of the SAM-II extinction profiles are consistent with the smaller optical depths associated with nitric acid haze (although this may be due, in part, to the limited latitude range of the SAM-II observations that excludes the coldest polar regions with the greatest likelihood of very dense clouds). Hence, lidar backscatter data provide some supporting evidence for two distinct cloud types.

The depolarization of lidar signals backscattered from PSC's has also been measured in both the Arctic and Antarctic winter regions. Airborne lidar experiments were conducted during January 1984 and January 1986 at high northern latitudes by the Langley research team. The backscatter intensities and depolarization ratios were measured on both occasions (Kent et al., 1986; Poole, 1987; Poole and McCormick, 1988). Independently, Iwasaka (1986) obtained backscatter and depolarization data at Syowa Station (69°S) in the austral winter of 1983.

On January 24, 1984, lidar data were collected along two segments of a flight between Thule, Greenland, and the North Pole. The two segments corresponded to regions in which 50 mb temperatures were about 188 K and 190 K, respectively. Along the segment at the colder temperature, which approached the local frost point of water, the backscatter ratios were 10 to 15 and the depolarization ratios were 0.2 to 0.4. These values would be expected for a cloud of relatively large, irregular ice crystals. On the warmer segment (approximately 2°C above the frost point), the backscatter ratios were smaller, ~ 5 , and the depolarization ratios were less than 0.1. These latter values are consistent with a size distribution of relatively small ice crystals. In regions that were considerably warmer than 190 K, normal stratospheric backscatter ratios in the range of 1.1 to 1.5 were observed, with little depolarization of the signal.

On the 1986 Langley lidar mission, a PSC was encountered at 60°N with local temperatures (at 50 mb) 3° – 6°C above the frost point. Again, backscatter ratios showed maximum values of about 5, and the depolarization ratio was never greater than 0.05.

Poole and McCormick (1988) interpreted these observations as indicating a multistage cloud formation process involving both the aerosol haze and cirrus-like ice clouds discussed earlier. They have modeled this formation process and predicted backscatter ratios and depolarizations that are consistent with lidar measurements.

The observations by Iwasaka (1986) are compatible with such an interpretation. At Syowa Station in 1983, the backscatter ratio at altitudes of 10 km to 20 km increased from about 2 to 5 in early June to about 5 to 10 at the end of June. The depolarization ratio over this same period increased from 0.01–0.1 to 0.3–0.6. Simultaneously, the temperature of the region decreased steadily from well above the frost point at the end of May to near the frost point in early July (for an assumed water vapor concentration of 6 ppmv).

10.6.3.2 Radiative Heating of PSC's

It has been suggested that polar stratospheric clouds may cause significant heating of the Antarctic polar stratosphere in spring (e.g., Tung, 1986). Such heating could occur by three processes: 1) absorption of solar visible and near ultraviolet radiation, 2) absorption of solar near infrared radiation, and 3) net absorption of terrestrial longwave (thermal infrared) radiation. Because the expected composition of PSC's in all cases consists of materials that do not absorb visible radiation, and only weakly absorb near ultraviolet radiation, (1) will not be important.

AEROSOL ABUNDANCES AND DISTRIBUTIONS

The absorption of solar near-infrared radiation by cloud particles can occur in the near-IR H_2O and HNO_3 bands. Considering the particles to be composed of pure water (ice), and assuming PSC optical depths of 0.01 to 0.1, T. Ackerman (private communication, 1987) has estimated solar heating rates ranging from about 0.001°C to 0.01°C per day (other assumptions are $1\text{ }\mu\text{m}$ radius spherical ice particles uniformly distributed between 10 km and 20 km altitude; surface albedo of 0.5 at all solar wavelengths; solar zenith angle of 75.7° ; and a McClatchey subarctic winter temperature profile). By comparison, the heating rate associated with ozone absorption of near-ultraviolet sunlight under the same conditions is roughly 0.5°C per day. The near-infrared absorption of condensed HNO_3 would contribute to the PSC heating (although the corresponding H_2O heating would have to be decreased in accordance with the reduced water-mass fraction of the particles). It is doubtful that cloud particles of mixed composition would produce substantially more heating than pure ice particles. Accordingly, the near-infrared heating rate associated with PSC's should amount only to a few percent of the ozone solar near ultraviolet heating rate. Vapor phase H_2O and HNO_3 also absorb solar radiation; hence, the differential heating in the presence of PSC's also depends on the fraction of these materials that is condensed.

Pollack and McKay (1985) investigated the absorption and emission of longwave radiation by PSC's, and the effects of PSC's on the net heating rates in the polar winter stratosphere. The local net heating rate in the stratosphere is determined mainly by the balance between absorption of upwelling terrestrial radiation, and cloud emission of thermal radiation. The net heating rate depends on the underlying surface temperature, on the tropospheric temperature profile, on the presence and characteristics of cirrus clouds, and on the properties of the PSC's (particle composition, size distribution, and height distribution, and cloud optical depth). For nearly all of the cases considered by Pollack and McKay (1985)—deemed by these authors to represent a comprehensive range of possibilities—the PSC's typically caused a small net longwave cooling of the stratosphere, by up to 1°C per day. In a few cases, warming rates of $\sim 0.07^\circ\text{C}$ per day were found.

On the basis of these studies, it may tentatively be concluded that PSC's are not responsible for significant heating of the polar stratosphere in late winter or early spring, during the time when the ozone hole is forming. Ozone solar absorption provides the primary heating under these conditions.

10.7 CONCLUSIONS

The previous discussion has considered the role of stratospheric aerosols in the remote sensing of the global ozone distribution and long-term trends, and in the Antarctic ozone hole phenomenon. On the basis of the extensive information available on aerosols in the upper atmosphere, the following major conclusions can be drawn.

1. No significant trends that might affect ozone observations can be detected in existing measurements of the global background stratospheric aerosol layer. Likewise, polar stratospheric clouds do not appear to have changed substantially over the early period of their observation (1979 to 1984). However, in 1987 the Antarctic PSC's persisted several weeks longer than usual—well into October—with more sightings of very dense clouds than in previous years. It should be noted that the data records for stratospheric aerosols and PSC's are of a short enough duration that small trends over longer timespans cannot be precluded.

2. The stratospheric aerosol loading is occasionally greatly enhanced by a major volcanic eruption. Such eruptions (for example, El Chichón in 1982), even in remote locations, can perturb the stratosphere worldwide, including the polar regions in both hemispheres, for periods of several years or more. During these volcanic periods, the radiative properties of the atmosphere can be anomalous, complicating the interpretation of remote sensing data.

3. New intercomparisons between SAGE and SME satellite observations indicate that significant aerosol loadings (with respect to remote ozone-sounding measurements) rarely occur above about 35 km—that is, within the altitude region where the accuracy and information content of the SBUV ozone-profiling system is greatest. Hence, background aerosols are not likely to be responsible for ozone errors of more than a few percent in the SBUV layers 6 to 9 (~25 km to 50 km); nor can aerosols explain any long-term trend in the SBUV data. Even so, volcanic aerosols may cause sizeable errors in SBUV ozone profile measurements during relatively short periods following major eruptions. There is little evidence to support the idea of persistent widespread mesospheric aerosol layers (except at the summer mesopause) that might significantly interfere with remote ozone observations.

4. The impact of volcanic aerosols on ground-based Umkehr measurements is greatest in the upper Umkehr layers (7 to 9, above about 30 km) and the lower layers (1 to 3, below about 20 km). The Umkehr data may be corrected for aerosol effects using lidar and satellite data on the vertical and horizontal distributions of particles. Nevertheless, the residual ozone errors in postvolcanic years may exceed several percent at the most sensitive levels. Accordingly, in ozone trend analysis, very careful handling, or neglect, of Umkehr data collected during volcanically disturbed periods is recommended.

5. Direct observations of polar stratospheric cloud properties, together with independent measurements of related physical and chemical parameters, strongly imply that PSC's are intimately involved in the formation of the Antarctic ozone hole. This conclusion is based on the following facts:

- PSC's appear in the proper temporal sequence and spatial configuration to be closely associated with the development of the ozone hole.
- Thermodynamic data suggest that PSC's may be formed through the cocondensation of H_2O , HNO_3 , and HCl vapors; cloud particle sedimentation is also consistent with the observed dehydration and denitrification of the winter polar vortex (see Chapter 11).
- Measured PSC optical and morphological properties are compatible with the PSC composition and microphysics inferred above. PSC's are also known to occur in the northern polar winter stratosphere. Accordingly, effects of PSC formation on ozone concentration could be studied in the Northern Hemisphere, as has been done in the Southern Hemisphere. Although much has been learned in the last few years about PSC's and their relation to the ozone hole, considerable uncertainty remains concerning many of the fundamental physical and chemical processes.

Recommendations

A number of logical recommendations follow from the present assessment.

1. Continued monitoring of the global stratospheric aerosol layer is needed, preferably using satelliteborne sensors. Such monitoring not only provides basic scientific information on the

AEROSOL ABUNDANCES AND DISTRIBUTIONS

properties and physicochemical effects of atmospheric particles, it also establishes a data base that is essential to remote-sensing system design and operation for the detection of ozone and other terrestrial and atmospheric parameters.

2. Regular lidar aerosol measurements should be carried out at selected Umkehr ozone observation sites to obtain a data set that can be used to correct Umkehr data for variable aerosol properties; such correlative data would greatly improve the precision of the ground-based segment of the long-term ozone-monitoring network.

3. The effects of aerosols on remote-sensing systems should be more carefully accounted for in computational inversion schemes; appropriate algorithms and data requirements should be fully investigated, and, where necessary, more sophisticated approaches implemented.

4. Further research should be pursued to obtain a more complete understanding of the physical chemistry, surface reactions, microphysics, and occurrence of polar stratospheric clouds.

Discussion

The advent of satelliteborne sensors has led to a global description of stratospheric aerosols. The recorded morphology and climatology of these trace atmospheric constituents have become more comprehensive and precise. Through extensive space- and ground-based observations, the evolution of volcanic eruption clouds like that of El Chichón has been characterized in considerable detail.

The degradation by aerosols of remote sensing for ozone (and other parameters) is now well understood. For example, the present analysis confirms potential problems with Umkehr ozone observations during periods that are influenced by volcanic eruptions. Nevertheless, the overall accuracy of Umkehr data for studying ozone climatology and long-term variations would not be compromised by occasional volcanic eruptions when proper account is taken of anomalous aerosol effects. The SBUV sensors are, in general, less susceptible to aerosol effects than Umkehr sensors; studies of global ozone morphology with the SBUV system should not be greatly affected by aerosol-generated errors. Even so, in times and in regions of volcanic disturbance, the SBUV data must be interpreted with care.

Most exciting has been the recent linkage of polar stratospheric clouds to the formation of the Antarctic ozone hole. Scientific analysis indicates that nitric acid and water vapors can condense in the winter polar stratosphere to form nitric acid ice clouds. The resulting denitrification of the stratospheric air is in all likelihood a crucial aspect of the complex chemical process that leads to the formation of the ozone hole.